



M Ű E G Y E T E M 1 7 8 2

PhD THESIS

Quantum information protocols for spin qubits: from
double quantum dots to large-scale implementations

Dávid Pataki

Supervisor: András Pályi
Associate professor
BME Department of Theoretical Physics

Budapest University of Technology and Economics

2025

Contents

1	Introduction and background	5
1.1	Quantum computing	5
1.2	Qubits in solid-state systems	7
1.2.1	Spin qubits	7
1.2.2	Superconducting qubits	11
1.2.3	Majorana qubits	12
1.3	Quantum error correction	14
1.3.1	Repetition code	14
1.3.2	Stabilizer formalism	17
1.3.3	Surface code	18
2	Triplet blockade: mechanism for spin-to-supercurrent conversion	21
2.1	Simple model of a double quantum dot Josephson junction	22
2.2	Numerical simulations	25
2.3	Even-odd effect	30
2.4	Triplet blockade	32
2.5	Effect of spin-orbit interaction, relation to experiment	33
2.6	Spin-to-supercurrent conversion, coupling to superconducting qubits	35
2.7	Conclusions and outlook	35
3	Coherent errors in stabilizer codes caused by quasistatic phase damping	37
3.1	Quasistatic phase damping as a model of random coherent errors	38
3.2	Example: 2-qubit repetition code	39
3.2.1	Single cycle of error detection	40
3.2.2	Two cycles of error detection	41
3.3	Quasistatic phase damping in stabilizer codes	44
3.3.1	Single cycle of error detection and error correction	44
3.3.2	Multiple cycles	47
3.4	Surface code error threshold	49
3.4.1	Coherent errors lead to coherent error on the logical qubit	49
3.4.2	Error correction with readout errors	50
3.4.3	Fermionic Linear Optics simulation	51
3.4.4	Numerical results	53
3.5	Results for the distance-3 surface code and their relation to experiments	55
3.6	Conclusions and outlook	59
4	Surface code error correction with crossbar spin qubit architectures	61
4.1	The crossbar spin qubit architecture	64
4.2	Surface code stabilizer measurement cycles	65
4.2.1	Z-cycle circuit, X-cycle circuit with CNOT gates	66

4.2.2	Z-cycle circuit, X-cycle circuit using $\sqrt{\text{SWAP}}$ gates	66
4.2.3	Routing and scheduling protocol for parallel operation	66
4.2.4	Line-by-line implementation	70
4.2.5	Dependence of the logical error on the code distance	72
4.3	Pulse sequence for the stabilizer measurement cycles	76
4.3.1	Abstract pulse sequence	76
4.3.2	Verification of the shuttling protocol	78
4.3.3	Physical pulse sequence	80
4.3.4	Idle-qubit errors due to limited control	81
4.4	Overview of auxiliary files	86
4.5	Discussion	87
4.6	Conclusions	88
5	Summary	89
	Thesis statements	91
	Publications related to the thesis statements	94
	Acknowledgements	95
	Bibliography	97

Chapter 1

Introduction and background

1.1 Quantum computing

The transistor was invented in 1947 by John Bardeen, Walter Brattain, and William Shockley, and revolutionized the field of electronics. The metal–oxide–semiconductor field-effect transistor, the most widely used type of transistor, was developed at Bell Labs between 1955 and 1960. Since then, personal computers and smartphones have become widespread and have shaped our daily lives. As technology improves, more and more powerful computers are being manufactured every year by large tech companies (e.g. Intel, AMD, Apple). Today’s commercial processors have billions of transistors (made from silicon) and are capable of performing trillions of operations per second with extremely high precision. Supercomputers are built using thousands of state-of-the-art processors – corresponding to hundreds of thousands of processor cores in total – allowing for significant advancements in computational science. According to Moore’s law [1], the number of transistors on a microchip – and thus computing power – doubles approximately every two years. However, as transistors approach the atomic scale, physical limitations, such as heat dissipation and quantum tunneling, are making it increasingly difficult to maintain this pace. Today, hardware manufacturing companies are using 4 nm production process to squeeze as many transistors into one chip as possible. Innovations such as three-dimensional chip architectures and specialized hardware (e.g. application-specific integrated circuits) have extended Moore’s law, but it is unknown how much longer.

Quantum computing is a revolutionary approach that uses the principles of quantum mechanics to process information. Unlike classical computers that use bits (which can take the value 0 or 1), quantum computers use quantum bits (or qubits), which can exist in superposition of states (e.g. 0 and 1 with 50% probability for both). This allows quantum computers to solve problems – such as factoring large integers [2], simulating quantum systems [3, 4], or optimizing sophisticated functions efficiently [4, 5] – that could be considered unsolvable by classical algorithms due to the vast amount of computational time required (even for supercomputers). Quantum computer prototypes do exist today, but have not yet realized their potential due to their small number of qubits and the significant level of noise in physical implementation [6]. Currently, the USA – via private companies such as Microsoft, IBM, Google, Amazon – and China are the global leaders in the field, however Europe is also investing significant amounts of money in quantum technologies [7]. Indicative of the growing industry, Ref. [8] showed that in 2022 there were more than 400 start-up companies worldwide focusing on quantum technologies.

A qubit can be created from any system with two distinct quantum states, $|0\rangle$ and $|1\rangle$. These two states are called the computational basis states, and an arbitrary (pure) qubit state can be obtained as the linear combination of those,

$$|\psi\rangle = \alpha|0\rangle + \beta|1\rangle, \tag{1.1}$$

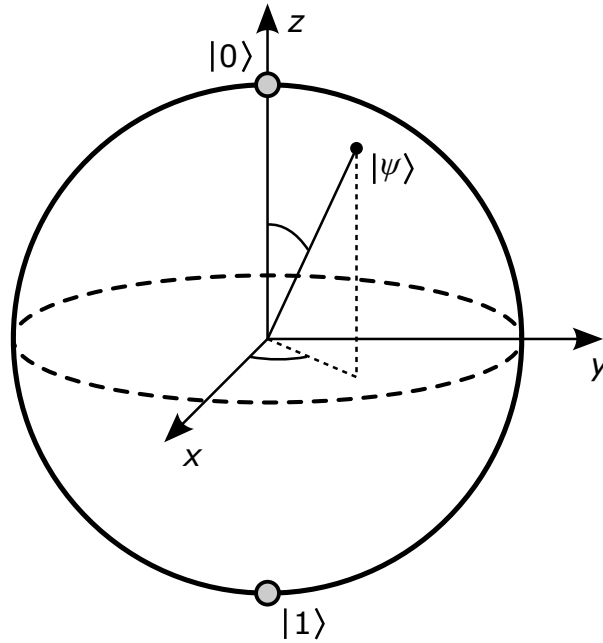


Figure 1.1: Arbitrary pure quantum state $|\psi\rangle$ of a qubit (see Eq. (1.1)) represented on the Bloch sphere.

where α and β are complex coefficients, fulfilling the normalization condition,

$$|\alpha|^2 + |\beta|^2 = 1. \quad (1.2)$$

Qubit states can be represented as vectors, using the basis states

$$|0\rangle = \begin{pmatrix} 1 \\ 0 \end{pmatrix}, \quad |1\rangle = \begin{pmatrix} 0 \\ 1 \end{pmatrix}, \quad (1.3)$$

or visualized on the surface of a unit sphere, called the Bloch sphere [9], which is shown in Fig. 1.1. Multi-qubit states are described by 2^n complex coefficients (in a tensor product basis), where n is the number of qubits. This means that increasing the number of qubits linearly, the amount of data fully characterizing their quantum state grows exponentially.

Qubit manipulation is described by unitary operations applied to the quantum state Eq. (1.1). Any single-qubit rotation on the Bloch sphere has its corresponding 2×2 unitary matrix. Operations involving more qubits usually generate entanglement or swap the qubit states. These single and multi-qubit operations are often called gates, and a quantum algorithm can be represented as a quantum circuit [9], see Fig. 1.2. To obtain a universal gate set that is capable of realizing any desired operation, a few single-qubit gates and an appropriately chosen two-qubit gate are sufficient. For instance, a commonly used universal gate set includes the T gate, the S gate, the Hadamard gate, and the controlled-NOT (CNOT) [9]:

$$\{T, S, H, \text{CNOT}\}. \quad (1.4)$$

The definition of these gates is listed in Table 1.1. These gates can be used to generate any single-qubit rotation and to entangle qubits. The Solovay–Kitaev theorem guarantees that such a set can be used to approximate any desired quantum gate with a short sequence of gates, which can also be found efficiently [9, 10]. A circuit lacking T gates (containing S , H , and CNOT gates only) is called a Clifford circuit. Interestingly, an n qubit Clifford circuit including measurements, composed of m operations can be simulated in $\mathcal{O}(n^2m)$ polynomial time on a

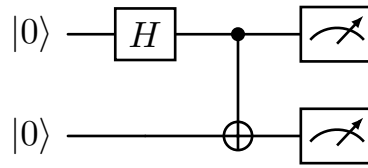


Figure 1.2: Example quantum circuit that prepares an entangled two-qubit state (Bell state) from the initial $|0\rangle$ states. At the end of the circuit, the qubits are measured. The definition of the gates building up the quantum circuit can be found in Table 1.1.

classical computer [11–13]. This means that not only coherence and entanglement [14], but *magic* (or non-stabilizerness) injected by the T gates is also an important ingredient of a truly quantum algorithm [15, 16].

The physical description of a quantum gate is based on the Hamiltonian $\hat{\mathcal{H}}(t)$ which generates the unitary time evolution of the involved qubits governed by the time-dependent Schrödinger equation. Hence, an arbitrary gate U can be expressed as

$$U = \mathcal{T} \exp \left(-\frac{i}{\hbar} \int_0^{T_g} dt \hat{\mathcal{H}}(t) \right), \quad (1.5)$$

where \mathcal{T} is time ordering, $\hbar = h/(2\pi)$ is the reduced Planck constant, and T_g is the gate duration. Physical realization of quantum gates and qubits thus corresponds to engineering the Hamiltonian of the system, $\hat{\mathcal{H}}$. In contrast with the deterministic time evolution, projective measurement of the qubit in the computational basis collapses the wavefunction and gives the outcome 0 or 1 with probabilities $p_0 = |\alpha|^2$ and $p_1 = |\beta|^2$, and post-measurement states $|0\rangle$ and $|1\rangle$, respectively.

It is worthwhile to mention that measurement-based quantum computation (MBQC) offers a fundamentally different approach from the traditional circuit model that is based on unitary time evolution. Instead of manipulating qubits through a sequence of gates, MBQC uses a highly entangled initial state (called *graph state* or *cluster state*) and performs the computation through destructive single-qubit measurements alone [17–19]. This measurement-based approach can simplify experimental realization for some architectures, e.g. for photonic quantum computing [20].

1.2 Qubits in solid-state systems

1.2.1 Spin qubits

In practice, useful quantum algorithms would require millions of qubits [21], thus scalability is a crucial criterion for qubit architectures. In the past 25 years, semiconductor spin qubits have emerged as a promising platform for future quantum computers. A single electron or a single hole confined in a semiconductor quantum dot has a small characteristic size (10 – 100 nm) [22, 23] compared to superconducting qubits (100 microns) [24]. Furthermore, spin qubits also have high-fidelity universal quantum control (single-qubit and two-qubit gate fidelities above 99.5%) [25, 26], the capability of operation above one kelvin [27–31], and their fabrication exploits today’s highly advanced technologies of the semiconductor industry [32–34].

Loss–DiVincenzo qubits

Loss–DiVincenzo qubits are single-electron spin qubits hosted in quantum dots ("artificial atoms"). A two-dimensional electron gas can be formed in a semiconductor heterostructure at the interface layer. Fig. 1.3 shows such a heterostructure, a GaAs quantum dot device. Metallic gate electrodes are used to form the quantum dots by applying a negative gate voltage

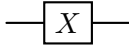
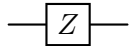
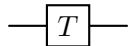
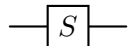
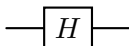
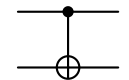
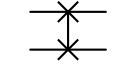
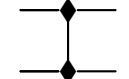
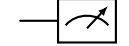
Name of the gate	Circuit notation	Matrix
Pauli-X (X , NOT)		$\begin{pmatrix} 0 & 1 \\ 1 & 0 \end{pmatrix}$
Pauli-Z (Z)		$\begin{pmatrix} 1 & 0 \\ 0 & -1 \end{pmatrix}$
T		$\begin{pmatrix} 1 & 0 \\ 0 & e^{i\pi/4} \end{pmatrix}$
S		$\begin{pmatrix} 1 & 0 \\ 0 & i \end{pmatrix}$
Hadamard (H)		$\frac{1}{\sqrt{2}} \begin{pmatrix} 1 & 1 \\ 1 & -1 \end{pmatrix}$
Controlled-NOT (CNOT)		$\begin{pmatrix} 1 & 0 & 0 & 0 \\ 0 & 1 & 0 & 0 \\ 0 & 0 & 0 & 1 \\ 0 & 0 & 1 & 0 \end{pmatrix}$
SWAP		$\begin{pmatrix} 1 & 0 & 0 & 0 \\ 0 & 0 & 1 & 0 \\ 0 & 1 & 0 & 0 \\ 0 & 0 & 0 & 1 \end{pmatrix}$
$\sqrt{\text{SWAP}}$		$\begin{pmatrix} 1 & 0 & 0 & 0 \\ 0 & \frac{1-i}{2} & \frac{1+i}{2} & 0 \\ 0 & \frac{1+i}{2} & \frac{1-i}{2} & 0 \\ 0 & 0 & 0 & 1 \end{pmatrix}$
Measurement		$\begin{pmatrix} 1 & 0 \\ 0 & 0 \end{pmatrix}$ or $\begin{pmatrix} 0 & 0 \\ 0 & 1 \end{pmatrix}$

Table 1.1: List of elementary single and two-qubit gates and the matrices of the corresponding unitary operators in the computational basis. Note that the measurement is not a unitary operation, and it is not deterministic. It is described by a matrix which projects the state of the qubit to $|0\rangle$ or $|1\rangle$, depending on the measurement outcome.

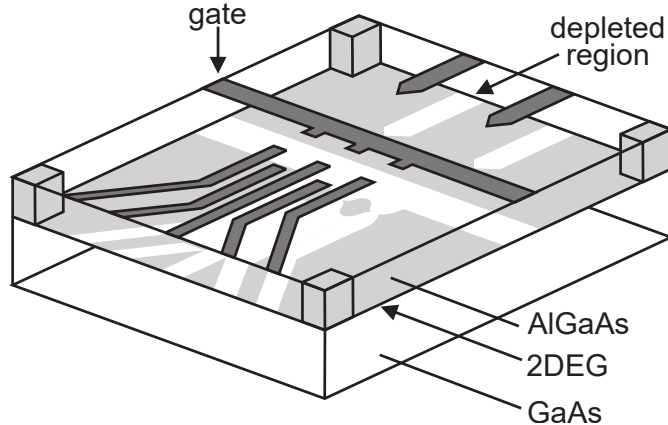


Figure 1.3: GaAs quantum dot device defined by metal surface electrodes (gates). A two-dimensional electron gas (2DEG) is formed at the interface layer between GaAs and AlGaAs. The quantum dots are defined by applying a negative gate voltage to the surface electrodes that creates depleted regions (denoted by white) at the interface layer. Figure taken from Ref. [35].

that creates depleted regions due to Coulomb repulsion. The imposed electrostatic confinement potential has atom-like orbitals (energy levels), suitable for trapping a single electron (see top panel of Fig. 1.4(a)). The electron is a spin-1/2 particle, thus occupying e.g. the ground state orbital it has two energy sublevels, $|\uparrow\rangle$ and $|\downarrow\rangle$, which makes it a natural qubit system when the orbitals are well-separated in energy. An external magnetic field is used to control the energy splitting of these spin states.

The simplest description of a spin qubit confined in a quantum dot is given by the effective Hamiltonian,

$$\hat{\mathcal{H}}_{\text{spin}} = \frac{1}{2} g^* \mu_B B_{\text{eff}}^z \hat{\sigma}_z, \quad (1.6)$$

where $\mu_B = 57.9 \mu\text{eV/T}$ is the Bohr magneton, B_{eff}^z describes the effect of a static external magnetic field (also called the Zeeman field) pointing in the z direction, $\hat{\sigma}_z$ is the Pauli-Z matrix, and g^* is the effective g-factor which is dependent on the host material and the electrostatic potential landscape that is used to define the quantum dot. In vacuum, the electron g-factor is $g = 2$, while in semiconductor devices it is renormalized by the spin-orbit interaction and ranges between $0.2 \lesssim g^* \lesssim 15$ [36–38], depending on the direction of the magnetic field as well (commonly referred to as g-tensor anisotropy). The static Hamiltonian, Eq. (1.6), induces spin precession around the z axis on a generic qubit state, Eq. (1.1). Therefore, usually it is convenient to describe the qubit dynamics in the so-called qubit frame which rotates with the qubit frequency, $f_Q = g^* \mu_B B_{\text{eff}}^z / h$, around the z axis.

Single-qubit rotations around the x or the y axis are performed by appropriate microwave pulses, and described by

$$\hat{\mathcal{H}}_{\text{drive}}(t) = \frac{1}{2} g^* \mu_B B_{\text{ac}} \sin(\omega_{\text{ac}} t + \phi) \hat{\sigma}_x, \quad (1.7)$$

where B_{ac} is the amplitude, ω_{ac} is the frequency, and ϕ is the phase of the driving field (denoted by $B_{\text{eff}}^x(t)$ in Fig. 1.4). To reach complete oscillations on the Bloch sphere, the drive has to be resonant with the qubit frequency, $\omega_{\text{ac}} = 2\pi f_Q$. The actual rotation angle is determined by the drive strength B_{ac} and the pulse duration, while the axis of the rotation is controlled by the phase ϕ . Alternatively, in the presence of (strong) spin-orbit interaction, it is also possible to drive the qubit with an ac electric field [30, 39, 40].

Neighboring spins (e.g. in a double quantum dot) interact via Heisenberg exchange. This exchange interaction arises from the spatial overlap of the electronic wavefunctions, thus its

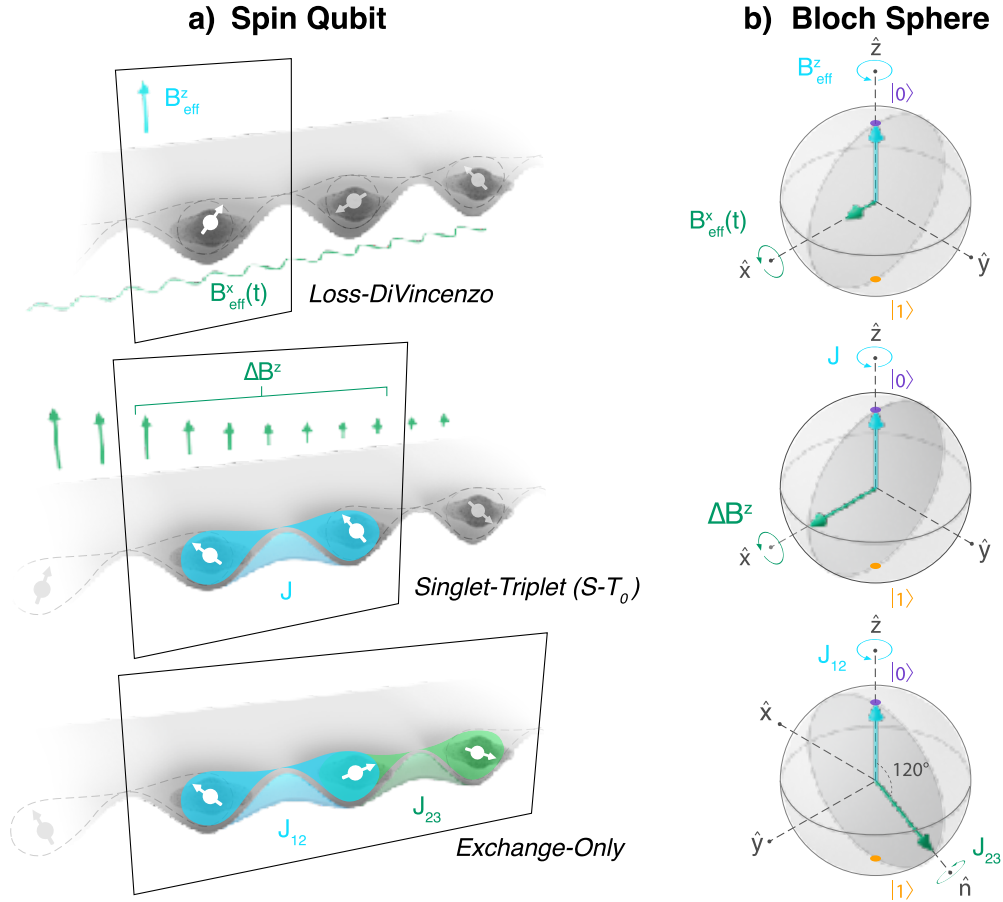


Figure 1.4: Spin qubits in quantum dots. (a) Spin configurations, (b) Bloch spheres associated with Loss–DiVincenzo single spin qubits, two-spin singlet-triplet qubits, and three-spin exchange-only spin qubits. Figure taken from Ref. [23].

strength is controlled by the tunnel barrier separating the qubits [41]. Heisenberg exchange naturally gives rise to a SWAP or a $\sqrt{\text{SWAP}}$ gate (listed in Table 1.1), however, when the exchange is anisotropic it could be exploited to engineer a CNOT gate as well [42].

In these devices, the readout of the spin quantum state relies on spin-dependent single electron tunneling processes (e.g. Pauli spin blockade), which then enable charge readout via direct electronic transport [35], charge sensing techniques [43], or dipole coupling to a microwave resonator [44, 45]. Pauli spin blockade (PSB) is a mechanism in double quantum dot systems where electron tunneling is inhibited due to the Pauli exclusion principle. When two electrons occupy a double quantum dot, the transition from the (1, 1) charge configuration to the (0, 2) configuration is allowed only if the electrons form a spin singlet state; triplet states are blocked (provided the orbital level spacing is large) because the (0, 2) configuration can only accommodate a singlet pair on the same orbital. Thus, PSB enables spin-to-charge conversion [35].

Today, state-of-the-art devices are based on silicon metal-oxide-semiconductor (MOS) and Si/SiGe heterostructures, and they have 4-12 qubits with single-qubit and two-qubit gate durations $T_g \approx 10 - 100$ ns [22, 46–48].

Singlet-triplet qubits

Controlling the on-site energies and the tunnel coupling, a double quantum dot can be tuned to a charge configuration where both dots are occupied by one electron. Eigenstates of such a

two-spin system have also been utilized to encode a single qubit [49], shown in the middle panel of Fig. 1.4. Distinguished by the total spin quantum number, the singlet and triplet quantum states,

$$|S\rangle = \frac{1}{\sqrt{2}} (|\uparrow\downarrow\rangle - |\downarrow\uparrow\rangle), \quad (1.8)$$

$$|T_0\rangle = \frac{1}{\sqrt{2}} (|\uparrow\downarrow\rangle + |\downarrow\uparrow\rangle), \quad (1.9)$$

can be identified as e.g. $|0\rangle = |T_0\rangle$, and $|1\rangle = |S\rangle$. In this case, the qubit Hamiltonian has the form

$$\hat{\mathcal{H}}_{ST_0} = \frac{J}{2} \hat{\sigma}_z = \frac{J}{2} (|0\rangle\langle 0| - |1\rangle\langle 1|) = \begin{pmatrix} \frac{J}{2} & 0 \\ 0 & -\frac{J}{2} \end{pmatrix}, \quad (1.10)$$

where J is the exchange energy, i.e. the energy splitting between the singlet and the triplet states at zero magnetic field. For two electrons in a double quantum dot, the exchange energy J can be controlled electrically by changing the detuning or the tunnel barrier between the two quantum dots. The exchange splitting of the singlet-triplet qubit leads to oscillations about the z axis of the Bloch sphere, similar to the Zeeman field for Loss–DiVincenzo qubits. Rotations about the x axis of the Bloch sphere can, e.g., be achieved with magnetic field gradients ΔB^z (depicted in green in Fig. 1.4) or differences in g -factors that lead to an energy difference between the $|\uparrow\downarrow\rangle$ and $|\downarrow\uparrow\rangle$ states [50, 51].

Other types of spin qubits

Similarly to singlet-triplet qubits, exchange-only qubits are encoded using the collective quantum state of a few (e.g. three) spins [52, 53], see the bottom panel of Fig. 1.4(a). By adjusting the nearest-neighbor exchange coupling, it is possible to manipulate the encoded qubit state (as shown in the bottom panel of Fig. 1.4(b)) and entangle neighboring qubits as well [52, 54]. The main advantage of exchange-only qubits is that they can operate without direct single-spin rotations, which typically require precise control of magnetic fields. Instead, they rely solely on electrically tunable, fast exchange pulses [55], making them easier to fabricate, without the need for an external magnetic field. Additionally, when they are operated in the combined total spin angular momentum $S_{\text{tot}} = 0$ subspace, they decouple from certain local magnetic field fluctuations (e.g. hyperfine noise) [56, 57].

A fundamentally different approach to spin qubits is to use nuclear spin states for quantum computing. Doped semiconductors [58], or point defects [59] are the host platforms for these qubits. Nuclear spins are ideal candidates for storing quantum information since they exhibit high coherence [60]. Unlike traditional spin qubits driven by microwave pulses, nuclear spin qubits are addressed using radio-frequency electromagnetic fields. In these registers, besides nuclear spins, nearby electrons are also utilized as spin qubits and play a crucial role: provided by the hyperfine interaction they allows for the readout of nuclear spin states and efficient multi-qubit operations [61].

1.2.2 Superconducting qubits

Today, superconducting qubits are the most advanced among solid-state qubit platforms in terms of qubit count and average gate fidelities [62, 63]. An effective description of the transmon qubit is often done using the Hamiltonian of a Cooper pair box [64]: a superconducting island tunnel coupled to a grounded superconductor (called the “lead”),

$$\hat{\mathcal{H}}_{\text{transmon}} = 4E_C (\hat{n} - n_g)^2 - E_J \cos \hat{\varphi}. \quad (1.11)$$

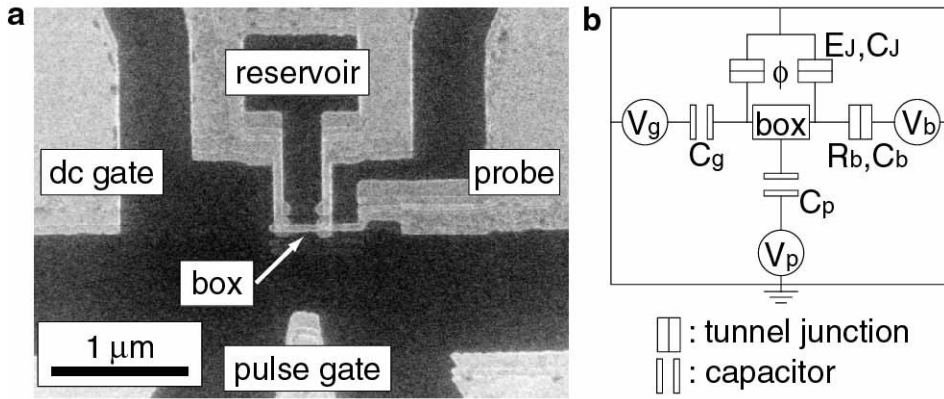


Figure 1.5: The Cooper pair box. (a) Micrograph image of the device. (b) Circuit diagram showing that the superconducting island ("box") is in contact with a superconducting reservoir through a tunnel junction with capacitance C_J . The Josephson energy E_J is tunable by magnetic flux ϕ . Excess Cooper pairs tunnel onto the island in response to an electric field applied by means of the gate capacitance C_g and gate voltage V_g . Figure taken from Ref. [66].

The Cooper pair box is depicted in Fig. 1.5. In the Hamiltonian, \hat{n} is the number of Cooper pairs on the island, $\hat{\phi}$ is the gauge-invariant phase difference between the superconductors, E_C is the charging energy (determined by the total capacitance of the box electrode), $n_g = C_g V_g / (2e)$ is the offset charge (tunable by gate voltage V_g) with $2e$ being the electric charge of a Cooper pair, and E_J is the Josephson energy (tunable by magnetic flux). The number operator \hat{n} and the phase operator $\hat{\phi}$ are conjugate variables, as position and momentum. Fig. 1.6 shows the energy spectrum as a function of the offset charge n_g for different E_J/E_C ratios. The transmon is operated in the regime $E_J \gg E_C$, where the dispersion is completely flat (as shown in Fig. 1.6(d)) providing reduced sensitivity to charge noise. In terms of the energy spectrum, this system is equivalent to an anharmonic oscillator whose lowest two eigenstates are used to realize a qubit. Since the second excited state ($m = 2$, blue line in Fig. 1.6(d)) is not far in energy, leakage from the computational subspace can occur during operation, and in certain applications it has to be mitigated [65].

Single-qubit rotations are usually implemented as microwave pulses (with pulse duration $T_g \approx 10$ ns) applied through control lines that are capacitively coupled to the qubit island [67, 68]. In a modern architecture, the transmon qubits are also coupled to each other, and to a readout resonator, allowing for two-qubit gates and qubit measurement [68, 69], respectively.

Most recently, Andreev spin qubits have emerged, combining superconducting qubits and spin qubits. These type of hybrid qubits utilize Andreev bound states, which form at the interface between the superconducting and a normal (non-superconducting) material when they are strongly coupled [70]. Andreev spin qubits have been realized in semiconductor-superconductor hybrid nanowires [71]. Experiments demonstrated coherent single-qubit manipulation and coupling between two Andreev spin qubits [72, 73].

1.2.3 Majorana qubits

Topological protection is an intriguing phenomenon of condensed matter physics arising in systems whose band structure has a non-zero topological invariant [74]. A qubit encoded in the degenerate ground state of a one-dimensional topological superconductor is shown to be protected against local disorder and noise [75, 76]. A simple model possessing such a robust ground-state degeneracy is the Kitaev chain [77]. Quantum information could be stored in the fermion parity of Majorana zero modes localized at the end of the chain in a robust way. A

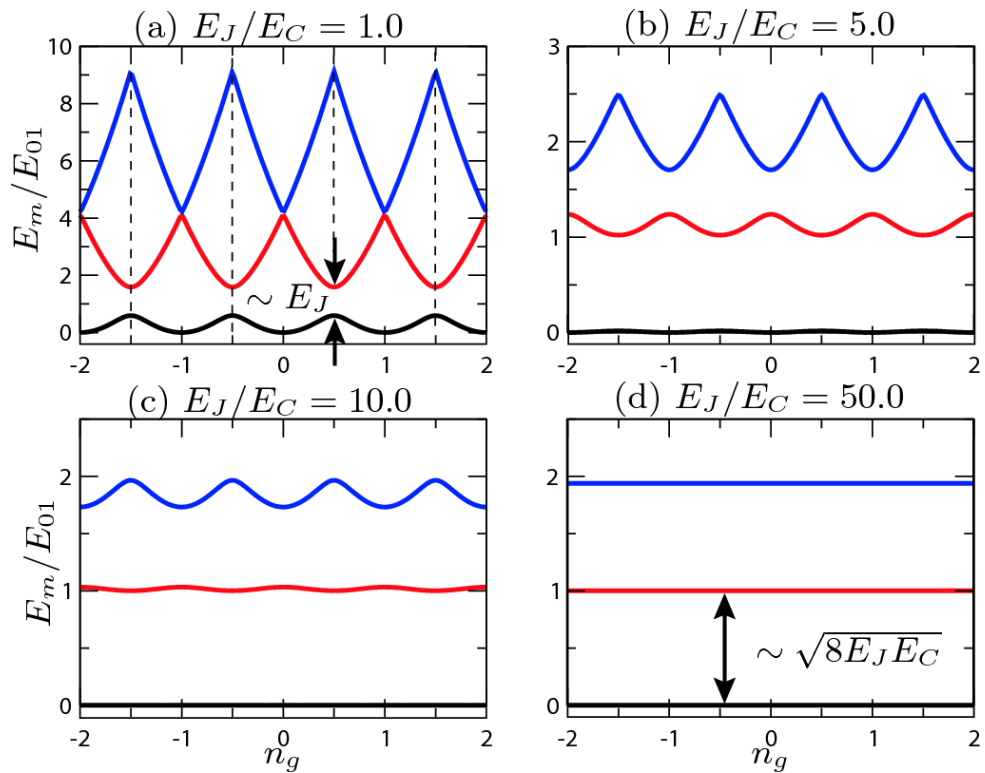


Figure 1.6: Eigenenergies (lowest three levels, $m = 0, 1, 2$) of the transmon Hamiltonian, Eq. (1.11), as a function of the offset charge n_g for increasing ratios E_J/E_C from (a) to (d). Energies are given in units of the transition energy E_{01} , evaluated at the degeneracy point $n_g = 1/2$. Panel (d) shows the transmon regime where the dispersion is completely flat, providing reduced sensitivity to charge noise. Figure taken from Ref. [64].

Majorana qubit is formed using two uncoupled Kitaev chains, e.g., in the globally even subspace. Qubit manipulation is possible via spatial exchange ("braiding") due to the non-Abelian statistics of these zero-energy excitations [78, 79]. Projective measurements of the fermion parity could be used to perform the qubit readout [80]. The simulation of braiding, dephasing, and readout of Majorana qubits is extensively studied in the group of my supervisor [81–85].

The fabrication of such topological systems is a challenging task. However, recent proposals based on quantum dot-superconductor hybrid structures appear to be attainable by experiments [86–89].

1.3 Quantum error correction

In the absence of topological protection, decoherence drives the quantum systems to the classical regime where the speedup of quantum computers vanishes. For example, factoring a 2048 bit RSA integer using Shor's algorithm requires around 10^{12} operations [21], thus at least 10^{-12} precision per operation. Today's state-of-the-art quantum chips have roughly 100 qubits with 10^{-3} best case precision. Therefore, a formidable nine orders of magnitude improvement is demanded to be able to successfully execute the factoring task.

An alternative solution is to use quantum error correction to prevent decoherence, and achieve higher operational precision. This requires many more qubits, roughly one million of them to implement the factoring algorithm [90]. The corresponding five orders of magnitude improvement seems to be more attainable than the nine orders of magnitude required through precision alone. In line with this observation, most experts agree that quantum error correction is the viable approach for achieving practical quantum computing.

A quantum error correction code is able to detect bit-flip and phase-flip errors, and a subsequent recovery operation can be applied to correct these errors. Using such a scheme, quantum information of a single logical qubit is distributed over many entangled physical qubits [91], enabling the identification of errors through a decoding process. The fault-tolerance theorem guarantees that if the noise per elementary operation is below a non-zero *error threshold* then quantum computation can be performed efficiently with arbitrary accuracy [75, 92–94]. However, increasing accuracy requires an increasing number of physical (data) qubits, and not all quantum processors can run all codes (quantum error correction codes are not hardware agnostic). A chronological overview of quantum error correction experiments (from 1998 up to 2024) on all hardware platforms is given in Table II. of Ref. [95].

1.3.1 Repetition code

A fundamental example of error correction codes is the repetition code. The classical repetition code encodes bits by repeating them: the smallest code that can correct errors uses three physical bits to encode one logical bit with the mapping

$$0_L = 000, \quad 1_L = 111, \quad (1.12)$$

where 000 and 111 are known as the *codewords* [9]. If the measured state is outside of the codespace (i.e. it is neither 000 nor 111) then at least one bit-flip error occurred. Error correction can be implemented by taking a majority vote. If each physical bit is subject to an independent error probability p , then the logical error probability of this scheme (the probability of the majority vote being incorrect, which happens if more than half of the bits were flipped) becomes

$$p_L = p^3 + 3p^2(1 - p), \quad (1.13)$$

since there are $\binom{3}{2} = 3$ possible ways to flip two out of three bits. When the physical error probability is sufficiently small, that is, below the *code threshold*, the logical error probability

can be suppressed by increasing the number of physical bits in the code. In Eq. (1.13), the logical error probability is lower than the physical error probability, $p_L < p$, as long as $p < p_{\text{th}} = 0.5$, which coincides with the code threshold in this case.

In quantum information, bit-flip errors (Pauli-X noise) can be corrected using an equivalent encoding for a logical qubit, e.g.

$$|0_L\rangle = |0\rangle \otimes |0\rangle \otimes |0\rangle \equiv |000\rangle, \quad |1_L\rangle = |1\rangle \otimes |1\rangle \otimes |1\rangle \equiv |111\rangle. \quad (1.14)$$

These states are called the codeword basis states, and they span the *codespace*. A general pure qubit state, Eq. (1.1) is thus encoded in the codespace as

$$|\psi_L\rangle = \alpha |0_L\rangle + \beta |1_L\rangle = \alpha |000\rangle + \beta |111\rangle. \quad (1.15)$$

Projective measurement of the individual qubits would collapse the wavefunction, destroying the encoded qubit. Avoiding this, the single-qubit errors are detected via checking that the parity of any pair of qubits is even (the state is in the subspace spanned by $|000\rangle$ and $|111\rangle$). Measuring the joint Z-parity of qubits i and j is equivalent to measuring the observable $\hat{Z}_i \otimes \hat{Z}_j \equiv \hat{Z}_i \hat{Z}_j$, therefore the observables $\hat{Z}_1 \hat{Z}_2 \hat{I}_3$ and $\hat{I}_1 \hat{Z}_2 \hat{Z}_3$, with \hat{I} being the identity matrix, reveal where neighbouring qubits differ in parity. The Z-parity of two qubits can be measured using an ancillary qubit, as shown in Fig. 1.7(a). The outcome of these parity measurements is known as the *error syndrome* [96]. For example, a bit-flip error on the first qubit, described by $\hat{X}_1 \hat{I}_2 \hat{I}_3$, changes the encoded state as

$$|\psi_L\rangle \rightarrow \hat{X}_1 \hat{I}_2 \hat{I}_3 |\psi_L\rangle = \alpha |100\rangle + \beta |011\rangle, \quad (1.16)$$

and it is detected by the first parity check, since the $\hat{Z}_1 \hat{Z}_2 \hat{I}_3$ check operator, which anticommutes with the error operator, will return with (-1) eigenvalue in this case, resulting in error syndrome $(-1, +1)$.

In case of Pauli errors, the error can be corrected by applying the same Pauli operator on the encoded state (flipping the same qubit twice is the same as identity). However, in a physical experiment, one only sees the resulting error syndrome and has to propose a correction based on that. Assuming that errors happen independently, with a small probability, it is easy to find the optimal strategy for correction, since there are only 4 different error syndromes altogether. The correction operations inferred from the syndromes are

$$(+1, +1) \rightarrow \hat{I}_1 \hat{I}_2 \hat{I}_3, \quad (1.17)$$

$$(-1, +1) \rightarrow \hat{X}_1 \hat{I}_2 \hat{I}_3, \quad (1.18)$$

$$(+1, -1) \rightarrow \hat{I}_1 \hat{I}_2 \hat{X}_3, \quad (1.19)$$

$$(-1, -1) \rightarrow \hat{I}_1 \hat{X}_2 \hat{I}_3. \quad (1.20)$$

Table 1.2 lists all possible bit-flip errors, and the resulting faulty logical states, error syndromes, correction operations, and the final states after error correction. Error correction is successful when the final state is identical to the initial encoded state, Eq. (1.15), which is the case when a single error occurs only.

Single-qubit phase-flip errors (Pauli-Z noise) can be corrected similarly with the encoding

$$|0_L\rangle = |+\rangle \otimes |+\rangle \otimes |+\rangle \equiv |+++ \rangle, \quad (1.21)$$

$$|1_L\rangle = |-\rangle \otimes |-\rangle \otimes |-\rangle \equiv |-- \rangle, \quad (1.22)$$

where $|+\rangle$ and $|-\rangle$ are the eigenstates of \hat{X} ,

$$|+\rangle = \frac{1}{\sqrt{2}} (|0\rangle + |1\rangle), \quad (1.23)$$

$$|-\rangle = \frac{1}{\sqrt{2}} (|0\rangle - |1\rangle). \quad (1.24)$$

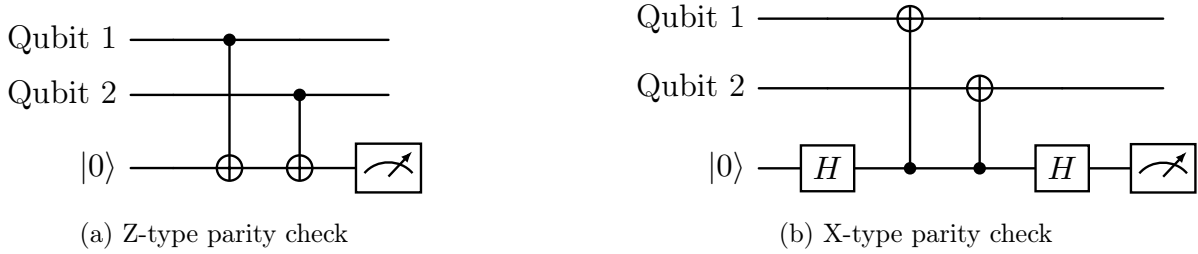


Figure 1.7: Quantum circuits that measure the parity of two qubits in (a) Z basis and (b) in X basis, using an ancillary qubit (prepared in $|0\rangle$) and CNOT gates. Even parity is associated with the outcome 0 (corresponding to the $+1$ eigenvalue of $\hat{Z}_1\hat{Z}_2$ or $\hat{X}_1\hat{X}_2$), and odd parity with the outcome 1 (corresponding to the -1 eigenvalue of $\hat{Z}_1\hat{Z}_2$ or $\hat{X}_1\hat{X}_2$). Such a measurement does not disturb the encoded logical state, Eq. (1.15).

Error	Logical state with error	Syndrome	Correction	Final state
$\hat{I}_1\hat{I}_2\hat{I}_3$	$\alpha 000\rangle + \beta 111\rangle$	$(+1, +1)$	$\hat{I}_1\hat{I}_2\hat{I}_3$	$\alpha 000\rangle + \beta 111\rangle$
$\hat{X}_1\hat{I}_2\hat{I}_3$	$\alpha 100\rangle + \beta 011\rangle$	$(-1, +1)$	$\hat{X}_1\hat{I}_2\hat{I}_3$	$\alpha 000\rangle + \beta 111\rangle$
$\hat{I}_1\hat{X}_2\hat{I}_3$	$\alpha 010\rangle + \beta 101\rangle$	$(-1, -1)$	$\hat{I}_1\hat{X}_2\hat{I}_3$	$\alpha 000\rangle + \beta 111\rangle$
$\hat{I}_1\hat{I}_2\hat{X}_3$	$\alpha 001\rangle + \beta 110\rangle$	$(+1, -1)$	$\hat{I}_1\hat{I}_2\hat{X}_3$	$\alpha 000\rangle + \beta 111\rangle$
$\hat{X}_1\hat{X}_2\hat{I}_3$	$\alpha 110\rangle + \beta 001\rangle$	$(+1, -1)$	$\hat{I}_1\hat{I}_2\hat{X}_3$	$\alpha 111\rangle + \beta 000\rangle$
$\hat{X}_1\hat{I}_2\hat{X}_3$	$\alpha 101\rangle + \beta 010\rangle$	$(-1, -1)$	$\hat{I}_1\hat{X}_2\hat{I}_3$	$\alpha 111\rangle + \beta 000\rangle$
$\hat{I}_1\hat{X}_2\hat{X}_3$	$\alpha 011\rangle + \beta 100\rangle$	$(-1, +1)$	$\hat{X}_1\hat{I}_2\hat{I}_3$	$\alpha 111\rangle + \beta 000\rangle$
$\hat{X}_1\hat{X}_2\hat{X}_3$	$\alpha 111\rangle + \beta 000\rangle$	$(+1, +1)$	$\hat{I}_1\hat{I}_2\hat{I}_3$	$\alpha 111\rangle + \beta 000\rangle$

Table 1.2: List of all possible bit-flip errors, and the resulting logical states, error syndromes, correction operations, and the final states after error correction for the 3-qubit bit-flip repetition code. The first row corresponds to having no error. The error syndrome shows the measured value of the observables $\hat{Z}_1\hat{Z}_2\hat{I}_3$ and $\hat{I}_1\hat{Z}_2\hat{Z}_3$. Error correction is successful when the final state is identical to the initial encoded state, Eq. (1.15). This holds for the upper four rows of this table.

In this case, the parity check operators are $\hat{X}_1\hat{X}_2\hat{I}_3$ and $\hat{I}_1\hat{X}_2\hat{X}_3$. An X-type parity check can be measured using extra Hadamard gates, as shown in Fig. 1.7(b).

In conclusion, it is possible to correct bit-flip and phase-flip errors with repetition codes. However, as described in the next section in more detail, the repetition code is insufficient to correct both types of errors simultaneously. Thus the repetition code is often called a classical code [9]. In the following, I discuss quantum codes as well, which can detect and correct both types of errors.

1.3.2 Stabilizer formalism

One of the most common classes of quantum error correction codes is stabilizer codes. The stabilizer formalism provides a framework to define and study quantum error correction codes in terms of (multi-qubit) Pauli operators, rather than directly using the encoded logical states. Stabilizer codes are defined on a set of physical qubits by specifying two sets of operators [96]: a set of independent stabilizer generators, and a set of encoded logical operators. The *stabilizer* generators are n -qubit Pauli operators that leave the codespace invariant (logical identity operations), meaning that each generator \hat{S}_f satisfies

$$\hat{S}_f |\psi_L\rangle = |\psi_L\rangle, \quad (1.25)$$

for any logical state $|\psi_L\rangle$. They generate a group (the stabilizer group of the quantum code), and they commute with each other (Abelian group).

The encoded logical Pauli operators must commute with all elements of the stabilizer group and they have to satisfy the commutation (or anticommutation) relations of the Pauli operators which they represent. For example, the encoded logical X and Z operators act on the logical states as the Pauli-X and Pauli-Z operators on a single qubit:

$$\hat{X}^L |0_L\rangle = |1_L\rangle, \quad \hat{X}^L |1_L\rangle = |0_L\rangle; \quad \hat{Z}^L |0_L\rangle = |0_L\rangle, \quad \hat{Z}^L |1_L\rangle = -|1_L\rangle, \quad (1.26)$$

and the logical Y operator is just the combination of these two, $\hat{Y}^L = i\hat{X}^L\hat{Z}^L$. There are multiple equivalent operators that realize the same encoded logic, since e.g. $(\hat{X}^L\hat{S}_f)|\psi_L\rangle = \hat{X}^L|\psi_L\rangle$.

The *code distance* is the minimal weight of any (non-identity) logical operator on the code, where the weight of an operator is the number of physical qubits it acts on (non-trivially). When different logical operators have different minimal weights, usually the smallest one is taken as the distance of the quantum code. The number of encoded logical qubits k is determined by the number of stabilizer generators m , and the number of physical qubits n as $k = n - m$ [97]. Such a Pauli stabilizer code is denoted as $[[n, k, d]]$. Errors in stabilizer codes are detected by measuring the stabilizer generators. In practice, this is done with the help of ancillary qubits, similarly as described for the repetition code (Fig. 1.7).

The simplest example of a (classical) stabilizer code is the repetition code. The stabilizer generators of the 3-qubit bit-flip repetition code are the operators that are measured to detect bit-flip errors. Thus, the stabilizer group can be viewed as a set of measurements for which error-free logical states return (+1) eigenvalues, but when there is a detectable error, one or more (−1) eigenvalues will be returned. Since n -qubit Pauli operators either commute or anticommute with each other, a measured (+1) eigenvalue reflects that the error operator commutes with the given stabilizer group element, while a (−1) eigenvalue shows that the error operator \hat{E} anticommutes with a stabilizer group element \hat{S}_f ,

$$\hat{S}_f\hat{E}|\psi_L\rangle = -\hat{E}\hat{S}_f|\psi_L\rangle = -\hat{E}|\psi_L\rangle, \quad (1.27)$$

leading out of the codespace. In the stabilizer formalism, the 3-qubit bit-flip repetition code is defined by their stabilizer generators, $\hat{S}_1 = \hat{X}_1\hat{X}_2\hat{I}_3$ and $\hat{S}_2 = \hat{I}_1\hat{X}_2\hat{X}_3$, together with the logical

operators $\hat{X}^L = \hat{X}_1\hat{X}_2\hat{X}_3$, and e.g. $\hat{Z}^L = \hat{Z}_1\hat{Z}_2\hat{Z}_3$. Note that in the bit-flip encoding, Eq. (1.15), a single phase-flip error can cause a logical error, since

$$|\psi_L\rangle \rightarrow \hat{Z}_1\hat{I}_2\hat{I}_3|\psi_L\rangle = \alpha|0_L\rangle - \beta|1_L\rangle = \hat{Z}^L|\psi_L\rangle \quad (1.28)$$

This means that in this case, the code distance for bit-flip errors is $d_X = 3$, but for phase-flips it is $d_Z = 1$.

As described in the previous section, errors are corrected by applying a correction operator that returns the logical state to the codespace. Although, for the simple case of the 3-qubit repetition code, it is easy to list all possible error syndromes and use a look-up table decoder (see Eqs. (1.17)-(1.20)), however in general, the suitable correction operator is calculated by a classical algorithm called a *decoder* [97], based on the stabilizer measurement outcomes. Many quantum error correcting codes can be represented in the stabilizer formalism. The next section provides another example, the surface code, which will play a central role in Chapters 3 and 4 of this thesis.

1.3.3 Surface code

One of the most prominent quantum error correction codes is the surface code [98–100], depicted in Fig. 1.8, which is based on a two-dimensional qubit grid and requires only nearest-neighbor connectivity. The surface code is a code family, whose members are labelled by the odd integer d , the code distance. The distance- d surface code is a stabilizer code, it encodes a single logical qubit, and has code size d^2 , meaning that it consists of $n = d^2$ physical data qubits. The smallest surface code patch suitable for error correction ($d = 3$) is depicted in Fig. 1.8(a). The encoded quantum information is preserved by checking the joint parity of all qubit plaquettes (each formed by four data qubits) in X or Z basis, denoted by light blue or light gray color on Fig. 1.8, respectively. Using the layout of Fig. 1.8, the stabilizer generators of the distance-3 code are

$$\hat{S}_1 = \hat{X}_1\hat{X}_2, \hat{S}_2 = \hat{X}_2\hat{X}_3\hat{X}_5\hat{X}_6, \hat{S}_3 = \hat{X}_4\hat{X}_5\hat{X}_7\hat{X}_8, \hat{S}_4 = \hat{X}_8\hat{X}_9, \quad (1.29)$$

$$\hat{S}_5 = \hat{Z}_1\hat{Z}_2\hat{Z}_4\hat{Z}_5, \hat{S}_6 = \hat{Z}_3\hat{Z}_6, \hat{S}_7 = \hat{Z}_4\hat{Z}_7, \hat{S}_8 = \hat{Z}_5\hat{Z}_6\hat{Z}_8\hat{Z}_9. \quad (1.30)$$

At the edges of the code, instead of weight-4 (e.g. \hat{S}_2), there are only weight-2 (e.g. \hat{S}_1) stabilizers of one type (X or Z). Since the logical qubit states are the common eigenstates of all these stabilizer operators with eigenvalue +1, starting from the computational basis states they can be obtained by projection to the logical subspace as

$$|0_L\rangle = \mathcal{N}_d \prod_{f=1}^{n-1} \frac{\hat{I} + \hat{S}_f}{2} |0\rangle^{\otimes n}; \quad (1.31)$$

$$|1_L\rangle = \mathcal{N}_d \prod_{f=1}^{n-1} \frac{\hat{I} + \hat{S}_f}{2} |1\rangle^{\otimes n}, \quad (1.32)$$

where $\mathcal{N}_d = 2^{(d^2-1)/4}$ is a normalization factor.

Logical X (Z) operators connect the X-type (Z-type) edges of the code, meaning that a string of Pauli-X (Pauli-Z) operators on the physical qubits performs a corresponding X (Z) flip on the logical qubit [100]. Following from the definition of code distance, the shortest such string has length d , see red and blue strings in Fig. 1.8(a), corresponding to logical operators $\hat{X}^L = \hat{X}_1\hat{X}_4\hat{X}_7$ and $\hat{Z}^L = \hat{Z}_1\hat{Z}_2\hat{Z}_3$, respectively. Provided by the fact that they touch at a single data qubit only, the \hat{X}^L and \hat{Z}^L operators anti-commute, just as the physical X and Z operators. Furthermore, the logical operators touch each stabilizer operator on two data qubits,

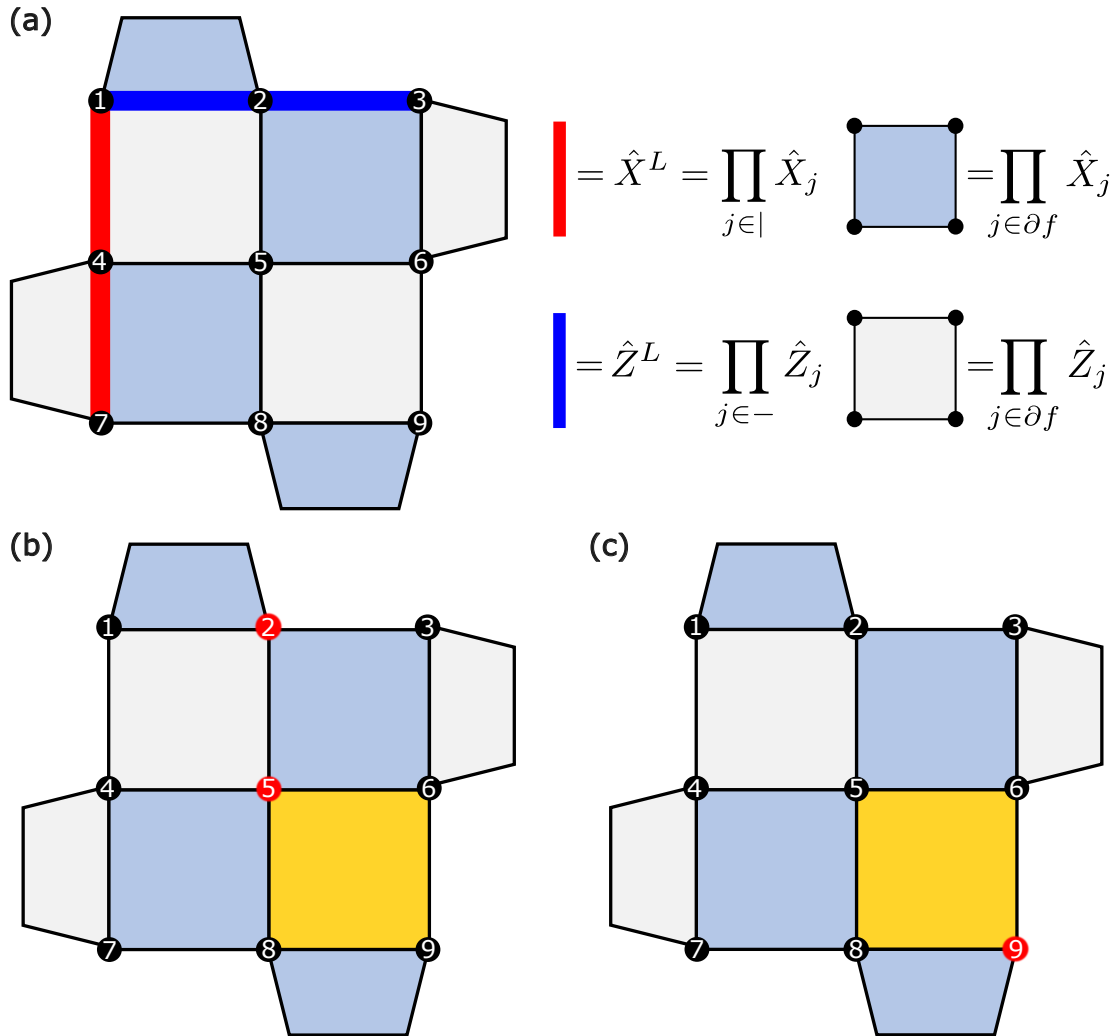


Figure 1.8: Layout of a distance-3 surface code patch [101]. (a) The black dots represent the data qubits. In this case, 9 data qubits encode a single logical qubit. Light blue (light gray) plaquettes represent X-type (Z-type) stabilizer operators. Red (blue) string shows an example logical X (Z) operator. Any string of Pauli-X (Pauli-Z) operators connecting the light blue (light grey) edges, and touching each Z-type (X-type) stabilizer operators on two data qubits is a valid logical X (Z) operator. (b) Error string $\hat{E} = \hat{X}_2 \hat{X}_5$. Red color represents the Pauli-X errors on the physical qubits. Yellow color indicates the change in the corresponding parity check outcome. (c) The single-qubit \hat{X}_9 error results in the same parity check outcome as the error string $\hat{E} = \hat{X}_2 \hat{X}_5$, showing that the distance-3 surface code is able to reliably correct a single error only during a single error correction cycle.

implying that they commute with all of those. Note that, e.g. $\hat{X}^L = \hat{X}_1\hat{X}_5\hat{X}_9$ would be a valid logical X operator as well.

As mentioned previously, error detection is done by measuring all parity checks, and the result of this process is an error syndrome s . After the syndrome is measured, a (classical) decoding algorithm has to be employed to find its cause, i.e., the corresponding errors on the physical qubits. Independent Pauli-X (or Pauli-Z) errors occurring on multiple data qubits simultaneously lead to a Pauli string of errors (multi-qubit Pauli operators), e.g. $\hat{E} = \hat{X}_2\hat{X}_5$. Error correction fails if the correction operation \hat{C}_s suggested by the decoder, in combination with the error string \hat{E} , connects the edges of the code. For example, the error string \hat{E} touches the stabilizer operator $\hat{S}_5 = \hat{Z}_1\hat{Z}_2\hat{Z}_4\hat{Z}_5$ on two data qubits and $\hat{S}_8 = \hat{Z}_5\hat{Z}_6\hat{Z}_8\hat{Z}_9$ on a single data qubit, thus only the measurement of \hat{S}_8 will return with a (-1) value, as shown on Fig. 1.8(b). The decoder can confuse this outcome with a single \hat{X}_9 error which provides the same error syndrome, depicted on Fig. 1.8(c). Applying the corresponding correction $\hat{C}_s = \hat{X}_9$ would result in a logical error in the distance-3 surface code, since $\hat{C}_s\hat{E} = \hat{X}_2\hat{X}_5\hat{X}_9$ is a logical X operator. To test these and further examples, an interactive visualization tool is available at [102].

The surface code has the advantage of having fast and accurate decoders available [103–107]. The simplest quantum error correction experiment is a memory experiment, where a surface code logical state $|0_L\rangle$ ($|+_L\rangle$) is prepared by initializing all data qubits to $|0\rangle$ ($|+\rangle$), that is followed by one or more rounds of stabilizer measurement, and finally the measurement of all data qubits in the Z basis (X basis). In this case, the decoding and the evaluation of logical errors can be performed in post-processing, after the data is collected by the measurements [63]. Active error correction is enabled by feedforward operations, referring to the case when the measurement outcomes are used to determine future quantum operations. Utilizing fast feedforward operations, error correction can be performed in real-time, which is a requirement for universal fault-tolerant quantum computation [108].

The surface code shows threshold behavior, which means that if the strength of physical errors is below a threshold p_{th} , then the code performs increasingly better as the code size is increased, with vanishing logical error for asymptotically large code size [99, 100]:

$$p_L \propto \left(\frac{p}{p_{\text{th}}}\right)^{\frac{d+1}{2}}, \quad (1.33)$$

where p is the physical error rate and $\frac{d+1}{2}$ is the minimal number of simultaneous single-qubit errors that can cause a logical error for odd distance d . The error threshold of the surface code is $p_{\text{th}} \approx 1\%$ for realistic (circuit-level) noise which is within reach for state-of-the-art solid-state quantum hardware, e.g. superconducting qubits [63, 109–111]. The first error correction experiments with semiconductor spin qubits realized the phase-flip repetition code [112, 113] with a single round of measurement and without feed-forward; however, full-fledged quantum error correction (e.g. the surface code) has yet to be realized with this platform.

Besides experimental progress, another important line of research is the simulation of quantum error correction codes to forecast their future performance. The effect of Pauli errors during quantum error correction is well-understood due to the efficient simulability [12] and the existence of mappings to classical disordered spin models [114]. However, the exploration of more realistic error models (including e.g. gate errors and measurement errors) is an ever-present challenge. Recently, efficient large-scale numerical simulations of coherent errors became feasible, due to a newly developed technique [115]. This technique was originally used to investigate the effect of uniform coherent errors in the surface code, then follow-up works extended this to arbitrary planar-graph surface codes [116] and the presence of phenomenological readout errors [117].

Chapter 2

Triplet blockade: mechanism for spin-to-supercurrent conversion

This chapter is based on publications [I.](#) and [II.](#)

Superconducting materials conduct electricity without resistance below a critical temperature, due to the condensation of electrons into a macroscopic quantum state. In this state, electrons are paired up forming Cooper pairs [118].

A Josephson junction (depicted on Fig. 2.1) is a superconducting device formed by two superconductors separated by a thin insulating barrier, allowing Cooper pairs to tunnel coherently across the junction and giving rise to unique quantum phenomena. The coherent tunneling of these pairs is described by the Josephson effect [119], which leads to a characteristic *current-phase relation*,

$$I(\phi) = I_c \sin(\phi). \quad (2.1)$$

This famous equation shows that the dissipationless Cooper-pair current (I) flowing through the junction at zero voltage bias (i.e. without any applied voltage) is driven by the quantum mechanical phase difference (ϕ) between the two superconductors, up to a maximum amplitude, that is the critical current (I_c). This phenomenon is called the direct current (dc) Josephson effect. In case of non-zero voltage bias, the phase difference ϕ changes over time, producing oscillating supercurrent at a frequency proportional to the applied voltage, that is known as the alternating current (ac) Josephson effect.

These properties have enabled the use of Josephson junctions in a variety of applications, from classical superconducting electronics to quantum information processing. For instance, Josephson junctions are the elementary building blocks of superconducting qubits (outlined in Sec. 1.2.2). Beyond qubit realization, Josephson junctions are crucial components in devices such as ultra-sensitive magnetometers (SQUIDs), amplifiers, mixers, and switches, also used for readout and control in qubit experiments [120].

When the insulating layer (weak link) of the Josephson junction is a non-magnetic tunnel barrier, a zero phase difference is energetically favorable in the absence of supercurrent, which is described by a positive critical current, $I_c > 0$. In case of a so-called π junction, a π phase shift appears in the current-phase relation,

$$I(\phi) = I_c \sin(\phi + \pi) = -I_c \sin(\phi), \quad (2.2)$$

resulting in a reversed supercurrent. This supercurrent reversal has been observed in ferromagnetic weak links [122, 123], out-of-equilibrium electron systems [124] and semiconductor quantum dot junctions [125, 126]. Hybrid superconductor-semiconductor nanostructures, such as Cooper

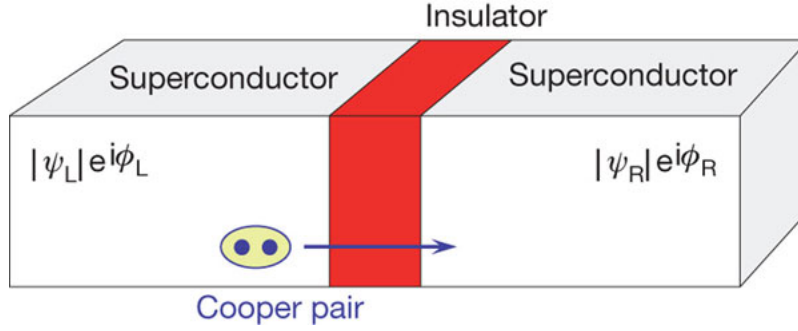


Figure 2.1: Schematics of a "Josephson junction", a tunnel junction with superconducting leads. The superconductors have superconducting phase ϕ_L and ϕ_R respectively, which gives rise to a phase difference $\phi = \phi_R - \phi_L$, driving a dc Josephson current across the junction. Figure taken from Ref [121].

pair splitters and Andreev qubit prototypes, are also fabricated and subject to intense research at Budapest University of Technology and Economics, Department of Physics, in the group of Szabolcs Csonka [127–138].

In this chapter, I present the theoretical study of a Josephson junction with a double quantum dot (DQD) as a weak link. Using numerical simulations and analytical calculations in the perturbative regime, I compute the equilibrium critical current and describe two intriguing phenomena: even-odd effect related to the charge configuration of the DQD implying the $0 - \pi$ junction behavior, furthermore the magnetically induced triplet blockade of the $(1, 1)$ charge state. I also discuss the opportunity for the latter to provide a coupling mechanism between spin qubits and (topological or non-topological) superconducting qubits. My results are built upon previous theoretical studies [88, 139–143], and a recent experiment that was conducted by my collaborators [144].

The rest of this chapter is organized as follows. In Sec. 2.1, I introduce a simple model based on zero-bandwidth approximation that describes the double quantum dot Josephson junction. In Sec. 2.2, I present my numerical results regarding the critical current. In Sec. 2.3, I discuss the switching of the sign of the supercurrent, the even-odd effect. In Sec. 2.4, I discuss magnetic field dependence, and triplet blockade in the $(1, 1)$ charge sector of the serially coupled double quantum dot. In Sec. 2.5, I discuss the effect of spin-orbit interaction and the relation of my results to experiment. In Sec. 2.6, I outline two mechanisms utilizing the triplet blockade: spin-to-supercurrent conversion and coupling to superconducting qubit.

2.1 Simple model of a double quantum dot Josephson junction

One can describe the double quantum dot Josephson junction based on a minimal model (Fig. 2.2(a)), replacing the superconducting leads by single lattice sites that can host at most one pair of quasi-particles. This method is also known as *zero-bandwidth* (ZBW) approximation [145, 146]. Assuming the leads are coupled to a Cooper pair reservoir, Josephson current can flow through the junction. For the sake of simplicity, I only take into account a single orbital in the quantum dots, therefore I use a four-site spinful fermionic hopping model with superconducting pairing on the leads. The Hamiltonian includes left and right superconducting leads $\hat{\mathcal{H}}_L$ and $\hat{\mathcal{H}}_R$,

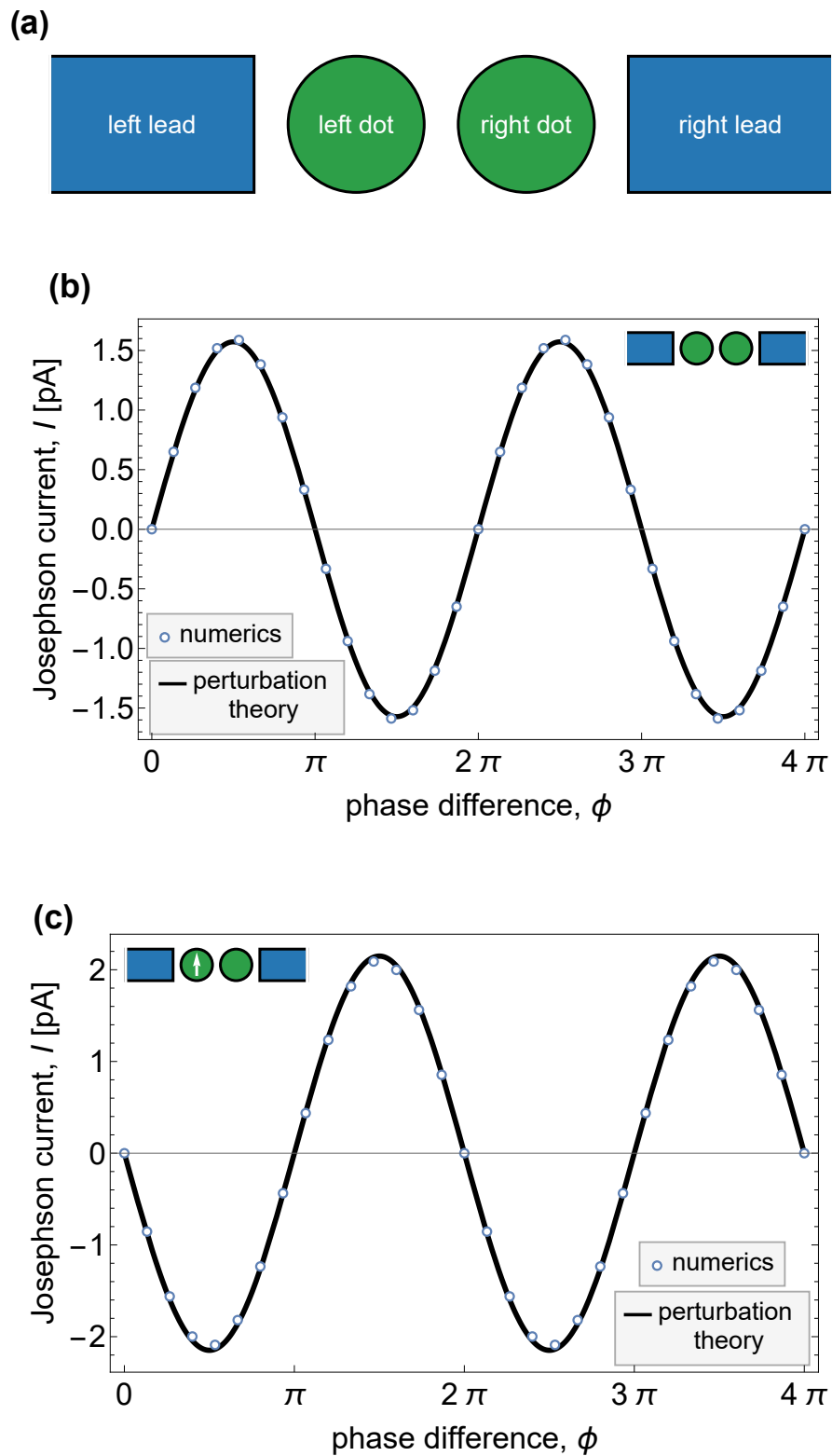


Figure 2.2: Current-phase relation in ZBW approximation. (a) Schematics of the Josephson junction with a serially coupled DQD. (b) Sinusoidal current-phase relation for the empty DQD. (c) Current-phase relation when the left dot is occupied by a single electron. In this case, the sinusoidal Josephson current-phase relation is shifted by a phase π with respect to (b). Parameters: see Table 2.1.

the double quantum dot Hamiltonian $\hat{\mathcal{H}}_{\text{DQD}}$ and dot-lead tunneling terms $\hat{\mathcal{H}}_{\text{tL,tR}}$:

$$\hat{\mathcal{H}} = \hat{\mathcal{H}}_{\text{L}} + \hat{\mathcal{H}}_{\text{tL}} + \hat{\mathcal{H}}_{\text{DQD}} + \hat{\mathcal{H}}_{\text{tR}} + \hat{\mathcal{H}}_{\text{R}}, \quad (2.3a)$$

$$\hat{\mathcal{H}}_{\text{L}} = \Delta \left(e^{-i\phi/2} \hat{c}_{\text{L}\downarrow}^\dagger \hat{c}_{\text{L}\uparrow}^\dagger + \text{h.c.} \right), \quad (2.3b)$$

$$\hat{\mathcal{H}}_{\text{tL}} = t_{\text{L}} \sum_{s=\downarrow,\uparrow} \left(\hat{c}_{\text{L},s}^\dagger \hat{d}_{\text{L},s} + \text{h.c.} \right), \quad (2.3c)$$

$$\begin{aligned} \hat{\mathcal{H}}_{\text{DQD}} = & \varepsilon_{\text{L}} \hat{n}_{\text{L}} + \varepsilon_{\text{R}} \hat{n}_{\text{R}} + \frac{U_{\text{L}}}{2} \hat{n}_{\text{L}} (\hat{n}_{\text{L}} - 1) + \frac{U_{\text{R}}}{2} \hat{n}_{\text{R}} (\hat{n}_{\text{R}} - 1) + U' \hat{n}_{\text{L}} \hat{n}_{\text{R}} \\ & + \tau \sum_{s=\downarrow,\uparrow} \left(\hat{d}_{\text{L},s}^\dagger \hat{d}_{\text{R},s} + \text{h.c.} \right) + \frac{g^* \mu_{\text{B}} B}{2} \sum_{\ell=\text{L,R}} (\hat{n}_{\ell\downarrow} - \hat{n}_{\ell\uparrow}), \end{aligned} \quad (2.3d)$$

$$\hat{\mathcal{H}}_{\text{tR}} = t_{\text{R}} \sum_{s=\downarrow,\uparrow} \left(\hat{c}_{\text{R},s}^\dagger \hat{d}_{\text{R},s} + \text{h.c.} \right), \quad (2.3e)$$

$$\hat{\mathcal{H}}_{\text{R}} = \Delta \left(e^{i\phi/2} \hat{c}_{\text{R}\downarrow}^\dagger \hat{c}_{\text{R}\uparrow}^\dagger + \text{h.c.} \right), \quad (2.3f)$$

where $\hat{c}_{\ell,s}$'s, $\hat{d}_{\ell,s}$'s are the fermionic modes for the leads and the dots respectively, and the $\hat{n}_{\ell} = \sum_s \hat{d}_{\ell,s}^\dagger \hat{d}_{\ell,s}$ are particle number operators for the dots. This model has several parameters: Δ is the superconducting gap, ϕ is the phase difference between the superconducting leads, $\varepsilon_{\text{L/R}}$ are on-site energies, $U_{\text{L/R}}$ are charging energies of the dots, U' is the interdot charging energy and B is the Zeeman field applied to control the spin state of the DQD. The latter is assumed to be small enough to retain superconductivity. I model the DQD with an effective identical g-factor on both dots. Comparison with the experiment reveals that the electron g-factor is strongly renormalized, $g^* = 15.9$ [144], which was also observed in other experiments with semiconductor nanowires [37, 147]. Quasiparticles can tunnel through the junction with dot-lead tunneling amplitudes $t_{\text{L/R}}$ and interdot tunneling τ . The Fock space of this model is $4^4 = 256$ -dimensional which makes it numerically accessible.

My main quantity of interest is the *current operator* which is the quantum mechanical time derivative of the particle number operator and defined for a cross-section of the system [74], e.g. for the interface between the left dot and the left lead it is given by

$$\hat{j}_{\text{L}} = -\frac{i}{\hbar} \left[\hat{n}_{\text{L}}, \hat{\mathcal{H}}_{\text{tL}} \right] = t_{\text{L}} \frac{i}{\hbar} \sum_{s=\downarrow,\uparrow} \left(\hat{c}_{\text{L},s}^\dagger \hat{d}_{\text{L},s} - \text{h.c.} \right). \quad (2.4)$$

The zero-temperature Josephson current is the ground state expectation value of the current operator,

$$I(\phi) = \left\langle \Psi_0(\phi) \left| \hat{j}_{\text{L}} \right| \Psi_0(\phi) \right\rangle, \quad (2.5)$$

where $|\Psi_0(\phi)\rangle$ is the phase-dependent ground state of the full system. Provided by the Hellmann-Feynman theorem, this is equivalent to calculating the phase derivative of the total ground state energy [118],

$$I(\phi) = \frac{2e}{\hbar} \frac{\partial E_0}{\partial \phi}, \quad (2.6)$$

where $2e$ is the electric charge of a Cooper pair. This expression shows that the phase derivative of the total ground state energy gives the Josephson current. Consequently, in order to determine the leading order Josephson current, it is enough to compute phase dependent ground state energy corrections. However, in the following I will use only Eq. (2.5) to this end.

Eq. (2.5) can be easily evaluated numerically, once the ground state wavefunction $\Psi_0(\phi)$ is found. Therefore I perform the exact diagonalization of the 256×256 Hamiltonian matrix, finding its eigenvalues and eigenstates. Beyond the Josephson current-phase relation (Fig. 2.2(b) and (c)), one can compute the current as a function of on-site energies ε_L and ε_R while other parameters are fixed. A diagram that visualizes the equilibrium charge states of the two serially coupled dots as a function of the on-site energies (or gate voltages) is called the *charge stability diagram*, illustrated in Fig. 2.3. I will use the term *supercurrent charge stability diagram* for the charge stability diagram obtained by the Josephson current calculation. It provides a useful characterization of the system as the ground state dot occupations are precisely tuned by the on-site energies. I also study the stability diagram in the presence of Zeeman field B (i.e. magnetic stability).

Another straightforward approach to the problem is perturbation theory in the tunnel couplings. Assuming $t_{L/R}, \tau \ll \Delta$, I consider all the tunneling terms (dot-lead tunnelings and interdot tunneling) as perturbation. In this case, the elementary process contributing to the supercurrent is when a Cooper pair is transferred through the junction, thus the leading-order Josephson current is carried by 6th-order tunneling processes [148]. Computing corrections to the ground state wavefunction up to 5th-order and using Eq. (2.5), allows me to obtain analytical results for the current, in the weak tunneling limit.

The investigated system is realized by my experimental collaborators with quantum dots defined in InAs nanowire [144]. In the experiment, supercurrent through the junction is directly measured and on-site energies ε_L and ε_R are controlled by the plunger gate voltages P_1 and P_2 , respectively. The relations between plunger gate voltages and on-site energies are given by

$$\varepsilon_L = -\frac{U_L}{2} - U' - \alpha_{11}eP_1 - \alpha_{12}eP_2, \quad (2.7a)$$

$$\varepsilon_R = -\frac{U_R}{2} - U' - \alpha_{21}eP_1 - \alpha_{22}eP_2, \quad (2.7b)$$

with the lever arms $\alpha_{11} = 0.2$, $\alpha_{12} = 0.011$, $\alpha_{21} = 0.013$, $\alpha_{22} = 0.124$.

2.2 Numerical simulations

A suitable parameter set that produces good agreement with the experimental data is summarized in Table 2.1. These parameters were extracted by performing a global fit to the experimental data [144].

In the experiment, the DQD weak link was formed by an electrostatically gated InAs nanowire, see Fig. 2.4(a) and (b). A phase-sensitive measurement scheme was employed, where the DQD was embedded in a superconducting quantum interference device (SQUID), shown in Fig 2.4(c), enabling a signful measurement of I_c . The current-phase relation was measured with the reference arm of the SQUID opened with its electrostatic gate so that it exhibits a higher critical current than the DQD arm. Due to this asymmetry, the phase drop over the DQD junction is determined by the magnetic flux Φ through the SQUID loop area (Fig. 2.4(e)) [125, 150], which is proportional to the applied out-of-plane magnetic field B_\perp . The switching current I_{sw} of the SQUID was measured by ramping a current bias and recording the bias current value when the junction switches to the resistive state marked by a threshold voltage drop of the order of 10 μ V. This relation is described by the formula

$$I_{sw} = I_{ref} + I_{DQD} \sin \phi, \quad (2.8)$$

where $\phi = 2\pi\Phi/\Phi_0 = 2\pi(B_\perp - B_o)/B_p$, with $B_p \approx 1.7$ mT being the magnetic field periodicity corresponding to a flux change equal to the superconducting flux quantum $\Phi_0 = h/2e$ and B_o

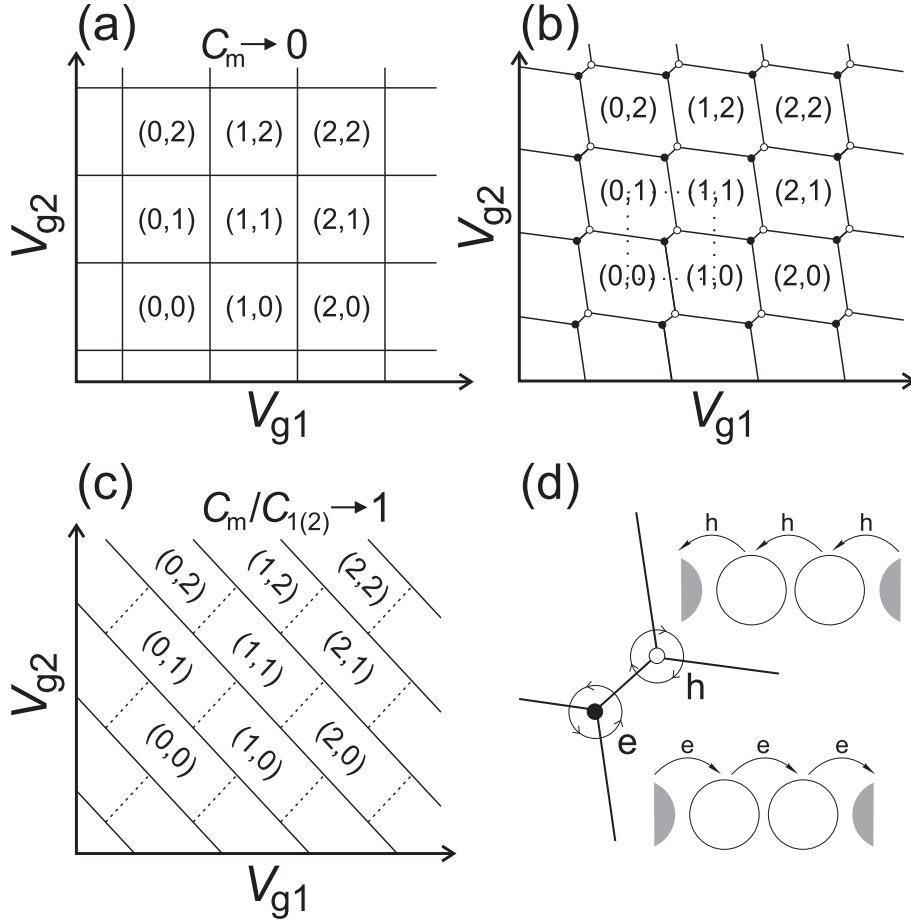


Figure 2.3: Schematic charge stability diagram of a double quantum dot system (without superconducting leads) for (a) small, (b) intermediate, and (c) large interdot capacitive coupling. The gate voltages V_{g1} and V_{g2} are controlling the on-site energies of the two dots, respectively. Higher gate voltage corresponds to lower on-site energies, which makes higher charge occupation of the electronic ground state energetically more favorable. The equilibrium charge on each dot in each domain is denoted by (N_1, N_2) . When the interdot capacitive coupling is small (a), the different charge occupation regions form a square-grid-like structure. Increasing the interdot capacitive coupling (b) distorts this structure and gives rise to a so-called honeycomb pattern of the charge boundaries. They are called Coulomb diamonds, because of the shape of the domains, and since the electrons need to overcome the energy penalty of Coulomb repulsion when they are occupying the same quantum dot. Large interdot capacitive coupling (c) makes the charge domains diagonal. The two kinds of triple-points corresponding to the electron transfer process (\bullet) and the hole transfer process (\circ) crossing the charge boundaries are illustrated in (d). Figure taken from Ref. [149].

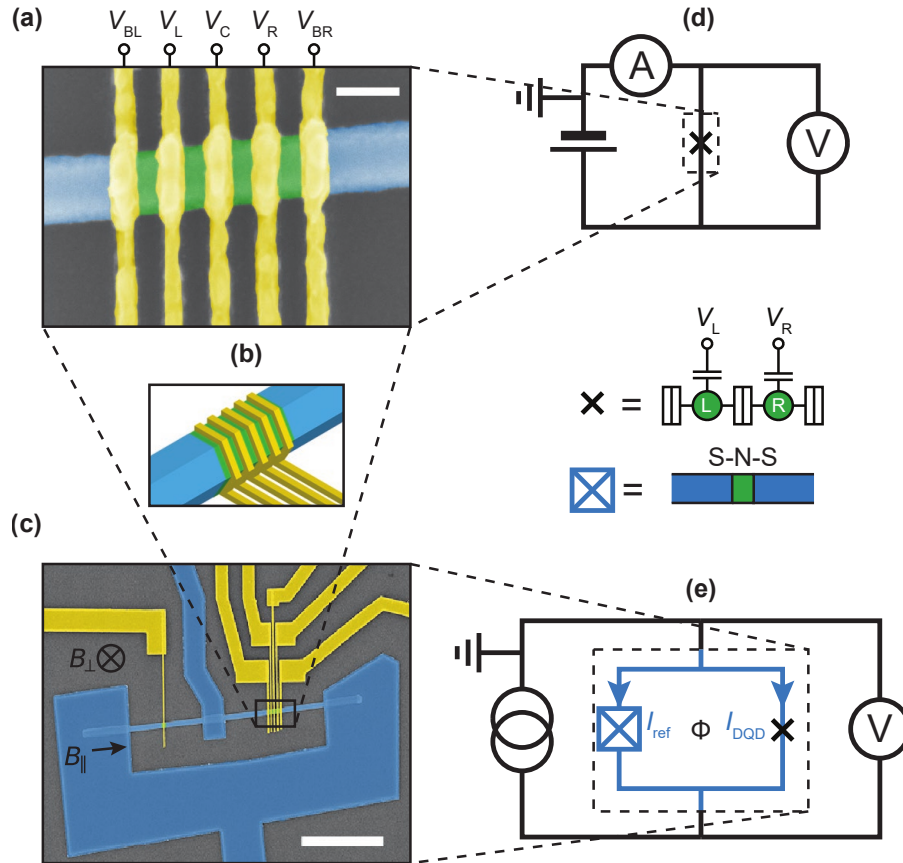


Figure 2.4: Device layout realized in the experiment [144]. (a) Color-enhanced electron micrograph of the nanowire DQD junction with five wrap-around gates (yellow) which provide the confining potential. The V_{BL} , V_C and V_{BR} gate voltages define the barriers, while V_L and V_R control the number of electrons on the dots. The scale bar denotes 100 nm. (b) Perspective drawing of the DQD junction highlighting the conformal gates. (c) Color-enhanced electron micrograph of the DC SQUID made of superconducting NbTiN film (in blue) with the reference junction in the left arm and the DQD junction in the right arm. The scale bar denotes $2 \mu\text{m}$. (d) The circuit diagram for the normal-state characterization of the DQD, providing charge stability similar to Fig. 2.5(b). (e) The measurement scheme of the switching current measurements in the SQUID geometry.

being the offset perpendicular magnetic field. The switching current values I_{ref} and I_{DQD} represent the reference arm and the DQD junction contributions, respectively. In the measurements $I_{\text{ref}} > 5|I_{\text{DQD}}|$ was always fulfilled, enabling a reliable observation of the supercurrent reversal in the DQD.

The supercurrent charge stability diagram measured by my experimental collaborators is shown in Fig. 2.5(a), in comparison with my numerical result, Fig. 2.5(b). These two figures suggest good qualitative agreement between theory and experiment. Furthermore, the DQD charge occupation labels in Fig. 2.5(b) show that there is an even-odd pattern depending on the total parity of the charge configuration. The magnetic field dependence of the supercurrent charge stability diagram is also computed for $\varepsilon_L = \varepsilon_R$ and it is depicted in Fig 2.6. The even-odd pattern remains intact with one extra feature: in the (1,1) charge sector, the critical current is suppressed when the ground state is tuned from a singlet configuration to a triplet configuration.

The detailed discussion of the even-odd effect and the triplet blockade is the subject of the following sections.

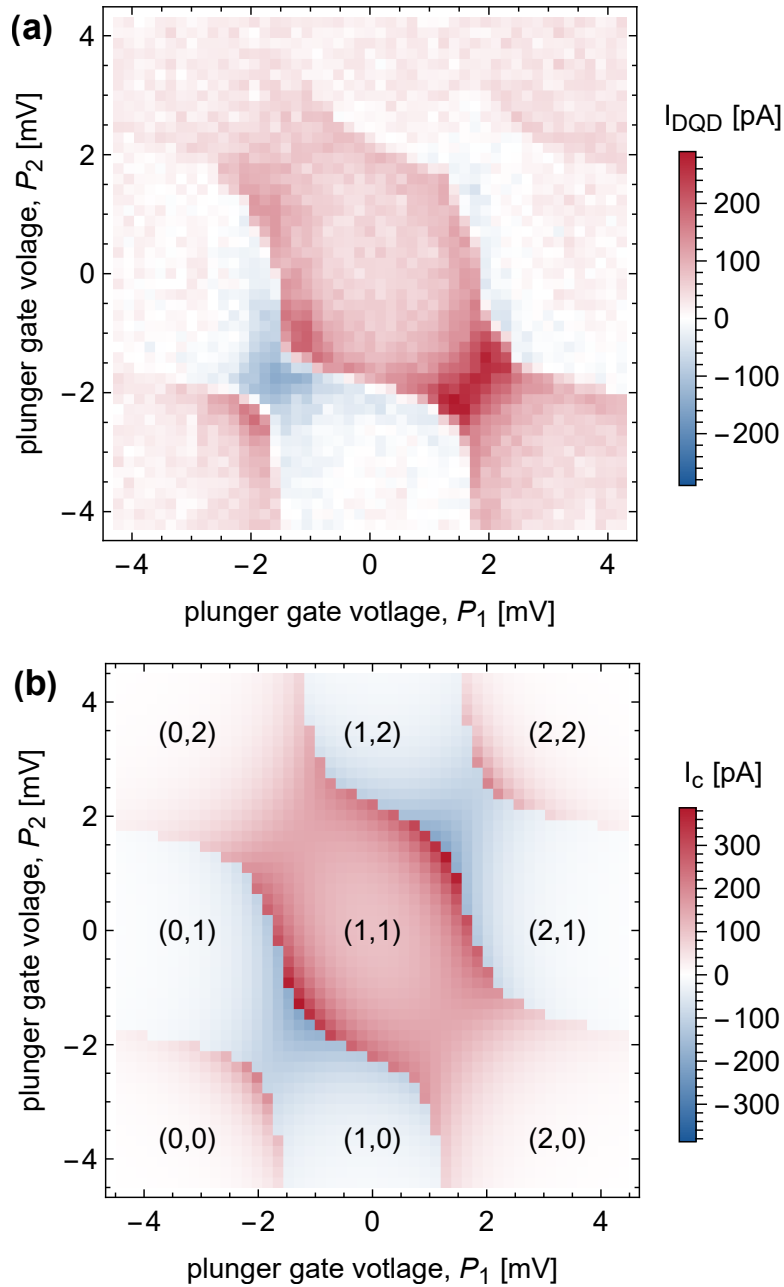


Figure 2.5: Supercurrent charge stability diagrams. (a) Supercurrent charge stability diagram from experimental data (plunger gate voltage offset removed) with an even-odd pattern, positive supercurrent in the even sectors and negative in the odd sectors. (b) Numerical simulation based on the ZBW model with electron occupation numbers. Parameters: see Table 2.1 and Eq. (2.7).

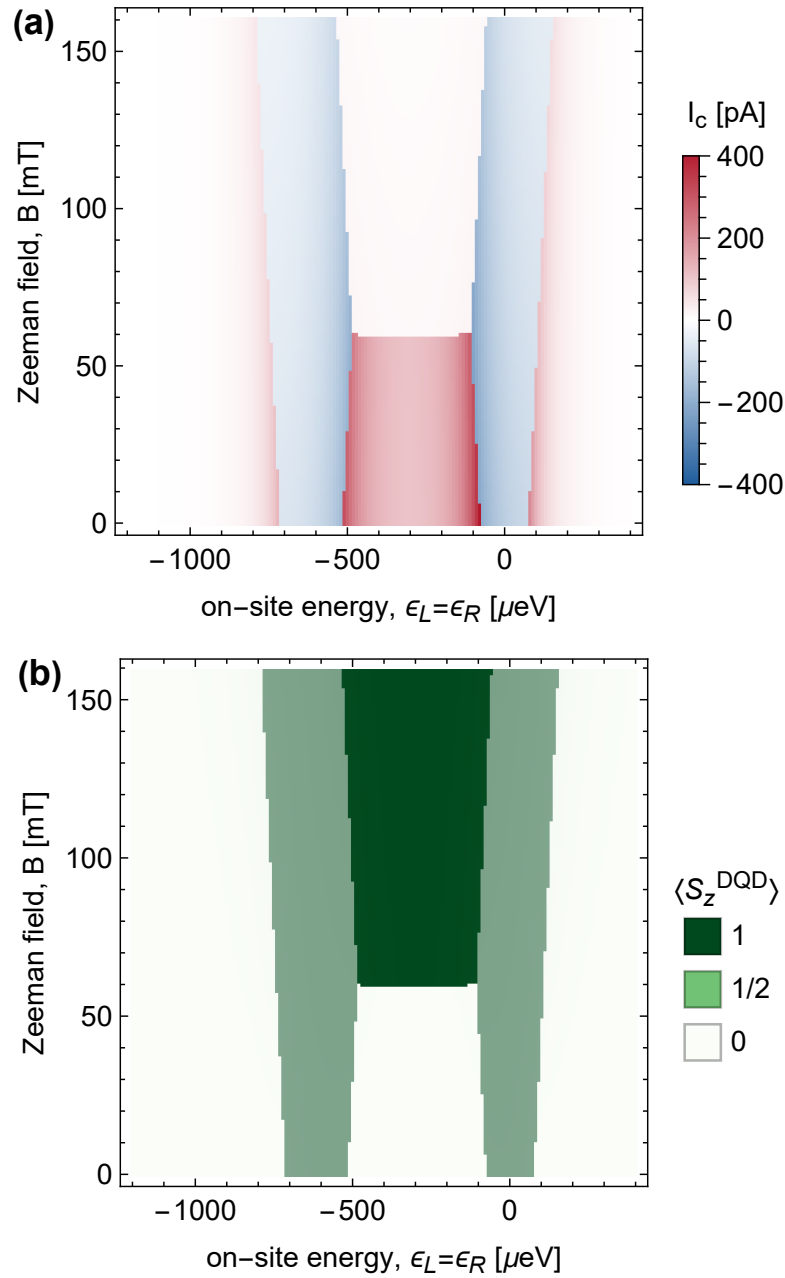


Figure 2.6: Magnetic stability diagram. (a) Supercurrent charge stability diagram along the line $\epsilon_L = \epsilon_R$, in the presence of Zeeman field obtained numerically. The even-odd pattern is still present with increasing magnetic field, however the amplitude of the current abruptly decreases in the middle of the diagram (in the (1,1) charge sector) when the magnetic field exceeds the value $B \approx 60$ mT. (b) Ground state expectation value of the z -component of the total DQD spin reveals that the supercurrent is blocked in the triplet configuration. Parameters: see Table 2.1.

Quantity	Value
U_L	596.6 μeV
U_R	465.9 μeV
U'	41.5 μeV
Δ	200 μeV
τ	85 μeV
g^*	15.9
t_L	65 μeV
t_R	65 μeV

Table 2.1: Parameters for the numerical simulation of the double quantum dot Josephson junction. The parameters listed here are the result of a global fit to experimental data [144].

2.3 Even-odd effect

The occupation of the DQD based on the total fermion number parity can be classified as even, or odd. For example, an empty DQD has even parity, but when either of the dots are occupied by a single-electron, it corresponds to odd parity. In the weak tunneling regime, when the dot-lead and dot-dot tunnel amplitudes are small compared to the superconducting gap Δ and the on-site Coulomb repulsion $U_{L/R}$, the zero-temperature Josephson current–phase relation is sinusoidal (as shown in Fig 2.2(b)), with a positive coefficient in the even parity sector:

$$I(\phi) = |I_c(\varepsilon_L, \varepsilon_R)| \sin(\phi), \quad (2.9)$$

where the critical current I_c is dependent on the charge occupations (controlled by the on-site energies $\varepsilon_{L,R}$), and the other parameters as well (listed in Table 2.1). In the odd parity sector, which is also called the π -junction regime, it is shifted by a phase π , thus reversed as

$$I(\phi) = |I_c(\varepsilon_L, \varepsilon_R)| \sin(\phi + \pi) = -|I_c(\varepsilon_L, \varepsilon_R)| \sin(\phi). \quad (2.10)$$

This feature is usually called the *even-odd effect* [148, 151].

To understand this phenomenon, I turn to the limit when the dot-dot tunnel amplitude is also small $\tau \ll \Delta, U_{L/R}$ and use the perturbative approach. In (time-independent, non-degenerate) perturbation theory, the general assumption is that the system is slightly altered from a known, exactly solvable Hamiltonian, $\hat{\mathcal{H}} = \hat{\mathcal{H}}_0 + \lambda \hat{V}$, where $\hat{\mathcal{H}}_0$ is the unperturbed Hamiltonian, \hat{V} is a small perturbation, and $0 \leq \lambda \leq 1$ is a formal expansion parameter, with $\lambda = 0$ corresponding to no perturbation and $\lambda = 1$ to the full perturbation. The energy levels, $E_n^{(0)}$, and the eigenstates, $|\psi_n^{(0)}\rangle$, of the unperturbed Hamiltonian $\hat{\mathcal{H}}_0$ are known. The energy levels and eigenstates of the perturbed ("full") Hamiltonian $\hat{\mathcal{H}}$ determined by the time-independent Schrödinger equation,

$$\left(\hat{\mathcal{H}}_0 + \lambda \hat{V}\right) |\psi_n(\lambda)\rangle = E_n(\lambda) |\psi_n(\lambda)\rangle. \quad (2.11)$$

Assuming that the eigenenergies $E_n(\lambda)$ and eigenstates $|\psi_n(\lambda)\rangle$ are analytical functions of the parameter λ , they can be expanded in power series,

$$E_n(\lambda) = E_n^{(0)} + \lambda E_n^{(1)} + \lambda^2 E_n^{(2)} + \dots, \quad (2.12)$$

$$|\psi_n(\lambda)\rangle = |\psi_n^{(0)}\rangle + \lambda |\psi_n^{(1)}\rangle + \lambda^2 |\psi_n^{(2)}\rangle + \dots, \quad (2.13)$$

providing the solution to the perturbed problem, when $\lambda = 1$. Substituting these expressions to the time-independent Schrödinger equation, Eq. (2.11), one can derive the solutions up to

arbitrary order. For example, the perturbative corrections to the state $|\psi_n^{(0)}\rangle$, up to second order read as

$$|\psi_n(\lambda)\rangle = |\psi_n^{(0)}\rangle + \lambda \sum_{m \neq n} \frac{\langle \psi_m^{(0)} | \hat{V} | \psi_n^{(0)} \rangle}{E_n^{(0)} - E_m^{(0)}} |\psi_m^{(0)}\rangle \quad (2.14a)$$

$$+ \lambda^2 \sum_{m \neq n} \sum_{\ell \neq n} \frac{\langle \psi_m^{(0)} | \hat{V} | \psi_\ell^{(0)} \rangle \langle \psi_\ell^{(0)} | \hat{V} | \psi_n^{(0)} \rangle}{(E_n^{(0)} - E_m^{(0)}) (E_n^{(0)} - E_\ell^{(0)})} |\psi_m^{(0)}\rangle \quad (2.14b)$$

$$- \lambda^2 \sum_{m \neq n} \frac{\langle \psi_m^{(0)} | \hat{V} | \psi_n^{(0)} \rangle \langle \psi_n^{(0)} | \hat{V} | \psi_n^{(0)} \rangle}{(E_n^{(0)} - E_m^{(0)})^2} |\psi_m^{(0)}\rangle \quad (2.14c)$$

$$- \frac{\lambda^2}{2} |\psi_n^{(0)}\rangle \sum_{m \neq n} \frac{|\langle \psi_m^{(0)} | \hat{V} | \psi_n^{(0)} \rangle|^2}{(E_n^{(0)} - E_m^{(0)})^2} + \mathcal{O}(\lambda^3). \quad (2.14d)$$

Each term in this lengthy formula contains (product of) matrix elements of the perturbation \hat{V} , and (unperturbed) energy differences in the denominators. The product of the matrix elements describes transitions to intermediate states $|\psi_\ell^{(0)}\rangle$. One can think of an arbitrary k th order term as k -step process that includes $(k - 1)$ intermediate states.

In the case of the DQD Josephson junction the unperturbed Hamiltonian includes the superconducting leads, and the DQD without the interdot tunneling term ($\tau = 0$),

$$\hat{\mathcal{H}}_0 = \hat{\mathcal{H}}_L + \hat{\mathcal{H}}_R + \hat{\mathcal{H}}_{\text{DQD}}(\tau = 0), \quad (2.15)$$

and the perturbation includes all the tunneling terms (cf. Eq. (2.3)),

$$\hat{V} = \hat{\mathcal{H}}_{tL} + \hat{\mathcal{H}}_{tR} + \tau \sum_{s=\downarrow, \uparrow} \left(\hat{d}_{L,s}^\dagger \hat{d}_{R,s} + \text{h.c.} \right). \quad (2.16)$$

Since the leading order contributions to the Josephson current, Eq. (2.5), are 6th-order, I computed the ground state $|\Psi_0(\phi)\rangle$ up to 6th-order in perturbation theory, using Wolfram Mathematica [152]. Substituting the result to Eq. (2.5), the thus obtained leading-order Josephson current can be described as a sum of contributions (with coefficient $t_L^2 t_R^2 \tau^2$), where each contribution can be visualized as a six-step process in which a Cooper pair from one lead is transported over to the other lead [148]. Four example processes are shown in Fig. 2.7. The intermediate states of such processes are virtual states, in the sense that they have a high energy, either due to quasiparticle excitations, or due to Coulomb repulsion.

My calculations show that for any given ground state at phase difference $\phi = \pi/2$, each of these contributions (i.e. each path) has the same sign, which is identical to the sign of the supercurrent. Furthermore, as depicted in Fig. 2.2(b), for the single-electron DQD ground state I find a reversed current, also confirmed by numerics. For the empty DQD and the two-electron singlet, triplet ground states I did not observe any sign reversal. Similarly, the four-electron ground state has no sign reversal, but the three-electron ground state also exhibits a reversed supercurrent. These results suggest that in this model the fermion parity of the ground state determines whether the sign in the Josephson current is plus or minus (corresponding to even or odd parity, respectively) because it is conserved on the superconducting leads, but changes when an extra electron is added to the double dot. Since for any studied ground state, each six-step process gives the same sign contributing to the critical current, I conclude that leading-order perturbation theory provides a suitable framework to understand the even-odd effect.

I also have unpublished numerical results for Josephson junctions with a single and a triple quantum dot (considering only a single orbital in each dot) suggesting that the same argument holds for any number of quantum dots in the Josephson junction, for linear geometries (chains of quantum dots).

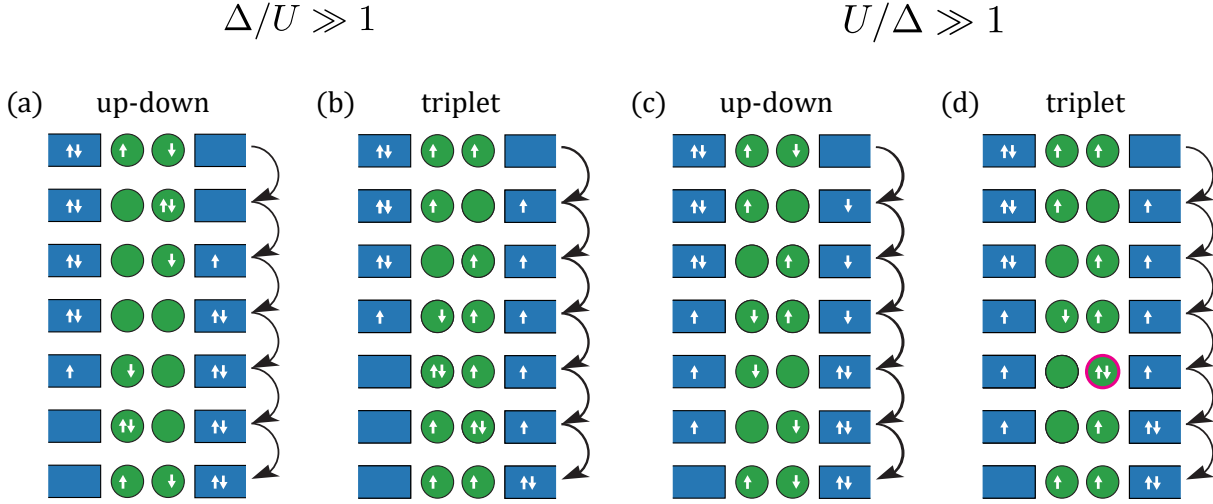


Figure 2.7: Example processes contributing to the Josephson current through the double dot. (a) Up-down process with intermediate states lacking quasiparticles, hence less penalized by a large gap $\Delta \gg U$. (b) Triplet process with intermediate states that all have at least one quasiparticle, hence more penalized by Δ . (c) Up-down process with all states having at most singly occupied quantum dots, hence exempt from Coulomb energy penalty. (d) Triplet process with an intermediate state that has a doubly occupied quantum dot and hence energetically penalized in the $U \gg \Delta$ regime.

2.4 Triplet blockade

In this section, I provide a detailed discussion of the suppressed triplet critical current by presenting simple arguments for a strong triplet blockade in two different limiting cases: the large-gap limit $\Delta \gg U$, and the strong-Coulomb-repulsion limit $U \gg \Delta$. Here, $U_L = U_R = U$ is assumed and I will use this simplifying assumption throughout this subsection. I also outline a process-counting argument that supports *partial* triplet blockade in the intermediate regime $\Delta \approx U$.

For the simple arguments, (1) the interdot Coulomb repulsion U' is disregarded, (2) instead of the singlet ground state, I address the case when the initial state holds an \uparrow -spin electron in the left dot and a \downarrow -spin electron in the right dot (the *up-down* state), (3) I describe the Josephson current as a perturbative effect.

First, I revisit the case of the large-gap limit $\Delta/U \gg 1$, which was described in Refs. [142, 153]. In this case, the reason for the triplet blockade is that a triplet ground state allows only such processes whose intermediate states have one or two quasiparticles in the leads. This is simply because a down-spin quasiparticle has to be transferred from the left lead through the junction to be able to recover a Cooper pair at the right lead. At the first step, there are two options: either the electron from the right dot hops to the right lead, or a down-spin quasiparticle enters the left dot from the left lead. In both cases one quasiparticle remains unpaired in one of the superconducting leads, until the down-spin quasiparticle is transferred from left to right. One example is shown in Fig. 2.7(b). In the 6th-order perturbative description of the ZBW model, the contribution of these processes scales as $\sim \Delta^{-5}$. In contrast, the up-down state allows for intermediate states where there are no quasiparticles in the leads; an example is shown in Fig. 2.7(a), where the 2nd, 4th and 6th states of the diagram do not have any quasiparticles. As a consequence, the contribution of such processes scale as $\sim \Delta^{-2}$. In conclusion, in the large-gap regime the ratio of the triplet and up-down critical currents is suppressed as $\sim \Delta^{-3}$, leading to a complete triplet blockade.

Now, I will turn to the strong-Coulomb-repulsion limit $U/\Delta \gg 1$. Consider a point in the supercurrent charge stability diagram in the vicinity of the boundary of the single-electron region and the (1,1) region, e.g. the point $P_1 = P_2 = -1.5$ mV on Fig. 2.5(b). In this case, any intermediate state that has a DQD occupation different from 1 and 2 has a large energy penalty in the corresponding energy denominator, and hence strongly suppressed. In addition, among the processes where all states have DQD occupation 1 or 2, the ones involving a doubly occupied quantum dot also comes with a large Coulomb energy penalty and hence are also suppressed.

Importantly, since the two spin-up particles cannot occupy the same site, in the processes allowed by the triplet ground state, there is at least one intermediate state that has a doubly occupied quantum dot; an example is depicted in Fig. 2.7(d), where the right dot is doubly occupied in the 5th state. The critical current of the triplet therefore scales as $\sim U^{-1}$. In contrast, for an up-down ground state, there is a process where the intermediate states have only singly occupied quantum dots, visualized in Fig. 2.7(c). The contribution of this process to the critical current scales as $\sim U^0$. In conclusion, in the strong-Coulomb-repulsion regime the ratio of the triplet and up-down critical currents is suppressed as U^{-1} , again leading to a strong triplet blockade.

Even though I have argued for a strong triplet blockade in both limiting cases $\Delta \gg U$ and $U \gg \Delta$, it is in principle possible that the triplet critical current exceeds the up-down critical current in the intermediate regime $U \approx \Delta$. Here, I argue that this is not the case. In this regime, I estimate the ratio of the triplet and up-down critical currents from the ratio of the total number of 6th-order process. In the triplet case, the total number of allowed processes is 80, whereas the up-down state allows 320 processes in total, leading to a rough estimate of the critical current ratio of 0.25. Note that the actual critical current ratio also depends on the amplitudes of every process. Due to this estimate, I expect a partial triplet blockade in this intermediate regime.

Finally, I comment on the validity of the simplifying assumptions (1) and (2) above. (1) The above considerations generalize as long as the interdot Coulomb repulsion energy U' is moderate. The analysis of the strong-Coulomb-repulsion regime could change, e.g., if U' would be a parameter tied to U , e.g. $U' = U/2$, but that is beyond the scope of my thesis. (2) The above arguments generalize to the case when a singlet ground state is considered, instead of the up-down state. One result that is changed is the order-of-magnitude estimate of the critical current ratio in the intermediate regime $U \approx \Delta$: counting the processes of the singlet ground state yields a ratio of $80/1120 \approx 0.07$, which is even smaller than the estimate $80/320 = 0.25$ quoted above. I also note that the above considerations generalize to the model with BCS leads. One technical difference is, that in BCS theory, quasiparticles have not only a spin quantum number, but also a momentum quantum number and the contributions visualized in Fig. 2.7 has to be summed with respect to the quasiparticle momentum. The scalings of the critical currents quoted above do change, but the scalings of the critical current ratios remain unchanged.

2.5 Effect of spin-orbit interaction, relation to experiment

In semiconductor quantum dot systems, depending on the material [23], usually spin-orbit interaction is also present. The effect of spin-orbit interaction (apart from the strongly renormalized g-factors) can be captured by adding an extra spin dependent interdot hopping term to the Hamiltonian Eq. (2.3d), e.g.,

$$\hat{\mathcal{H}}_{\text{spin-flip}} = \tau_x \left(-i\hat{d}_{L,\uparrow}^\dagger \hat{d}_{R,\downarrow} - i\hat{d}_{L,\downarrow}^\dagger \hat{d}_{R,\uparrow} + \text{h.c.} \right), \quad (2.17)$$

where τ_x is the spin-flip hopping amplitude. Therefore, to account for spin-orbit coupling, I refine the interdot tunneling Hamiltonian to include both spin-conserving and spin-flip tunneling amplitudes, $\tau_0 = 80 \mu\text{eV}$ and $\tau_x = 30 \mu\text{eV}$, resulting in an effective $\tau = \sqrt{\tau_0^2 + \tau_x^2} = 85 \mu\text{eV}$, which is the same as in Table 2.1.

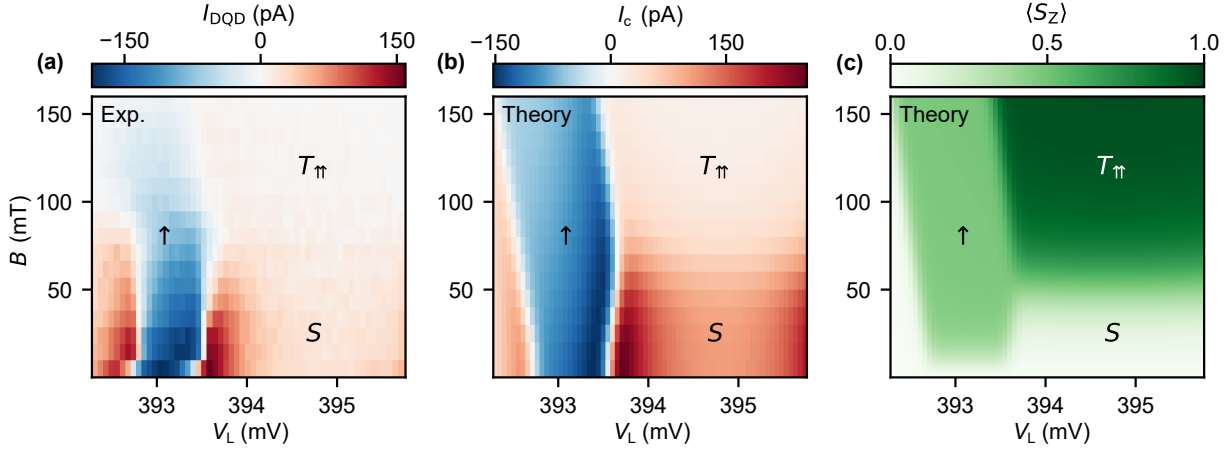


Figure 2.8: The superconducting DQD at $T \approx 50$ mK, in finite magnetic fields. (a) The experimentally measured signful supercurrent oscillation amplitude I_{DQD} as a function of plunger gate voltage and magnetic field [144]. (b) The corresponding ZBW calculation of the signful critical current. (c) The calculated spin expectation value in the ground state showing the singlet to triplet transition in the even occupied state as a function of the magnetic field. In panels (b) and (c), the parameters of Table 2.1 are used, with interdot hopping amplitude $\tau = \sqrt{\tau_0^2 + \tau_x^2}$ including spin-conserving and spin-flip hopping, $\tau_0 = 80$ μeV and $\tau_x = 30$ μeV , respectively.

During the measurements carried out by my experimental collaborators, the temperature was approximately $T \approx 50$ mK. At finite temperatures, the excited states of the full Hamiltonian are also occupied with probabilities following the Boltzmann distribution. In this case, the finite temperature Josephson current is calculated as

$$I(\phi) = \langle \hat{j}_L \rangle = \frac{1}{Z} \sum_{i=0}^{255} e^{-\beta E_i} \langle \Psi_i(\phi) | \hat{j}_L | \Psi_i(\phi) \rangle, \quad (2.18)$$

where $Z = \sum_i e^{-\beta E_i}$ is the partition function, E_i is the energy of the eigenstate $|\Psi_i(\phi)\rangle$, and $\beta = 1/(k_B T)$, where k_B is the Boltzmann constant.

The thus obtained numerical results in comparison with the measurement data are shown in Fig. 2.8. The magnetic field-dependent critical current in Fig. 2.8(b) is in good overall agreement with the measurement data depicted in Fig. 2.8(a). Compared to the sharp transition of Fig. 2.6(a), the critical current now exhibits a gradual decrease as the magnetic field is increased. Spin-flip hopping introduces a mixing (avoided crossing) between the singlet and triplet states, consequently the calculated spin expectation value in Fig. 2.8(c) shows a broadened singlet to triplet transition in the even occupied state, revealing the reason behind the gradual decrease in the critical current with increasing magnetic field – that is triplet blockade.

Finally, I comment on the validity of the previous arguments (described in Sec. 2.3 and 2.4) based on perturbation theory, in the presence of spin-flip hopping, Eq. (2.17). The spin-flip hopping term in the Hamiltonian yields new contributions to the perturbative current that have the imaginary unit (i or $-i$) appearing in the corresponding matrix elements. However, my calculations show that in this case, considering the elementary six-step processes that describe the contributions to the leading-order supercurrent, the $+1$, -1 , $+i$, $-i$ prefactors of the matrix elements of the intermediate states are always multiplied so that each of these contributions is real, and they have the same sign for a given ground state (at phase difference $\phi = \pi/2$). Therefore, I conclude that the even-odd effect remains intact in the presence of spin-flip hopping.

As long as the spin-flip hopping amplitude τ_x is small, $\tau_x \ll \tau_0$, the arguments for triplet blockade also remain valid. Although, when the spin-flip hopping amplitude is the dominant,

$\tau_x \gg \tau_0$, the situation is changed drastically. In this limit, hopping spins are always rotated in the DQD, meaning that as far as the supercurrent is concerned, the role of the triplet and the singlet ground states are essentially swapped. Instead of triplet blockade, the singlet state blocks the current. In the intermediate regime, $\tau_x \approx \tau_0$, similarly to Fig. 2.8, a broadened transition is expected, when the supercurrent is gradually decreased with increasing magnetic field, in the (1,1) charge sector.

2.6 Spin-to-supercurrent conversion, coupling to superconducting qubits

The triplet blockade is the superconducting equivalent of the Pauli spin blockade (described in Sec. 1.2.1), the cornerstone of the readout of spin qubits [23]. In this section, I outline a potential approach to utilize triplet blockade for the readout of the spin qubits and coupling to any superconducting qubit.

Based on the previous section, the (1,1) charge state of the DQD in the Josephson junction can be thought of as a tunnel barrier, whose “height” depends on the spin state of the two electrons forming the (1,1) configuration. Taking the singlet-triplet (S- T_0) qubit that was introduced in Sec. 1.2.1 as an example, in the $|T_0\rangle$ triplet state the tunnel barrier is high (small critical current, small Josephson coupling), compared to the $|S\rangle$ singlet state, where it is lower (large critical current, large Josephson coupling). Therefore, one can envision an experiment where first the DQD is isolated in the (1,1) charge configuration from the leads, then an arbitrary spin state is prepared, after that the DQD is connected to the leads and the critical current is measured. The critical current then should reveal the state of the singlet-triplet spin qubit.

In Ref. [154], coupling between a single quantum dot Josephson junction and a transmon qubit has been observed. A coupling mechanism can also be formulated based on the triplet blockade with a DQD Josephson junction. Here, I describe it for the transmon qubits, however, similar arguments can be formulated for any superconducting qubit that contains at least one Josephson junction. Note that in contrast with the Andreev spin qubit, whose spin qubit is strongly hybridized with the superconductor, the triplet blockade is utilized in the weak coupling limit. In the effective description of the transmon qubit, Eq. (1.11), the number operator \hat{n} and the phase operator $\hat{\varphi}$ act on the Hilbert space of the number of Cooper pairs on the island, i.e., the transmon degree of freedom. However, the Josephson energy E_J can be interpreted as an energy E_{JT} , if the DQD in the junction between the island and the lead contains a triplet, or E_{JS} , if the DQD contains a singlet electron pair. Consequently, the term $E_J \cos(\hat{\varphi})$ is substituted with $E_J \cos(\hat{\varphi}) + D_J \hat{\sigma}_z \cos(\hat{\varphi})$, where $E_J = (E_{JT} + E_{JS})/2$ and $D_J = (E_{JT} - E_{JS})/2$. Thus, I obtained a term in the Hamiltonian that couples the spin, $\hat{\sigma}_z = |T_0\rangle\langle T_0| - |S\rangle\langle S|$, and the transmon qubit via the phase operator $\hat{\varphi}$.

2.7 Conclusions and outlook

In this chapter, I presented a theoretical study of a Josephson junction with a double quantum dot, a minimal model system toward engineered topological superconductivity based on quantum dot chains. Based on numerical simulations and also analytical results in the perturbative regime I observed an even-odd pattern in the critical current which is confirmed by my experimental collaborators. Switching between the even and the odd states is identified as change of the ground state fermion parity and the sign of the supercurrent is uniquely determined by the ground state, up to leading order in perturbation theory.

In the (1,1) charge sector of the serially coupled double quantum dot, I observed the magnetically induced singlet-triplet ground-state transition via triplet blockade: the Josephson current

carried by the triplet ground state at high magnetic field is much suppressed compared to the current carried by the singlet ground state at low magnetic field. My theoretical results, based on the ZBW model, including spin-orbit interaction, capture the essential features of the experiment. Utilizing the triplet blockade, I outlined potential mechanisms for spin-to-supercurrent conversion and spin-to-superconducting qubit coupling.

My research summarized in this chapter was partly motivated by the application of hybrid superconductor - quantum dot systems to engineer topological superconductivity, Kitaev chains, Majorana zero modes, and ultimately, topologically protected quantum control of Majorana qubits. Since the publication of my results, pioneering experiments in the groups of Leo Kouwenhoven and Srijit Goswami at QuTech demonstrated the realization of two-site and three-site Kitaev chains using quantum dot arrays [155–159].

Chapter 3

Coherent errors in stabilizer codes caused by quasistatic phase damping

This chapter is based on publication [III](#).

As of present days, the realization of topologically protected qubits (e.g. Majorana qubits) remains elusive. Quantum error correction, with a thirty-year history from the fundamentals [9, 91] to the most recent experimental milestones [160–166], offers an alternative solution by the redundant encoding of a small number of logical qubits in a greater number of (unprotected) physical qubits. Simulation of quantum error correction codes under experimentally relevant noise models is an important task, as it helps to understand the challenges and opportunities in scaling up quantum computing platforms.

Recently, efficient large-scale numerical simulations of coherent errors became feasible, due to a newly developed technique [115]. This technique was originally used to investigate the effect of uniform coherent errors in the surface code (introduced in Sec. 1.3.3), then follow-up works extended this to arbitrary planar-graph surface codes [116] and the presence of phenomenological readout errors [117]. These studies have numerically established the threshold behavior of the surface code in the presence of coherent errors, assuming uniform unwanted rotations on the data qubits.

In this chapter, I study the performance of Pauli stabilizer codes against *quasistatic phase damping*. In this error model, physical qubits suffer coherent Z-rotations, with rotation angle randomly varying from qubit to qubit, but timewise constant throughout the entire quantum circuit; however, for each repetition of the circuit (shot) a new random value for each angle is chosen. (i) I identify quantum computing architectures where this error model is relevant and approximates $1/f$ noise. (ii) For Pauli stabilizer codes [97] I analyze how this error model is related to independent Pauli phase-flip errors. For a single cycle of error detection or error correction, I find that the two error models are equivalent. For multiple syndrome measurement cycles this is no longer true, however, quasistatic phase damping is an effective – correlated – Pauli model on the logical level. It is known that for single qubit error models stabilizer measurements asymptotically decohere the noise, that is, they cause coherent errors to converge toward probabilistic Pauli errors on the logical level [167]. My results show that for quasistatic phase damping this decoherence process is exact for all code sizes. (iii) I utilize the Fermionic Linear Optics simulation framework based on the Majorana-fermionic representation of the surface code [115], combined with phenomenological readout errors [117], to perform numerical experiments predicting the performance of the surface code in the presence of the quasistatic coherent error model. (iv) I establish a surface code error-correction threshold at a physical error rate

$p_{\text{th}} \approx 2.85\%$, including the quasistatic coherent errors and the readout errors. (v) I generate the threshold phase diagram in the plane spanned by the strengths of the coherent error and the readout error. (vi) I discuss the implications of my results for spin qubits and superconducting qubits.

The rest of this chapter is structured as follows. In Sec. 3.1, I introduce the error model of quasistatic phase damping and pinpoint the relevant qubit platforms affected by this type of noise. In Sec. 3.2, I compare and contrast my error model with independent Pauli errors through a minimal example of the 2-qubit phase-flip repetition code. I generalize this comparison for Pauli stabilizer codes in Sec. 3.3. In Sec. 3.4 and Sec. 3.5, I present my results on the combined effect of quasistatic phase damping and readout errors on the surface code, and relate these results to semiconductor spin qubits and superconducting qubits.

3.1 Quasistatic phase damping as a model of random coherent errors

In this section, I introduce *quasistatic phase damping*, the model of random coherent errors I study in the rest of this chapter. I motivate this error model by its experimental relevance for state-of-the-art solid-state quantum computing platforms: quantum-dot-based semiconductor spin qubits and superconducting qubits.

The quasistatic phase damping error model consists of coherent rotations around the z axis with a random angle for each data qubit. It is described by the unitary operator

$$\hat{U} = \prod_{j=1}^n e^{i\theta_j \hat{Z}_j}. \quad (3.1)$$

where n is the number of data qubits, and θ_j is the rotation angle of qubit j . I assume that in a single shot of a multi-cycle error detection or correction experiment, the random angles θ_j do not change for subsequent cycles. However, in a multi-shot experiment, which is required to obtain a statistical evaluation of the error correction protocol, the angles θ_j change randomly from shot to shot. These two properties are referenced by the adjective *quasistatic*. For concreteness, I assume that the angles θ_j are drawn randomly from a Gaussian distribution with zero mean and standard deviation σ , such that the random values for different qubits and different shots are statistically independent. Note that this model can be regarded as an extension of Refs. [115–117, 168], where the effect of homogeneous coherent Z rotations was studied in stabilizer codes. I also note that the simulation method I use to treat this error model generalizes in a straightforward way to more complicated angle distributions, including spatially and temporally correlated ones; that extension is beyond the scope of my thesis.

Now, let me motivate this error model by pointing out its relation to solid-state qubits. Superconducting quantum computer prototypes hosting around 100 qubits are available, and small-scale quantum error detection and correction circuits based on Pauli stabilizer codes have been implemented [69, 109–111, 169–171]. Qubit-level errors in these devices can be classified as state preparation and measurement errors, gate errors, and idle errors. Insight into the physical mechanism of idle errors is gained routinely via single-qubit Ramsey, Hahn echo, or more complex dynamical decoupling experiments.

In certain cases, the inhomogeneous dephasing time T_2^* of a superconducting qubit, measured by the Ramsey experiment, is exceeded by the qubit relaxation time T_1 ; furthermore, it is common to find that the Hahn echo improves qubit coherence, i.e., the corresponding decoherence time $T_{2,\text{echo}}$ exceeds T_2^* [172–174]. The coexistence of these two features, i.e., (i) a dephasing-limited coherence time, and (ii) a functioning Hahn echo, is consistent with, and often interpreted

as evidence for, classical electromagnetic noise that induces Larmor-frequency fluctuations. Furthermore, it is often found that the corresponding noise spectrum depending on the frequency f is proportional to $1/f$.

The quasistatic phase damping model [175, 176] I study here (see Eq. (3.1)) describes such Larmor frequency fluctuations of idling data qubits in a simplified manner. Since $1/f$ noise is dominated by the low-frequency range of the spectral density, it is reasonable to assume that the noisy component $\xi_j(t)$ of the Larmor frequency of qubit j is constant throughout a single shot of a multi-cycle quantum error correction circuit, which typically takes a few microseconds. However, to obtain a statistical evaluation of the error correction performance, many shots should be taken, and the corresponding total data acquisition time window is sufficiently long that the noisy component ξ_j explores many random values, represented by a Gaussian distribution in my model.

A further assumption of my model is the statistical independence of the local random components of the Larmor frequencies, which is realistic if the Larmor frequency fluctuations are caused by local noise sources (e.g., gate electrodes, local flux bias lines, short-range charge fluctuators, etc.). I note that the numerical methods applied here are directly generalizable to variants of my noise model with more complex temporal and spatial correlations, which is in fact an interesting direction for future research.

The quasistatic phase damping model is relevant for semiconductor spin qubits as well, since spin qubit decoherence is often dominated by $1/f$ noise. [23, 176–178] Note that in such devices, $1/f$ noise is attributed either to externally imposed electromagnetic fluctuations, e.g., gate noise, magnet noise, fluctuating charge traps, or to hyperfine interaction, i.e., magnetic noise exerted on the electron spin by the nuclear spins covered by the electron.

In this chapter, I consider stabilizer codes as a way of countering quasistatic phase damping on idling qubits. As mentioned above, Hahn echo and other dynamical decoupling schemes provide established alternative solutions for the same problem. An important and timely research direction is to compare these solutions, and to explore their combinations [109–111] to maximize the coherence of logical qubits.

3.2 Example: 2-qubit repetition code

In this section, I study quasistatic phase damping using the example of a 2-qubit phase-flip code, as depicted in Fig. 3.1. I start with the analysis of a single cycle of syndrome measurement in Sec. 3.2.1, and show that in this case, quasistatic phase damping is equivalent to a simple uncorrelated phase-flip channel. In Sec. 3.2.2, explicit calculation of the density matrix reveals that this is not the case for two cycles of error detection. I quantify the difference between my model and the simple Pauli phase-flip model in Sec. 3.2.2. This simple example proves that quasistatic phase damping is a type of error that is distinct from phase-flip Pauli errors. This observation motivates the study of the stabilizer codes subject to quasistatic phase damping, which I do, focusing on the surface code, in Secs. 3.4 and 3.5.

In the two-qubit phase-flip repetition code, errors are detected by repeatedly measuring a single *parity-check* (or *stabilizer*) operator $\hat{S} = \hat{X}_A \hat{X}_B$. After each measurement, the state of the two qubits is altered by projectors $\hat{\Pi}_s$ that depend on the measurement outcome $s \in \{+1, -1\}$ (also called even or odd parity, respectively),

$$\hat{\Pi}_s = \frac{1}{2}(\hat{\mathbb{1}} + s\hat{S}). \quad (3.2)$$

Here, A and B label the two data qubits. The protocol aims to preserve the value of the logical \hat{Z} operators of the code, which reads,

$$\hat{Z}^L = \hat{Z}_A \hat{Z}_B. \quad (3.3)$$

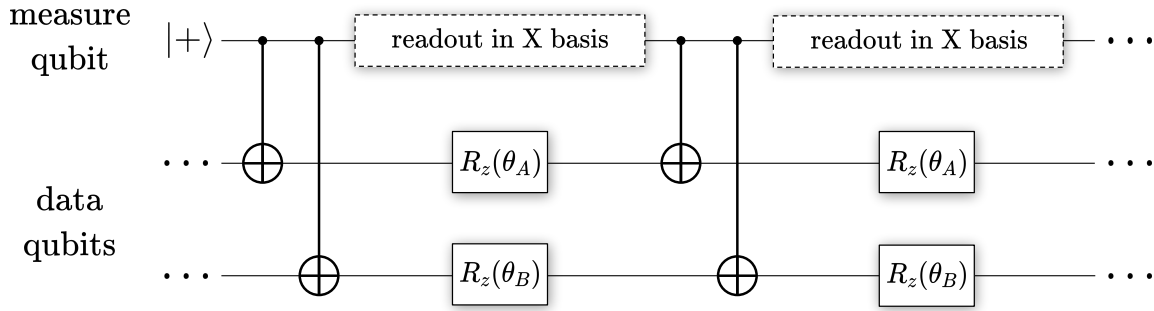


Figure 3.1: Schematic circuit representation of the 2-qubit phase-flip repetition code, data qubits A and B suffering quasistatic phase damping. The figure shows elements of two subsequent cycles in a multi-cycle error detection procedure. The gates labelled as $R_z(\theta_{A,B})$ represent coherent errors.

3.2.1 Single cycle of error detection

A single cycle of the two-qubit phase-flip repetition code, as an error detection protocol, is capable of detecting a single Pauli Z error. The list of all possible 2-qubit Pauli Z error strings is brief:

$$\hat{E} \in \{\hat{\mathbb{1}}, \hat{Z}_A, \hat{Z}_B, \hat{Z}_A \hat{Z}_B\}. \quad (3.4)$$

Independent phase-flip errors

I first consider independent phase-flip errors on the two physical qubits constituting the code. Throughout this chapter, I will use $P(\cdot)$ to denote the probability of a certain event. Assuming that the error probability on both qubits is p , and calculating the probability $P(\hat{E})$ of the occurrence of an error string \hat{E} for all possible 2-qubit errors, the Pauli error channel of the qubits reads,

$$\begin{aligned} \mathcal{E}_p(\hat{\rho}_0) &= \sum_{\hat{E}} P(\hat{E}) \hat{E} \hat{\rho}_0 \hat{E} = (1-p)^2 \hat{\rho}_0 + p(1-p) \hat{Z}_A \hat{\rho}_0 \hat{Z}_A \\ &\quad + (1-p)p \hat{Z}_B \hat{\rho}_0 \hat{Z}_B + p^2 \hat{Z}_A \hat{Z}_B \hat{\rho}_0 \hat{Z}_A \hat{Z}_B, \end{aligned} \quad (3.5)$$

for an arbitrary logical state of the two qubits $\hat{\rho}_0 = |\Psi_L\rangle\langle\Psi_L|$, where $|\Psi_L\rangle$ is an eigenstate of \hat{S} ,

$$\hat{S} |\Psi_L\rangle = |\Psi_L\rangle. \quad (3.6)$$

After the stabilizer measurement, for the trivial $s = +1$ outcome, the state of the two data qubits is projected to

$$\hat{\rho}_{1,p(+1)} = \hat{\Pi}_+ \mathcal{E}_p(\hat{\rho}_0) \hat{\Pi}_+ = (1-p)^2 \hat{\rho}_0 + p^2 \hat{Z}^L \hat{\rho}_0 \hat{Z}^L. \quad (3.7)$$

Quasistatic phase damping

I next consider independent coherent errors on the two qubits. The corresponding quantum channel reads,

$$\mathcal{E}_{\text{coh}}(\hat{\rho}_0) = \hat{U} \hat{\rho}_0 \hat{U}^\dagger, \quad \text{with} \quad \hat{U} = e^{i\theta_A \hat{Z}_A} e^{i\theta_B \hat{Z}_B}. \quad (3.8)$$

As mentioned in the previous section, the rotation angles are drawn from independent Gaussian distributions with zero mean, and identical standard deviations σ , i.e., with probability density function $f(\theta_A, \theta_B)$, which reads,

$$f(\theta_A, \theta_B) = f(\theta_A) f(\theta_B); \quad f(\theta) = \frac{1}{\sqrt{2\pi\sigma^2}} e^{-\frac{\theta^2}{2\sigma^2}}, \quad (3.9)$$

for $-\pi < \theta \leq \pi$. Since $f(\theta)$ is restricted to this interval, it is not normalized; however, I consider only small variances $\sigma \leq 0.5$, for which the normalization error is less than 10^{-9} . Note that in this single-cycle setting, the quasistatic phase damping model is the same as phase damping, as described in Sec. 8.3.6 of [9], independently on each qubit.

In this case, for the $s = +1$ measurement outcome, the density matrix of the two data qubits, averaged over the random angle distribution, reads

$$\hat{\rho}_{1,\text{coh}}(+1) = \int d\theta_A d\theta_B f(\theta_A, \theta_B) \hat{\Pi}_+ \mathcal{E}_{\text{coh}}(\hat{\rho}_0) \hat{\Pi}_+ = \langle \cos^2 \theta \rangle^2 \hat{\rho}_0 + \langle \sin^2 \theta \rangle^2 \hat{Z}^L \hat{\rho}_0 \hat{Z}^L, \quad (3.10)$$

where $\langle \cdot \rangle$ denotes averaging over the random angle distribution:

$$\langle g(\theta) \rangle = \int_{-\pi}^{\pi} d\theta g(\theta) f(\theta). \quad (3.11)$$

Average effect of coherent errors can be represented as a random Pauli channel

Comparing Eqs. (3.7) and (3.10) I find that for a single cycle of error detection, choosing

$$p = \langle \sin^2 \theta \rangle = \frac{1}{2} \left(1 - e^{-2\sigma^2} \right), \quad (3.12)$$

the two density matrices are identical,

$$\hat{\rho}_{1,p}(+1) = \hat{\rho}_{1,\text{coh}}(+1). \quad (3.13)$$

This is also true for the syndrome $s = -1$. Hence, I conclude that in the case of a single cycle of error detection, the effect of uncorrelated random Pauli phase-flip errors is equivalent to the effect of phase damping. This simple equivalence is broken in the multi-cycle case, as I show below.

3.2.2 Two cycles of error detection

I now consider two cycles of error detection. There are altogether 4 different measurement outcomes, *syndromes*, in the two cycles,

$$\mathbf{s} \in \mathcal{M}, \quad \text{where } \mathcal{M} = \{(+1, +1), (-1, +1), (+1, -1), (-1, -1)\}. \quad (3.14)$$

There are 16 different cycle-resolved error scenarios \mathbf{E} ; these error scenarios are the configurations of Z error strings occurred in the different cycles:

$$\mathbf{E} = (\hat{E}_1, \hat{E}_2), \quad (3.15)$$

with the two error strings \hat{E}_1 and \hat{E}_2 occurring in the 1st and 2nd cycles, respectively, are elements of the error set defined in Eq. (3.4). I denote the *merged* error operators as

$$\hat{E}(\mathbf{E}) = \hat{E}_1 \hat{E}_2. \quad (3.16)$$

The set of merged error operators is the same as the set of errors defined in Eq. (3.4). The list of the 16 cycle-resolved error scenarios and the corresponding merged error operators are given in the second and third columns of Table 3.1, respectively. Table 3.2 also lists the syndrome probabilities calculated from the coherent error amplitudes.

Independent phase-flip errors

For independent phase-flip errors, after two cycles of syndrome measurements, the density matrix can be written in a Pauli-diagonal form (i.e. in each term the operators on the left and the right of the density matrix are the same) as

$$\hat{\rho}_2(\mathbf{s}) = \sum_{\mathbf{E} \in \mathcal{D}_s} P(\mathbf{E}) \hat{E}(\mathbf{E}) \hat{\rho}_0 \hat{E}(\mathbf{E}), \quad (3.17)$$

where \mathcal{D}_s denotes the set of cycle-resolved error scenarios consistent with the syndrome \mathbf{s} , and $P(\mathbf{E})$ is the probability of occurrence of the cycle-resolved error scenario \mathbf{E} . For example, for the trivial syndrome $(+1, +1)$, there are 4 compatible scenarios:

$$\mathbf{E} \in \{(\hat{\mathbf{1}}, \hat{\mathbf{1}}), (\hat{Z}^L, \hat{\mathbf{1}}), (\hat{\mathbf{1}}, \hat{Z}^L), (\hat{Z}^L, \hat{Z}^L)\}, \quad (3.18)$$

corresponding to 2 different merged error strings only, $\hat{E}(\hat{\mathbf{1}}, \hat{\mathbf{1}}) = \hat{E}(\hat{Z}^L, \hat{Z}^L) = \hat{\mathbf{1}}$ and $\hat{E}(\hat{Z}^L, \hat{\mathbf{1}}) = \hat{E}(\hat{\mathbf{1}}, \hat{Z}^L) = \hat{Z}^L$. (All merged error operators along with the syndrome each of them implies are listed in the third and fourth columns of Table 3.1, respectively.) For this syndrome, Eq. (3.17) implies:

$$\hat{\rho}_2(+1, +1) = \left(P(\hat{\mathbf{1}}, \hat{\mathbf{1}}) + P(\hat{Z}^L, \hat{Z}^L) \right) \hat{\rho}_0 + \left(P(\hat{Z}^L, \hat{\mathbf{1}}) + P(\hat{\mathbf{1}}, \hat{Z}^L) \right) \hat{Z}^L \hat{\rho}_0 \hat{Z}^L. \quad (3.19)$$

I introduce the notation c_s and d_s for the coefficients of various operators in the post-measurement state,

$$\hat{\rho}_2(\mathbf{s}) = \begin{cases} c_s \hat{\rho}_0 + d_s \hat{Z}^L \hat{\rho}_0 \hat{Z}^L, & \text{for } s_2 = +1; \\ c_s \hat{Z}_A \hat{\rho}_0 \hat{Z}_A + d_s \hat{Z}_B \hat{\rho}_0 \hat{Z}_B, & \text{for } s_2 = -1. \end{cases} \quad (3.20)$$

The coefficients c_s, d_s are positive and fulfill

$$\sum_{\mathbf{s} \in \mathcal{M}} (c_s + d_s) = 1, \quad (3.21)$$

and thus can be interpreted as probabilities. From Eq. (3.17), I obtain

$$c_{++} = (1-p)^4 + p^4, \quad (3.22a)$$

$$d_{++} = c_{-+} = d_{-+} = 2p^2(1-p)^2, \quad (3.22b)$$

$$c_{+-} = d_{+-} = c_{--} = d_{--} = p(1-p)^3 + p^3(1-p), \quad (3.22c)$$

where I have compactified the notation, e.g., $c_{++} \equiv c_{(+1,+1)}$. In what follows, I will compare the result Eq. (3.22) with the analogous result for quasistatic phase damping, to show that the two error models are inequivalent.

Quasistatic phase damping

Next, I consider quasistatic phase damping with random rotation angles θ_A and θ_B for the two qubits. As discussed above in Sec. 3.1, the two angles are drawn from the same Gaussian distribution, and qubit A (B) is subject to rotation with angle θ_A (θ_B) before both measurement cycles, as illustrated in Fig. 3.1. Before performing the averaging for the error angles, the effect of the coherent errors cannot be written as a Pauli diagonal channel as in Eq. (3.17). However, the angle distribution is symmetric with respect to zero. Therefore, after averaging over the angle distribution according to the quasistatic phase damping model, I do obtain a Pauli diagonal

channel, which can be written in the form of Eq. (3.20), although with different \tilde{c}_s and \tilde{d}_s coefficients - I use $\tilde{\cdot}$ to specify the case of quasistatic phase damping:

$$\tilde{c}_{++} = \frac{1}{16} \left(e^{-16\sigma^2} + 2e^{-8\sigma^2} + 8e^{-4\sigma^2} + 5 \right), \quad (3.23a)$$

$$\tilde{d}_{++} = \tilde{d}_{-+} = \frac{1}{16} \left(1 - e^{-8\sigma^2} \right)^2, \quad (3.23b)$$

$$\tilde{c}_{-+} = \frac{1}{16} \left(e^{-16\sigma^2} + 2e^{-8\sigma^2} - 8e^{-4\sigma^2} + 5 \right), \quad (3.23c)$$

$$\tilde{c}_{+-} = \tilde{d}_{+-} = \tilde{c}_{--} = \tilde{d}_{--} = \frac{1}{16} \left(1 - e^{-16\sigma^2} \right). \quad (3.23d)$$

From this result, I conclude that in this two-cycle case, the effect of quasistatic phase damping cannot be described as random independent phase-flip errors with the same error rate p on both qubits. This is apparent by a comparison of Eqs. (3.22) and (3.23): for independent homogeneous phase-flip errors, there are only 3 different c_s, d_s coefficients, while for quasistatic phase damping, there are 4 different coefficients.

Best approximation of quasistatic phase damping with independent homogeneous phase-flip errors

As discussed just above, with two subsequent cycles of error detection in the two-qubit phase-flip code, the effect of quasistatic phase damping cannot be described as random independent phase-flip errors with the same error parameter p on both qubits. In this section, I try to find the best independent homogeneous phase-flip approximation - the *best Pauli approximation* - of the quasistatic phase damping channel.

I will quantify the quality of the approximation by the total variation distance. This distance is defined as

$$\delta(p, \sigma) = \max_s \left(\max \left\{ |c_s - \tilde{c}_s|, |d_s - \tilde{d}_s| \right\} \right), \quad (3.24)$$

where the right-hand side depends on the single parameter of the random Pauli channel, p , through the coefficients c_s and d_s , and on the single parameter of the quasistatic phase damping channel, the standard deviation of the coherent error distribution σ , through the coefficients \tilde{c}_s and \tilde{d}_s . The best Pauli approximation of a quasistatic phase damping channel with σ has the parameter p_{best} , such that

$$\delta(p_{\text{best}}(\sigma), \sigma) \leq \delta(p, \sigma) \quad \text{for all } 0 < p < 1. \quad (3.25)$$

I computed the best Pauli approximation numerically, and the corresponding total variation distance is shown in Fig. 3.2. For small p and σ , I find good agreement with the power series expansions,

$$c_{++} \approx 1 - 4p + 6p^2, \quad (3.26a)$$

$$d_{++} = c_{-+} = d_{-+} \approx 2p^2, \quad (3.26b)$$

$$c_{+-} = d_{+-} = c_{--} = d_{--} \approx p - 3p^2, \quad (3.26c)$$

$$\tilde{c}_{++} \approx 1 - 4\sigma^2 + 16\sigma^4, \quad (3.26d)$$

$$\tilde{d}_{++} = \tilde{d}_{-+} \approx 4\sigma^4, \quad (3.26e)$$

$$\tilde{c}_{-+} \approx 8\sigma^4, \quad (3.26f)$$

$$\tilde{c}_{+-} = \tilde{d}_{+-} = \tilde{c}_{--} = \tilde{d}_{--} \approx \sigma^2 - 8\sigma^4, \quad (3.26g)$$

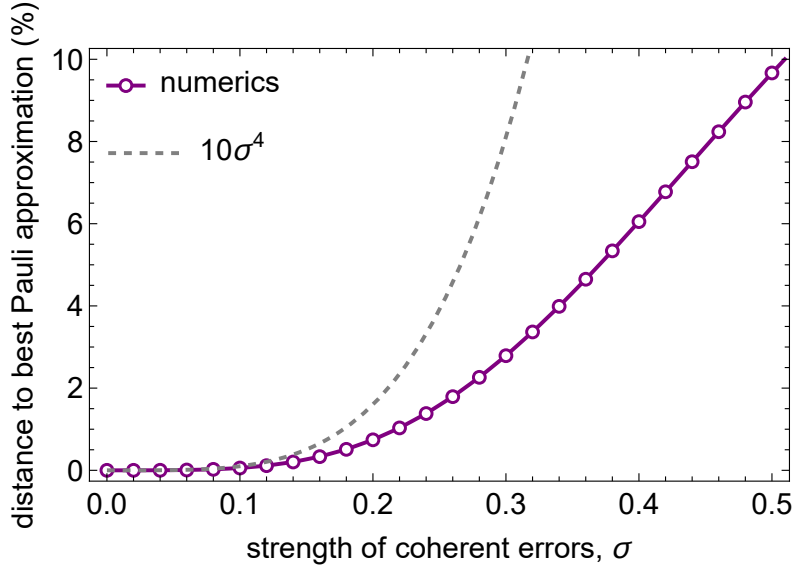


Figure 3.2: Distance between the two-cycle error channels of (1) quasistatic phase damping of strength σ , and (2) the independent and identical Pauli phase-flip channel that is closest to (1), for the two-qubit phase-flip repetition code.

which result in the best Pauli approximation,

$$\sigma \ll 1: \quad p_{\text{best}}(\sigma) \approx \sigma^2; \quad \delta(p_{\text{best}}, \sigma) = |c_{++}(p_{\text{best}}) - \tilde{c}_{++}| \approx 10\sigma^4. \quad (3.27)$$

For $\sigma \lesssim 0.3$, there is less than a few percent distance between quasistatic phase damping and the best Pauli approximation (see Fig. 3.2). Increasing σ , the distance to the best Pauli approximation is also increased; for $\sigma = 0.5$ it is around 10%.

3.3 Quasistatic phase damping in stabilizer codes

In this section, I generalize the results above, i.e., compare the quasistatic phase damping (quasistatic random coherent error) model with the uncorrelated phase-flip model, for Pauli stabilizer codes in general. In Sec. 3.3.1, I prove that the two models are equivalent in the case of a single cycle of error detection or error correction. In Sec. 3.3.2, I show that on the logical level, quasistatic phase damping is equivalent to a Pauli channel, however, this is not the one resulting from the simple uncorrelated phase-flip error model in general (see previous section as an example). Motivated by this difference of the error models, I will study the effect of quasistatic phase damping on the surface code in Secs. 3.4 and 3.5.

3.3.1 Single cycle of error detection and error correction

Now let me consider an arbitrary $[[n, k, d]]$ Pauli stabilizer code, encoding k logical qubits into n physical qubits with code distance d , whose stabilizers are tensor products of Pauli matrices and they commute with each other [97]. The stabilizer generators (independent parity checks) of the code are denoted by \hat{S}_f , with $f = 1, \dots, N$, with $N = n - k$. Upon measuring the stabilizer generators, one obtains the syndrome

$$s = (s_1, s_2, \dots, s_N) \in \{+1, -1\}^N, \quad (3.28)$$

No.	\mathbf{E}	$\hat{E}(\mathbf{E})$	\mathbf{s}	$P(\mathbf{E})$	$\tilde{P}(\mathbf{E})$
1	$(\hat{\mathbf{1}}, \hat{\mathbf{1}})$	$\hat{\mathbf{1}}$	$(+1, +1)$	$(1-p)^4$	$1 - 4p + 11p^2 - 26p^3 + 46p^4 - 60p^5 + 56p^6 - 32p^7 + 8p^8$
2	$(\hat{Z}_A \hat{Z}_B, \hat{Z}_A \hat{Z}_B)$	$\hat{\mathbf{1}}$	$(+1, +1)$	p^4	$p^2 - 6p^3 + 26p^4 - 52p^5 + 56p^6 - 32p^7 + 8p^8$
3	$(\hat{\mathbf{1}}, \hat{Z}_A \hat{Z}_B)$	$\hat{Z}_A \hat{Z}_B$	$(+1, +1)$	$(1-p)^2 p^2$	$2p^2 - 12p^3 + 34p^4 - 56p^5 + 56p^6 - 32p^7 + 8p^8$
4	$(\hat{Z}_A \hat{Z}_B, \hat{\mathbf{1}})$	$\hat{Z}_A \hat{Z}_B$	$(+1, +1)$	$(1-p)^2 p^2$	$2p^2 - 12p^3 + 34p^4 - 56p^5 + 56p^6 - 32p^7 + 8p^8$
5	(\hat{Z}_A, \hat{Z}_A)	$\hat{\mathbf{1}}$	$(-1, +1)$	$(1-p)^2 p^2$	$4p^2 - 16p^3 + 36p^4 - 56p^5 + 56p^6 - 32p^7 + 8p^8$
6	(\hat{Z}_B, \hat{Z}_B)	$\hat{\mathbf{1}}$	$(-1, +1)$	$(1-p)^2 p^2$	$4p^2 - 16p^3 + 36p^4 - 56p^5 + 56p^6 - 32p^7 + 8p^8$
7	(\hat{Z}_A, \hat{Z}_B)	$\hat{Z}_A \hat{Z}_B$	$(-1, +1)$	$(1-p)^2 p^2$	$2p^2 - 12p^3 + 34p^4 - 56p^5 + 56p^6 - 32p^7 + 8p^8$
8	(\hat{Z}_B, \hat{Z}_A)	$\hat{Z}_A \hat{Z}_B$	$(-1, +1)$	$(1-p)^2 p^2$	$2p^2 - 12p^3 + 34p^4 - 56p^5 + 56p^6 - 32p^7 + 8p^8$
9	$(\hat{\mathbf{1}}, \hat{Z}_A)$	\hat{Z}_A	$(+1, -1)$	$(1-p)^3 p$	$p - 6p^2 + 19p^3 - 40p^4 + 58p^5 - 56p^6 + 32p^7 - 8p^8$
10	$(\hat{Z}_A \hat{Z}_B, \hat{Z}_B)$	\hat{Z}_A	$(+1, -1)$	$(1-p)p^3$	$-p^2 + 9p^3 - 30p^4 + 54p^5 - 56p^6 + 32p^7 - 8p^8$
11	$(\hat{\mathbf{1}}, \hat{Z}_B)$	\hat{Z}_B	$(+1, -1)$	$(1-p)^3 p$	$p - 6p^2 + 19p^3 - 40p^4 + 58p^5 - 56p^6 + 32p^7 - 8p^8$
12	$(\hat{Z}_A \hat{Z}_B, \hat{Z}_A)$	\hat{Z}_B	$(+1, -1)$	$(1-p)p^3$	$-p^2 + 9p^3 - 30p^4 + 54p^5 - 56p^6 + 32p^7 - 8p^8$
13	$(\hat{Z}_A, \hat{\mathbf{1}})$	\hat{Z}_A	$(-1, -1)$	$(1-p)^3 p$	$p - 6p^2 + 19p^3 - 40p^4 + 58p^5 - 56p^6 + 32p^7 - 8p^8$
14	$(\hat{Z}_B, \hat{Z}_A \hat{Z}_B)$	\hat{Z}_A	$(-1, -1)$	$(1-p)p^3$	$-p^2 + 9p^3 - 30p^4 + 54p^5 - 56p^6 + 32p^7 - 8p^8$
15	$(\hat{Z}_A, \hat{Z}_A \hat{Z}_B)$	\hat{Z}_B	$(-1, -1)$	$(1-p)p^3$	$-p^2 + 9p^3 - 30p^4 + 54p^5 - 56p^6 + 32p^7 - 8p^8$
16	$(\hat{Z}_B, \hat{\mathbf{1}})$	\hat{Z}_B	$(-1, -1)$	$(1-p)^3 p$	$p - 6p^2 + 19p^3 - 40p^4 + 58p^5 - 56p^6 + 32p^7 - 8p^8$

Table 3.1: Summary of cycle-resolved error scenarios \mathbf{E} , merged error operators $\hat{E}(\mathbf{E})$, syndromes \mathbf{s} , independent Pauli phase-flip probabilities $P(\mathbf{E})$, and coherent error amplitudes $\tilde{P}(\mathbf{E})$ (written as a function of $p = \langle \sin^2 \theta \rangle$) calculated from Eq. (3.45), for the 2-qubit repetition code, for two cycles of error detection. Note that the coherent error amplitudes $\tilde{P}(\mathbf{E})$ can be negative as well.

\mathbf{s}	$\mathcal{D}_{\mathbf{s}}$	$\sum_{\mathbf{E} \in \mathcal{D}_{\mathbf{s}}} \tilde{P}(\mathbf{E})$
$(+1, +1)$	$(\hat{\mathbf{1}}, \hat{\mathbf{1}}), (\hat{Z}_A \hat{Z}_B, \hat{Z}_A \hat{Z}_B),$ $(\hat{\mathbf{1}}, \hat{Z}_A \hat{Z}_B), (\hat{Z}_A \hat{Z}_B, \hat{\mathbf{1}})$	$(1 - 2p + 2p^2)^2 (1 + 8p^2 - 16p^3 + 8p^4)$
$(-1, +1)$	$(\hat{Z}_A, \hat{Z}_A), (\hat{Z}_B, \hat{Z}_B),$ $(\hat{Z}_A, \hat{Z}_B), (\hat{Z}_B, \hat{Z}_A)$	$4(1-p)^2 p^2 (3 - 8p + 16p^2 - 16p^3 + 8p^4)$
$(+1, -1)$	$(\hat{\mathbf{1}}, \hat{Z}_A), (\hat{Z}_A \hat{Z}_B, \hat{Z}_B),$ $(\hat{\mathbf{1}}, \hat{Z}_B), (\hat{Z}_A \hat{Z}_B, \hat{Z}_A)$	$2p(1 - 7p + 28p^2 - 70p^3 + 112p^4 - 112p^5 + 64p^6 - 16p^7)$
$(-1, -1)$	$(\hat{Z}_A, \hat{\mathbf{1}}), (\hat{Z}_B, \hat{Z}_A \hat{Z}_B),$ $(\hat{Z}_A, \hat{Z}_A \hat{Z}_B), (\hat{Z}_B, \hat{\mathbf{1}})$	$2p(1 - 7p + 28p^2 - 70p^3 + 112p^4 - 112p^5 + 64p^6 - 16p^7)$

Table 3.2: List of all possible syndromes \mathbf{s} for the 2-qubit repetition code, together with the corresponding set of consistent cycle-resolved error scenarios $\mathcal{D}_{\mathbf{s}}$, and the syndrome probabilities calculated as the sum of coherent error amplitudes $\tilde{P}(\mathbf{E})$ (written as a function of $p = \langle \sin^2 \theta \rangle$). Unlike the individual $\tilde{P}(\mathbf{E})$ coherent error amplitudes, the syndrome detection probabilities listed in the last column are always positive.

and the quantum state of the qubits is projected to the code space with the projector

$$\hat{\Pi}_s = \prod_{f=1}^N \frac{1}{2} \left(1 + s_f \hat{S}_f \right). \quad (3.29)$$

I aim to investigate the form of the quasistatic coherent error channel combined with error detection. To this end, I have to perform an averaging over the random angle distribution for the post-measurement state. I will denote this average by

$$\langle \dots \rangle_{\boldsymbol{\theta}} \equiv \int d\boldsymbol{\theta} f(\boldsymbol{\theta}) \dots, \quad (3.30)$$

where $f(\boldsymbol{\theta}) = f(\theta_1)f(\theta_2)\cdots f(\theta_n)$ is the probability density function of the independent random rotation angles. The following derivation holds not only for the Gaussian angle distribution of Eq. (3.9), but also for any (discrete or continuous) probability distribution that is symmetric and has zero mean value, i.e.,

$$f(\theta) = f(-\theta), \quad \text{with } -\pi < \theta \leq \pi. \quad (3.31)$$

Note that in this case, the average of any odd function of θ_j will vanish.

For a single cycle of error detection, the effect of quasistatic phase damping is expressed as:

$$\hat{\rho}_1(s) = \langle \hat{\Pi}_s \hat{U} \hat{\rho}_0 \hat{U}^\dagger \hat{\Pi}_s \rangle_{\boldsymbol{\theta}} = \sum_{\hat{E}, \hat{E}'} \left\langle A_{\boldsymbol{\theta}}(\hat{E}) A_{\boldsymbol{\theta}}^*(\hat{E}') \right\rangle_{\boldsymbol{\theta}} \hat{\Pi}_s \hat{E} \hat{\rho}_0 \hat{E}' \hat{\Pi}_s. \quad (3.32)$$

Here, $\hat{\rho}_0 = |\Psi_L\rangle\langle\Psi_L|$ is the density matrix of an arbitrary initial logical state, i.e., with $|\Psi_L\rangle$ being a common eigenstate of all stabilizer operators with +1 eigenvalue. Furthermore, the 2^n error strings corresponding to \hat{Z} phase-flip operations on either of the qubits are denoted as \hat{E} , and I have rewritten the product of coherent single qubit rotations as

$$\hat{U} = \sum_{\hat{E}} A_{\boldsymbol{\theta}}(\hat{E}) \hat{E}, \quad (3.33)$$

by introducing the amplitudes

$$A_{\boldsymbol{\theta}}(\hat{E}) = \prod_{j=1}^n (\cos \theta_j)^{1-n_{\hat{E}}(j)} (i \sin \theta_j)^{n_{\hat{E}}(j)}. \quad (3.34)$$

Here $n_{\hat{E}}(j) = 0$ or 1 denotes the number of Pauli Z operators acting on qubit j in error string \hat{E} . For example, in case of $n = 5$, the double sum in Eq. (3.32) runs over 5-qubit Pauli Z error strings,

$$\hat{E} = \hat{\mathbb{1}}\hat{\mathbb{1}}\hat{\mathbb{1}}\hat{\mathbb{1}}\hat{\mathbb{1}}, \dots, \hat{\mathbb{1}}\hat{\mathbb{1}}\hat{\mathbb{1}}\hat{\mathbb{1}}\hat{Z}, \dots, \hat{Z}\hat{\mathbb{1}}\hat{\mathbb{1}}\hat{Z}\hat{\mathbb{1}}, \dots, \hat{Z}\hat{Z}\hat{Z}\hat{Z}\hat{Z}, \quad (3.35)$$

corresponding to

$$n_{\hat{E}} = 00000, 00001, \dots, 10010, \dots, 11111, \quad (3.36)$$

respectively.

Now, I show that Eq. (3.32) can be simplified. First, averaging over the random angles in Eq. (3.32) yields:

$$\left\langle A_{\boldsymbol{\theta}}(\hat{E}) A_{\boldsymbol{\theta}}^*(\hat{E}') \right\rangle_{\boldsymbol{\theta}} = \delta_{\hat{E}, \hat{E}'} \left\langle |A_{\boldsymbol{\theta}}(\hat{E})|^2 \right\rangle_{\boldsymbol{\theta}} \equiv P(\hat{E}). \quad (3.37)$$

Second, I note that since the stabilizers are products of Pauli operators, they either commute or anti-commute with the error strings. Therefore, applying the error string \hat{E} and then measuring the syndrome s compatible with that has the same effect as first projecting the collective quantum

state of the qubits to the trivial syndrome (all parity checks are +1) and then applying the error string; i.e., it holds that

$$\hat{\Pi}_s \hat{E} = \hat{E} \hat{\Pi}_0, \quad \text{if } \hat{E} \in \mathcal{D}_s, \quad (3.38)$$

where \mathcal{D}_s is the set of error strings consistent with the syndrome s

Hence, by exploiting Eqs. (3.37) and (3.38) in Eq. (3.32), I obtain a simplified formula for the error channel,

$$\hat{\rho}_1(s) = \sum_{\hat{E} \in \mathcal{D}_s} P(\hat{E}) \hat{E} \hat{\rho}_0 \hat{E}, \quad (3.39)$$

where the $P(\hat{E})$ probabilities follow from Eq. (3.34) as

$$P(\hat{E}) = \prod_{j=1}^n \langle \cos^2 \theta_j \rangle_{\theta}^{1-n_{\hat{E}}(j)} \langle \sin^2 \theta_j \rangle_{\theta}^{n_{\hat{E}}(j)}. \quad (3.40)$$

Since the \hat{E} error strings are products of Pauli Z and identity matrices, the result, Eq. (3.39), is a simple phase flip channel with equal and independent error probabilities on each qubit, $p = \langle \sin^2 \theta_j \rangle_{\theta}$, for each syndrome s . Consequently, for a single cycle of experiment performed with any Pauli stabilizer code, quasistatic phase damping is equivalent to uncorrelated phase-flip errors on average. Indeed that is an unsurprising result, since for a single physical qubit, phase damping is the same as the phase flip channel [9].

A result analogous to Eq. (3.39) holds for a single cycle of error *correction* as well since the correction operation \hat{C}_s depends only on the syndrome s . Hence, the state of the code after error correction has the following form:

$$\hat{C}_s \hat{\rho}_1(s) \hat{C}_s = \sum_{\hat{E} \in \mathcal{D}_s} P(\hat{E}) \hat{C}_s \hat{E} \hat{\rho}_0 \hat{E} \hat{C}_s. \quad (3.41)$$

3.3.2 Multiple cycles

I next consider multiple, t cycles of error detection: I apply the independent coherent rotations of the qubits with angles $\theta_1, \theta_2, \dots, \theta_n$, and the measurements repeatedly. I show that in this case, the average effect of quasistatic phase damping can be represented only with a more complicated Pauli channel. It is important to note that the angles θ_j do not change from cycle to cycle: if they did, this error model would – after averaging over the random angles – be equivalent to independent phase-flip errors.

Altogether, there are 2^{tn} cycle-resolved error scenarios \mathbf{E} , corresponding to different combinations of \hat{Z} phase-flip operations on either of the qubits during either of the cycles, and 2^n different merged Pauli-Z error strings $\hat{E}(\mathbf{E})$,

$$\mathbf{E} = (\hat{E}_1, \hat{E}_2, \dots, \hat{E}_t); \quad \hat{E}(\mathbf{E}) = \prod_{r=1}^t \hat{E}_r. \quad (3.42)$$

With this notation, I express the syndrome-dependent state of the code after t error detection cycles as follows:

$$\begin{aligned} \hat{\rho}_t(s) &= \left\langle \hat{Q}(\boldsymbol{\theta}) \hat{\rho}_0 \hat{Q}(\boldsymbol{\theta})^\dagger \right\rangle_{\boldsymbol{\theta}} = \sum_{\mathbf{E} \in \mathcal{D}_s} \sum_{\mathbf{E}' \in \mathcal{D}_s} \left\langle A_{\boldsymbol{\theta}}(\mathbf{E}) A_{\boldsymbol{\theta}}^*(\mathbf{E}') \right\rangle_{\boldsymbol{\theta}} \hat{E}(\mathbf{E}) \hat{\rho}_0 \hat{E}(\mathbf{E}') \\ &= \sum_{\mathbf{E} \in \mathcal{D}_s} \tilde{P}(\mathbf{E}) \hat{E}(\mathbf{E}) \hat{\rho}_0 \hat{E}(\mathbf{E}), \end{aligned} \quad (3.43)$$

where $\mathbf{s} = (s_1, s_2, \dots, s_t)$ is a multi-cycle syndrome (note that now the syndrome indices are labeling the quantum error correction cycles, and each $s_r \in \{+1, -1\}^N$), and I introduced the notations $\hat{Q}(\boldsymbol{\theta}) = \hat{\Pi}_{s_t} \hat{U} \hat{\Pi}_{s_{t-1}} \hat{U} \dots \hat{\Pi}_{s_1} \hat{U}$, and

$$A_{\boldsymbol{\theta}}(\mathbf{E}) = \prod_{r=1}^t A_{\boldsymbol{\theta}}(\hat{E}_r). \quad (3.44)$$

The density matrix in Eq. (3.43) is again Pauli-diagonal, but the newly defined quantities

$$\tilde{P}(\mathbf{E} \in \mathcal{D}_s) = \sum_{\mathbf{E}' \in \mathcal{D}_s} \left\langle A_{\boldsymbol{\theta}}(\mathbf{E}) A_{\boldsymbol{\theta}}^*(\mathbf{E}') \right\rangle_{\boldsymbol{\theta}} = \sum_{\substack{\mathbf{E}' \in \mathcal{D}_s \\ \hat{E}(\mathbf{E}) = \hat{E}(\mathbf{E}')}} \left\langle A_{\boldsymbol{\theta}}(\mathbf{E}) A_{\boldsymbol{\theta}}^*(\mathbf{E}') \right\rangle_{\boldsymbol{\theta}}, \quad (3.45)$$

obtained by regrouping the terms in the double sum, are not probabilities: they add up to 1,

$$\sum_{\mathbf{E}} \tilde{P}(\mathbf{E}) = 1, \quad (3.46)$$

but they can be negative as well (see Table 3.1), depending on which power of the imaginary unit appears in the corresponding terms. Real values are guaranteed by the fact that the terms containing odd powers of $(i \sin \theta_j)$ will vanish after averaging. In Eq. (3.45), I only get a non-zero contribution when $\hat{E}(\mathbf{E}) = \hat{E}(\mathbf{E}')$.

Upon performing the last sum in Eq. (3.43), the following result is obtained:

$$\hat{\rho}_t(\mathbf{s}) = \sum_{\boldsymbol{\alpha}} \tilde{\mathcal{P}}_{\boldsymbol{\alpha}}(\mathbf{s}) \hat{Z}_{\boldsymbol{\alpha}} \hat{E}_s \hat{\rho}_0 \hat{E}_s \hat{Z}_{\boldsymbol{\alpha}}, \quad (3.47)$$

where

$$\hat{Z}_{\boldsymbol{\alpha}} = (\hat{Z}_1^L)^{\alpha_1} (\hat{Z}_2^L)^{\alpha_2} \dots (\hat{Z}_k^L)^{\alpha_k}; \quad (3.48)$$

$$\tilde{\mathcal{P}}_{\boldsymbol{\alpha}}(\mathbf{s}) = \sum_{\substack{\mathbf{E} \in \mathcal{D}_s \\ \hat{E}(\mathbf{E}) = \hat{Z}_{\boldsymbol{\alpha}} \hat{E}_s}} \tilde{P}(\mathbf{E}). \quad (3.49)$$

Furthermore, I defined $\boldsymbol{\alpha} = (\alpha_1, \dots, \alpha_k) \in \{0, 1\}^k$, the operator \hat{Z}_j^L is defined as the logical Z operator acting on the j -th logical qubit, and \hat{E}_s is an arbitrary merged error string consistent with the syndrome \mathbf{s} . The $\tilde{\mathcal{P}}_{\boldsymbol{\alpha}}(\mathbf{s})$ quantities are syndrome-dependent probabilities, meaning that they are positive, since substituting Eq. (3.45) into Eq. (3.49) yields

$$\begin{aligned} \tilde{\mathcal{P}}_{\boldsymbol{\alpha}}(\mathbf{s}) &= \sum_{\substack{\mathbf{E}, \mathbf{E}' \in \mathcal{D}_s \\ \hat{E}(\mathbf{E}) = \hat{E}(\mathbf{E}') \\ \hat{E}(\mathbf{E}) = \hat{Z}_{\boldsymbol{\alpha}} \hat{E}_s}} \left\langle A_{\boldsymbol{\theta}}(\mathbf{E}) A_{\boldsymbol{\theta}}^*(\mathbf{E}') \right\rangle_{\boldsymbol{\theta}} = \left\langle \left(\sum_{\substack{\mathbf{E} \in \mathcal{D}_s \\ \hat{E}(\mathbf{E}) = \hat{Z}_{\boldsymbol{\alpha}} \hat{E}_s}} A_{\boldsymbol{\theta}}(\mathbf{E}) \right) \left(\sum_{\substack{\mathbf{E}' \in \mathcal{D}_s \\ \hat{E}(\mathbf{E}') = \hat{Z}_{\boldsymbol{\alpha}} \hat{E}_s}} A_{\boldsymbol{\theta}}^*(\mathbf{E}') \right) \right\rangle_{\boldsymbol{\theta}} \\ &= \left\langle \left| \sum_{\substack{\mathbf{E} \in \mathcal{D}_s \\ \hat{E}(\mathbf{E}) = \hat{Z}_{\boldsymbol{\alpha}} \hat{E}_s}} A_{\boldsymbol{\theta}}(\mathbf{E}) \right|^2 \right\rangle_{\boldsymbol{\theta}} > 0, \end{aligned} \quad (3.50)$$

and they satisfy

$$\sum_{\boldsymbol{\alpha}, \mathbf{s}} \tilde{\mathcal{P}}_{\boldsymbol{\alpha}}(\mathbf{s}) = 1. \quad (3.51)$$

These probabilities are the generalization of the single-logical-qubit coefficients \tilde{c}_s and \tilde{d}_s of Eq. (3.23), e.g. $\tilde{c}_{++} = \tilde{\mathcal{P}}_0(++), \tilde{d}_{++} = \tilde{\mathcal{P}}_1(++).$ As discussed in Sec. 3.2.2, these probabilities cannot be derived from independent single-qubit Z error probabilities.

From Eq. (3.43) it is not clear whether it is a well-defined Pauli channel on the physical level, because the $\tilde{P}(\mathbf{E})$ weights can be negative, thus these are not probabilities. However, one can rephrase Eq. (3.43) by using a new set of amplitudes $\tilde{P}'(\mathbf{E})$ that are positive, and hence define a proper Pauli channel on the physical level as well. This new set of amplitudes can be defined by redistributing the amplitudes within each class of cycle-resolved error scenarios (\mathbf{E}), where the classes are indexed by \mathbf{s} and α , and are defined via $\mathbf{E} \in \mathcal{D}_{\mathbf{s}}$, $\hat{E}(\mathbf{E}) = \hat{Z}_{\alpha} \hat{E}_{\mathbf{s}}$. In words, two cycle-resolved error scenarios belong to the same class, if they imply the same syndrome and the same merged error string. By performing such a redistribution $\tilde{P} \rightarrow \tilde{P}'$ of amplitudes, the error channel in Eq. (3.47) does not change: the $\tilde{\mathcal{P}}_{\alpha}(\mathbf{s})$ probabilities remain the same. Note that this redistribution is not unique; one way to do it is to choose one representative cycle-resolved error scenario $\mathbf{E}'_{\mathbf{s},\alpha}$ from each error class, and define new amplitudes, which are in fact non-negative, as:

$$\tilde{P}'(\mathbf{E}'_{\mathbf{s},\alpha}) = \tilde{\mathcal{P}}_{\alpha}(\mathbf{s}), \quad (3.52)$$

and $\tilde{P}'(\mathbf{E}) = 0$ for all \mathbf{E} that is not in the set of $\mathbf{E}'_{\mathbf{s},\alpha}$ representatives. This shows that my error model can be described as a Pauli model on the physical level. However, this Pauli model is highly correlated. It is an open question whether it is possible to construct an error model with local (in both space and time) correlations by redefining these weights differently. This question is beyond the scope of my thesis.

I conclude that for multiple cycles, the quasistatic phase damping channel is equivalent to an incoherent Pauli channel as written in Eq. (3.43), as well as an incoherent Pauli channel on the logical level, as written in Eq. (3.47). However, the Pauli channel in Eq. (3.43) does not describe, in general, independent homogeneous single-qubit phase flips, as I illustrated by the counterexample in Sec. 3.2.2.

3.4 Surface code error threshold

So far, it has been shown that for stabilizer codes applied for multi-cycle error correction, the effect of quasistatic phase damping is distinct from that of phase-flip Pauli errors. This motivates studies of noise resilience in this new setting. In the following section, I do this by focusing on the surface code. In particular, I numerically demonstrate that the surface code in the presence of quasistatic phase damping and readout errors exhibits a threshold behavior. To this end, I apply the Fermionic Linear Optics (FLO) simulation technique [115–117]. In Sec. 3.4.1, I briefly summarize the basics of the surface code and the effect of coherent errors. In Sec. 3.4.2, I discuss error correction in the presence of readout errors. In Sec. 3.4.3, I briefly describe the FLO simulation technique. Finally, I present my numerical results in Sec. 3.4.4, showing that the threshold for quasistatic phase damping is, up to numerical precision, the same as the threshold for Pauli phase flips, whereas the logical error rate at threshold is smaller in the former case (7%) than in the latter case (8.5%).

3.4.1 Coherent errors lead to coherent error on the logical qubit

The surface code encodes a logical qubit in the common +1 eigenspace of the X-type and Z-type parity check operators (stabilizers), as shown in Fig. 1.8(a). Since I consider coherent Z errors, only the X-type parity checks, $\hat{S}_f = \prod_{j \in \partial f} \hat{X}_j$, can return a -1 value. As a result of a single cycle of measurements, which is assumed to be free of readout error for now, a syndrome s is obtained. If this syndrome s is non-trivial, then a non-identity correction operation \hat{C}_s is applied as an attempt to bring the state back into the code space. In this case, \hat{C}_s involves a collection of Pauli Z phase flips. The specific correction operation for a given syndrome is the solution of the decoding problem, which I discuss briefly in Sec. 3.4.2.

Irrespective of the decoding algorithm, coherent errors on the physical qubits, after error correction, lead to a coherent error of the same type on the logical level [117]. Starting from an arbitrary logical state $|\Psi_L\rangle$, the quantum state of $n = d^2$ data qubits after measuring syndrome s , and applying the corresponding correction, can be written as [115]

$$|\Phi_s\rangle = \frac{1}{\sqrt{P(s)}} \hat{C}_s \hat{\Pi}_s \hat{U} |\Psi_L\rangle = e^{i\theta_L \hat{Z}^L} |\Psi_L\rangle, \quad (3.53)$$

where $P(s) = \langle \Psi_L | U^\dagger \hat{\Pi}_s U | \Psi_L \rangle$ is the probability of syndrome s , and the logical rotation angle θ_L depends on the syndrome, the decoder, and the physical rotation angles, $\theta_L = \theta_L(s, \boldsymbol{\theta})$, but *not* on the initial state $|\Psi_L\rangle$.

For a given syndrome s , I quantify the logical error by the maximum infidelity of the final state $|\Phi_s\rangle$ with the initial state $|\Psi_L\rangle$, maximized over all initial states. Logical rotations around the z axis are the most harmful for the eigenstates of the \hat{X}^L operator, thus I obtain the logical error rate as

$$p_L(s, \boldsymbol{\theta}) \equiv \max_{|\Psi_L\rangle} (1 - |\langle \Psi_L | \Phi_s \rangle|^2) = \sin^2 \theta_L(s, \boldsymbol{\theta}), \quad (3.54)$$

with this maximum attained for $|\Psi_L\rangle = |+_L\rangle$, the common eigenstate of \hat{X}^L as well as of all the stabilizer generators \hat{S}_f with eigenvalue $+1$.

To characterize the strength of the quasistatic phase damping errors, I will use either the standard deviation σ of the single-qubit random coherent rotations, or the *physical error rate* p which is defined as for the repetition code, Eq. (3.12). This definition is motivated by the fact that for single-cycle error detection and error correction, it provides an exact correspondence with the uncorrelated phase-flip channel.

3.4.2 Error correction with readout errors

I use a phenomenological noise model for readout errors, where the syndrome measurements are described by the corresponding (ideal) projections of the logical state, but the measurement outcomes are unreliably recorded, with readout error probability q ,

$$P(-1 \rightarrow +1) = P(+1 \rightarrow -1) = q \quad (3.55)$$

and $P(-1 \rightarrow -1) = P(+1 \rightarrow +1) = 1 - q$. To be able to detect and correct the readout errors as well, I consider d consecutive cycles of syndrome measurements. As a result, I get the noisy multi-cycle syndrome

$$\mathbf{s} = (s_1, s_2, \dots, s_d) \rightarrow \mathbf{s}' = (s'_1, s'_2, \dots, s'_d). \quad (3.56)$$

The state of the code after measuring the noisy multi-cycle syndrome \mathbf{s}' , decoding it, and applying the corresponding correction operator, yields [117]:

$$|\Phi_{\mathbf{s}, \mathbf{s}'}\rangle = \frac{1}{\sqrt{P(\mathbf{s})}} \hat{C}_{\mathbf{s}'} \hat{\Pi}_{s'_d} \hat{U} \dots \hat{\Pi}_{s'_1} \hat{U} |\Psi_L\rangle = \hat{C}_{\mathbf{s}'} \hat{C}_{s'_d} e^{i\theta^* \hat{Z}^L} |\Psi_L\rangle = e^{i\theta_L \hat{Z}^L} |\Psi_L\rangle, \quad (3.57)$$

where $P(\mathbf{s})$ is the probability of measuring the multi-cycle syndrome \mathbf{s} , and the logical rotation angle $\theta^* = \theta^*(\mathbf{s}, \boldsymbol{\theta})$ depends on the perfect multi-cycle syndrome only, however, θ_L now depends on the noisy multi-cycle syndrome as well, $\theta_L = \theta_L(\mathbf{s}, \mathbf{s}', \boldsymbol{\theta})$, through the correction $\hat{C}_{\mathbf{s}'}$.

To correct errors based on the noisy multi-cycle syndrome that is contaminated by readout error, I use the 3-dimensional version of the minimum weight perfect matching (MWPM) decoder [179], as implemented in PyMatching [180]. This decoder is less accurate, but much more efficient than maximum likelihood decoding which is an NP-complete problem [181], meaning that asymptotically the runtime grows exponentially with the code size (however for independent bit-flip and phase-flip errors there is an efficient algorithm [182]). PyMatching has expected

runtime of $\mathcal{O}(N^{1.32})$ [180], where N is the number of nodes in the decoding graph, described below.

The decoder sees the measurement outcomes as a 3-dimensional grid that has $(d^2 - 1)/2 \times (d^2 - 1)/2$ ‘space’ coordinates, characterizing the positions of the measured X stabilizers, and d ‘time’ coordinates, numbering the measurement cycles. Vertices, where the measured parity check differs from the value measured in the previous cycle, are marked, and the decoder needs to identify the set of edges with the smallest weight that connects the marked vertices to the left/right boundaries or pairs them up. An example decoding graph is depicted on Fig. 3.3. The correction operation is inferred from the resulting set of edges. ‘Spacelike’ and ‘timelike’ edges on the grid correspond to readout errors and physical errors. These carry different weights (w_s and w_t), since the rate p of coherent errors can differ from the rate q of readout errors. The weights are defined as [99]

$$w_s = \log\left(\frac{1-p}{p}\right) \quad \text{and} \quad w_t = \log\left(\frac{1-q}{q}\right), \quad (3.58)$$

such that a higher error probability corresponds to a lower weight, favored by the MWPM algorithm. To ensure that the correction operator brings the state back to the code space, the last measurement cycle is assumed to be free of any readout errors, $s'_d = s_d$, and the decoder is aware of this assumption. This is not a realistic assumption, but it has no significant impact on the results. Using more realistic (circuit-level) simulations, in a quantum memory setting, after the last cycle of syndrome extraction all data qubits are measured as well. Reconstructing the parity check from the outcomes of this final set of measurements and comparing them with the last cycle syndrome s'_d makes it possible to correct measurement errors occurring in the cycle.

Assuming perfect measurements in the last cycle, $s'_d = s_d$, readout errors lead to identity, or an extra logical \hat{Z}^L error, which is equivalent to a $\pi/2$ rotation, and is determined by

$$\theta_L(\mathbf{s}, \mathbf{s}', \boldsymbol{\theta}) = \begin{cases} \theta^*(\mathbf{s}, \boldsymbol{\theta}), & \text{if } \hat{C}_{\mathbf{s}'} \hat{C}_{s_d} |\Psi_L\rangle = |\Psi_L\rangle \\ \theta^*(\mathbf{s}, \boldsymbol{\theta}) + \frac{\pi}{2}, & \text{if } \hat{C}_{\mathbf{s}'} \hat{C}_{s_d} |\Psi_L\rangle = \hat{Z}^L |\Psi_L\rangle. \end{cases} \quad (3.59)$$

In this case, Eq. (3.54) is modified to

$$p_L(\mathbf{s}, \mathbf{s}', \boldsymbol{\theta}) = \sin^2 \theta_L(\mathbf{s}, \mathbf{s}', \boldsymbol{\theta}), \quad (3.60)$$

From this expression, I obtain the average logical error rate by averaging over all noisy syndromes and the $\boldsymbol{\theta}$ angle distribution as well,

$$p_L(\sigma) = \sum_{\mathbf{s}, \mathbf{s}'} P(\mathbf{s}) P(\mathbf{s} \rightarrow \mathbf{s}') \left\langle \sin^2 \theta_L(\mathbf{s}, \mathbf{s}', \boldsymbol{\theta}) \right\rangle_{\boldsymbol{\theta}}, \quad (3.61)$$

where $P(\mathbf{s} \rightarrow \mathbf{s}')$ is the probability that the noisy syndrome \mathbf{s}' was recorded instead of the ideal multi-cycle syndrome \mathbf{s} .

3.4.3 Fermionic Linear Optics simulation

Standard Pauli errors in quantum error correction can be efficiently simulated with Clifford simulators [12, 97]. Unfortunately, to simulate quasistatic coherent errors, I could not use this tool. To explore the effect of coherent errors in the surface code, several numerical methods have been considered. Brute-force simulations of small systems [183–185], tensor-network simulations for slightly larger systems [186], and Fermionic Linear Optics (FLO) methods [115–117] have emerged as possible options.

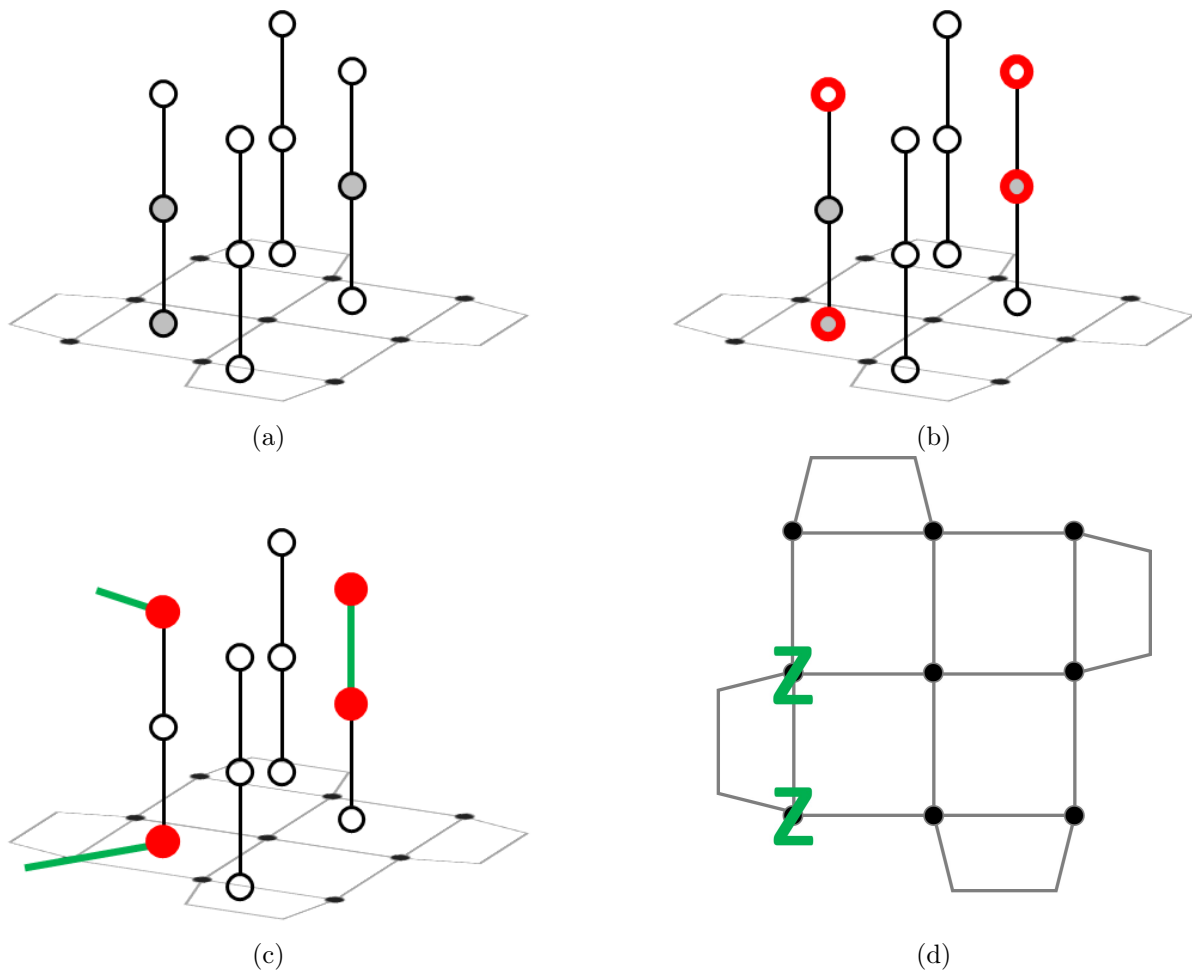


Figure 3.3: Specific example of MWPM decoding method on a distance-3 surface code patch. (a) Stabilizer measurement outcomes are represented on a 3D grid, ± 1 outcomes as white/grey circles. (b) Vertices, where the measured value differs from the previous round, are marked with red circles. (c) The minimum weight set of edges, which perfectly connects the marked vertices denoted by green color. (d) This set of edges forces the correction including two Pauli-Z operators. Figure taken from Ref. [117]

To obtain a fermionic description of the surface code, the $|0\rangle$ and $|1\rangle$ states of the physical qubits are represented as a fermion occupying the 'left' or the 'right' site of a double quantum dot, respectively. These two fermionic modes \hat{a}_0 and \hat{a}_1 satisfy the anticommutation relations

$$\{\hat{a}_i, \hat{a}_j\} = 0, \quad \{\hat{a}_i, \hat{a}_j^\dagger\} = \delta_{ij}. \quad (3.62)$$

To make use of the FLO tools, one introduces two Majorana operators (Majoranas) for each mode as

$$\hat{c}_1 = i(\hat{a}_1 - \hat{a}_1^\dagger), \quad \hat{c}_2 = \hat{a}_0 + \hat{a}_0^\dagger, \quad (3.63)$$

$$\hat{c}_3 = i(\hat{a}_0 - \hat{a}_0^\dagger), \quad \hat{c}_4 = \hat{a}_1 + \hat{a}_1^\dagger. \quad (3.64)$$

They are similar to fermionic operators, in that different Majoranas anticommute; however, all Majoranas are self-adjoint and square to the identity. The advantage of introducing Majoranas is that initialization of the code, coherent errors, and sampling of the measurement statistics of the stabilizer operators can all be mapped to the time evolution of a noninteracting fermionic system [115].

By introducing four Majoranas, a four-dimensional Hilbert space is assigned to each physical qubit and the so-called C_4 code is realized [15], with the stabilizer operator

$$\hat{S}_{C_4} = -\hat{c}_1\hat{c}_2\hat{c}_3\hat{c}_4, \quad (3.65)$$

and Pauli operators:

$$\hat{X} = i\hat{c}_1\hat{c}_2, \quad \hat{Z} = i\hat{c}_2\hat{c}_3. \quad (3.66)$$

Representing the surface code data qubits with C_4 codes, as shown in Fig 3.4, a system of Majorana fermions is realized. The core numerical advantage of using FLO lies in the fact that these free fermionic modes (Gaussian states) can be collectively represented by a $2n \times 2n$ covariance matrix [115], where n is the number of data qubits. Computing the time evolution of the system is equivalent to updating the covariance matrix, which allows sampling of the logical rotation angle distribution, $\theta_L(\mathbf{s}, \mathbf{s}', \boldsymbol{\theta})$ in $\mathcal{O}(n^2)$ time [117]. The performed FLO simulations have the following steps:

1. The rotation angles $\boldsymbol{\theta}$ of the quasistatic coherent errors are drawn from independent Gaussian distributions with zero mean, and identical standard deviations σ .
2. The perfect multi-cycle syndrome \mathbf{s} is sampled from the distribution $P(\mathbf{s})$.
3. The logical rotation angle $\theta^*(\mathbf{s}, \boldsymbol{\theta})$ (see Eq. (3.57)) is calculated (modulo π) based on the syndrome \mathbf{s} .
4. From the perfect syndrome \mathbf{s} , the noisy multi-cycle syndrome \mathbf{s}' is generated using the distribution $P(\mathbf{s} \rightarrow \mathbf{s}')$.
5. The logical rotation angle $\theta_L(\mathbf{s}, \mathbf{s}', \boldsymbol{\theta})$ of the final state is calculated by considering the effect of the correction operation $\hat{C}_{\mathbf{s}'}$, as per Eq. (3.59).

Note that the MWPM algorithm is used in the last step only.

3.4.4 Numerical results

I used the FLO method, as implemented in [117], to simulate the surface code under quasistatic phase damping and readout errors for code sizes up to $d = 17$. I sampled the distribution of the logical rotation angle, and computed the logical error rate in the following way:

$$p_L(\sigma) \approx \frac{1}{N_{\text{sample}}} \sum_{i=1}^{N_{\text{sample}}} \sin^2 \left(\theta_L(\mathbf{s}^{(i)}, \mathbf{s}'^{(i)}, \boldsymbol{\theta}^{(i)}) \right), \quad (3.67)$$

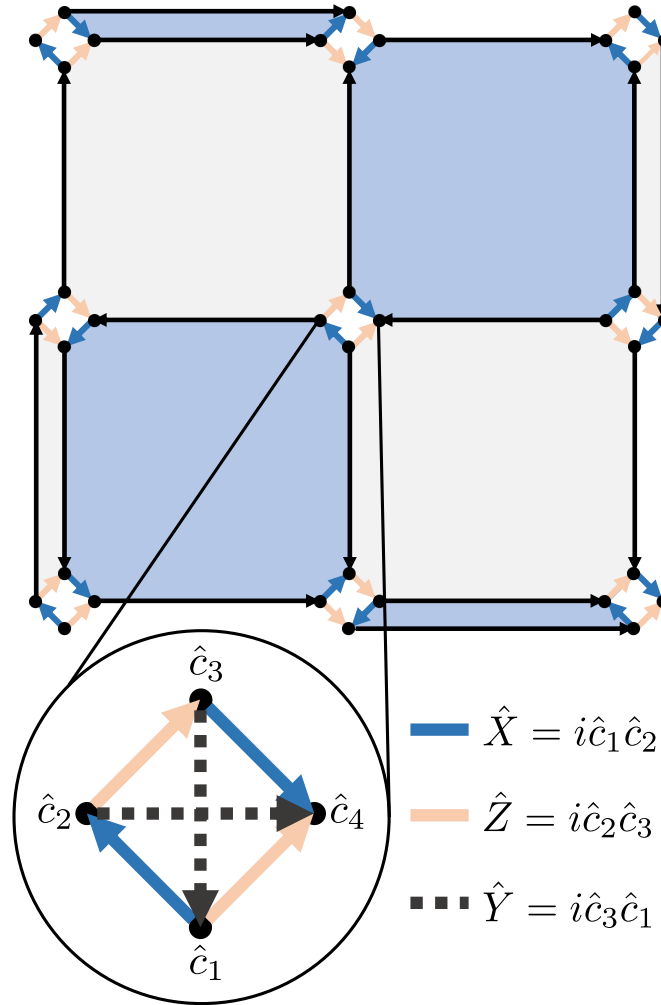


Figure 3.4: The Majorana representation of the surface code involves physical quantum bits represented by C_4 codes. Directed Majorana pairs (arrows) realize Pauli operators. The $\hat{S}_{C_4} = -\hat{c}_1\hat{c}_2\hat{c}_3\hat{c}_4$ operator stabilizes the qubit subspace (thus the operators $\hat{S}_{C_4}\hat{X}$, $\hat{S}_{C_4}\hat{Y}$, and $\hat{S}_{C_4}\hat{Z}$ are valid Pauli operators as well). Link operators - used to rewrite the surface code logical state - can be defined as Majorana pair operators connecting neighboring C_4 codes (black arrows). There is freedom in the orientation of link operators, but the product of links around each plaquette must be equal to the stabilizer defined on the plaquette.

where N_{sample} denotes the sample size.

Fig. 3.5(a) shows that I observe threshold behavior: for small physical error rates, increasing the code distance suppresses logical errors, while above the threshold, that is not true, logical errors accumulate and error correction fails. When the rates of physical and readout errors are the same, $p = q = \langle \sin^2 \theta \rangle$, I find that the threshold is $p_{\text{th}} \approx 2.85\%$, see Fig. 3.5(b). This is close to the threshold with Pauli Z errors and readout errors. For the toric code - that is a surface code with periodic boundary conditions - it is $2.93 \pm 0.02\%$ [114]. I also carried out Monte Carlo simulations to investigate phase-flip errors. Interestingly, I have found that the threshold value coincides with the above-mentioned 2.85%, however, the corresponding logical error rate is different for the two error models: in my case $p_L(p_{\text{th}}) \approx 7\%$, but for the combination of phase-flip and readout errors it is slightly higher, around 8.5%. This relative difference is sustained throughout the physical error rate window of Fig. 3.5(b) (not shown).

I have also investigated how varying the rate p of random coherent errors and q of readout errors independently affect the threshold of the surface code. Results are shown in 3.6. For many pairs of p and q , I numerically assessed whether scaling up the surface code decreases the logical error rate (scalable quantum error correction, green area) or increases it (quantum error correction does not work, red area). The threshold should be in between these regions. For example, if the physical error rate is at the 1% level, the surface code is quite robust against readout errors, scalable even with relatively high $q \approx 8\%$. However, if the readout error rate is at the 1% level, the surface code requires the coherent error rate to be below 4%.

3.5 Results for the distance-3 surface code and their relation to experiments

In this section, I discuss the implications of my results for the smallest surface code ($d = 3$) capable of error correction and their relation to experiments.

For physical error rates much below the threshold, $p \ll p_{\text{th}} \approx 2.85\%$, numerical simulations could only provide accurate results by significantly increasing the number of samples which is not feasible. However, it would also be interesting to see how the surface code performs in this regime. For the distance-3 surface code, I could carry out analytic calculations using a MWPM-based look-up table decoder, setting the weights of 'spacelike' and 'timelike' edges equal. For 3 rounds of error correction with readout error rate equal to physical error rate, $q = p$, I find that the logical error rate up to leading order is given by

$$p_L^{(d=3)} \approx 118p^2. \quad (3.68)$$

Interestingly, this expression is the same for independent phase-flip and readout errors. Thus, for small error rates, I expect similar behavior for the two models.

I consider an error correction experiment useful when the logical error rate of the encoded qubit is lower than the error rate of a single physical qubit, $p_L < p$. To study when this break-even condition is achieved, I compute the logical error rate p_L for several fixed values of physical error rate p and the readout error rate q for $d = 3$. Results are shown in Fig. 3.7. Again, I see that coherent errors are more harmful to the surface code quantum memory than readout errors: to achieve break-even, the physical error rate needs to be pushed below 1%, however, in this regime, readout errors up to 6% are tolerated.

I now connect these results to experimentally relevant error parameters, focusing on semiconductor spin qubits, to estimate the expected performance of a small surface code experiment based on currently available spin qubit hardware. My considerations expand upon earlier theoretical quantum error correction studies focusing on spin qubits [187–193].

The solid black curve in Fig. 3.7 shows my estimate for the physical and readout error rates, based on recent experimental data [194] obtained for spin qubit readout in a double quantum

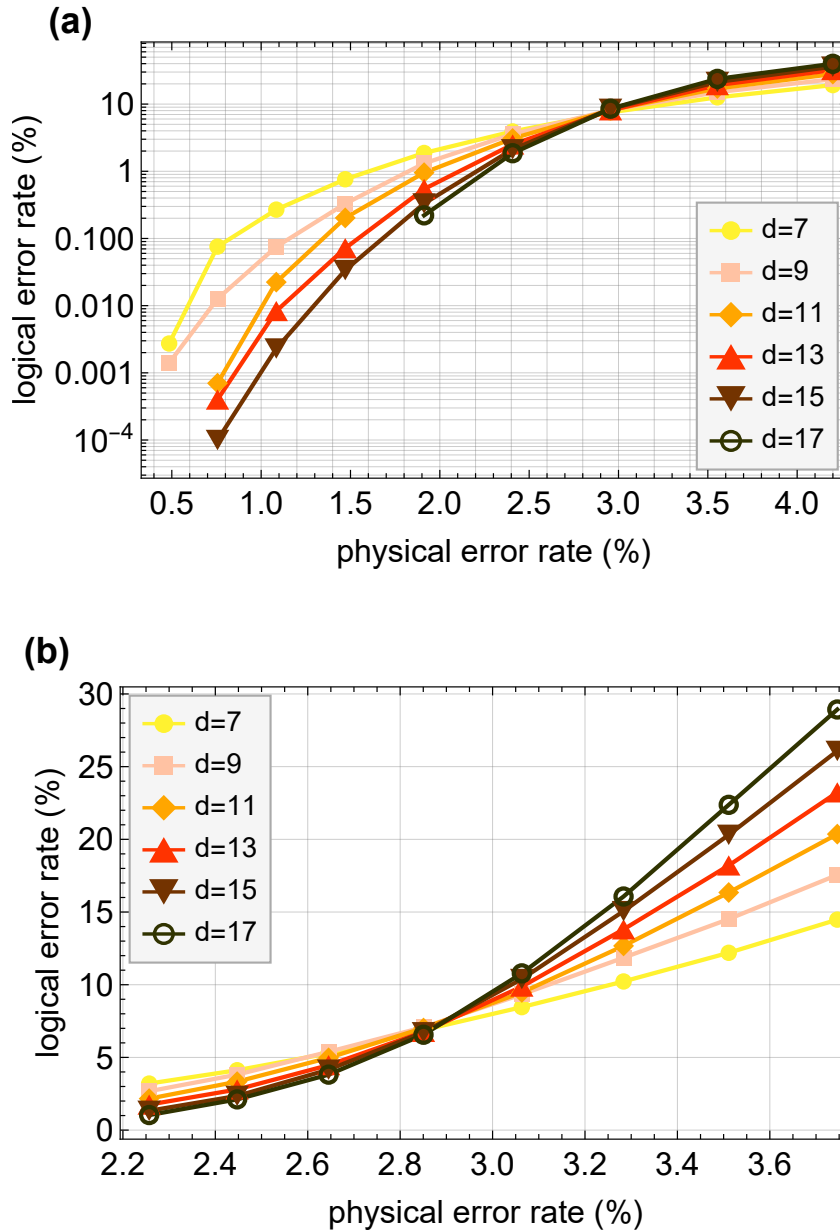


Figure 3.5: Surface code threshold with quasistatic phase damping and readout errors for $p = q$. Data points show the numerically obtained logical error rate (maximum infidelity), for different code distances d , with $p = q = \langle \sin^2 \theta \rangle$ being the physical error rate p and readout error rate q , that are kept equal for this plot. Each point is a result of $N_{\text{sample}} = 10,000 \times 100$ simulations: the multi-cycle syndrome \mathbf{s} was sampled for 10,000 random θ angles, simulating 100 random readout error configurations in each case. (a) Logical error rate for a wide range of physical error rates. (b) Zoom-in of (a) into a narrow window of physical error rates in the vicinity of the threshold. The graph confirms the existence of a threshold at $p_{\text{th}} \approx 2.85\%$.

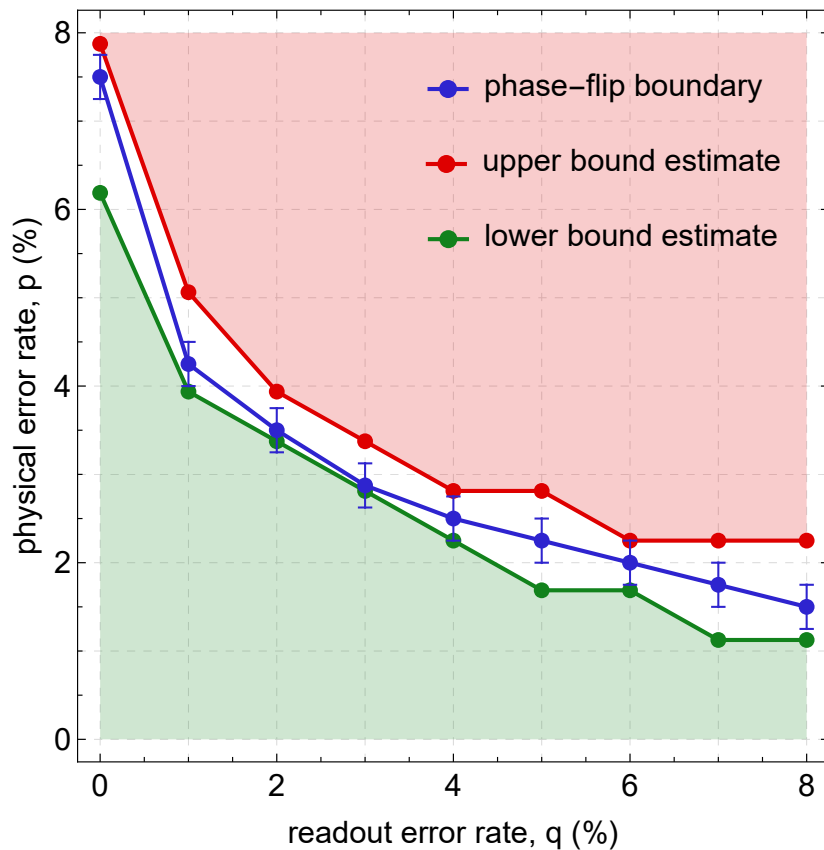


Figure 3.6: Surface code threshold with quasistatic phase damping and readout errors. On the (p, q) plane, threshold lines were identified by simulating 16 different values of p (equidistant in $0 < p \leq 9\%$) for a fixed q value, for code distances $d = 7, 9, 11, 13, 15$. For each q and d , a lower bound (green points) and an upper bound (red points) for the p threshold were estimated. The lower estimate is the greatest value of p at which the maximum infidelity decreases as the code distance increases. The upper estimate is the smallest value of p at which the logical error rate increases as the code distance increases. I also carried out Monte Carlo simulations to investigate phase-flip errors and numerically determined the threshold values (blue points) for asymmetric p and q values. For simplicity, the blue error bars are set to 0.25, which was the step size for the physical error rate in each individual simulation.

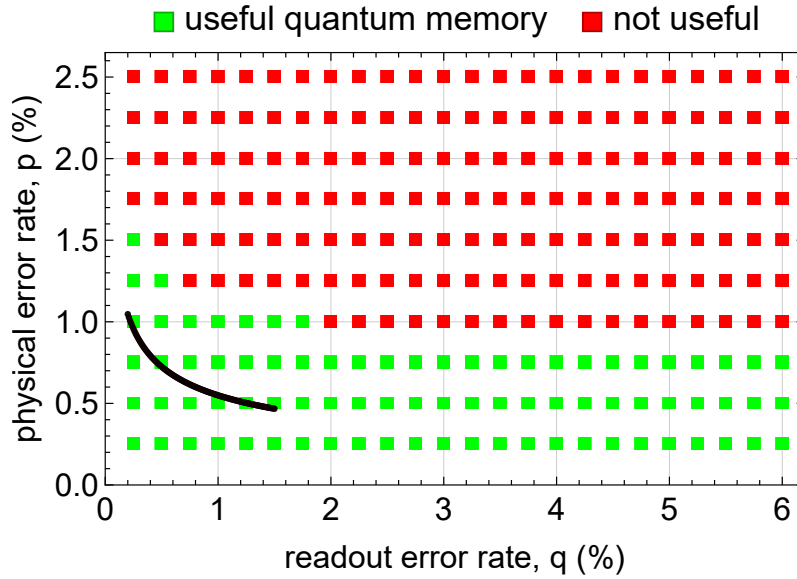


Figure 3.7: Comparison of logical and physical error rates on the (p, q) plane for the surface code with code distance $d = 3$. The green color indicates $p_L < p$, while the red color is for $p_L \geq p$. The black line shows estimated physical and readout error rates based on state-of-the-art spin qubit experiment, Ref. [194]. It corresponds to readout time $0.5 \mu\text{s} - 0.7 \mu\text{s}$.

dot. Points of the curve correspond to different measurement integration times, as I explain below. The black curve lies inside the break-even region (green), indicating that scaling up the hardware with the same high-quality components could make useful surface-code-based quantum error correction attainable with semiconductor spin qubits.

The black curve in Fig. 3.7 is obtained from the data [194] as follows. I connect the coherent error strength σ , and the corresponding physical error rate p , to the experimentally available inhomogeneous dephasing time T_2^* and measurement integration time T_{meas} by assuming that the Larmor angular frequency ω_L of each idling data qubit exhibits spatially uncorrelated, Gaussian, quasistatic fluctuations, with standard deviation $\sigma_{\omega_L} = \sqrt{2}/T_2^*$. This detuning of the Larmor frequency of the j th data qubit of the code implies a small random rotation θ_j around the z-axis on that qubit. Typically, the duration of a quantum error correction cycle is dominated by the measurement integration time T_{meas} of the measure qubits, therefore I estimate the standard deviation σ of the angle θ_j of the coherent error as

$$\sigma(T_{\text{meas}}) = \sigma_{\omega_L} \cdot T_{\text{meas}} = \sqrt{2} \frac{T_{\text{meas}}}{T_2^*}. \quad (3.69)$$

From this result, I express the physical error rate $p(T_{\text{meas}})$ using Eq. (3.12).

I can also provide a realistic estimate for the dependence of the readout error rate q on the measurement integration time. For this, I use experimental data, namely, the data set corresponding to the initial state T_- in Fig. 3(d) of Ref. [194]. In the measurement integration time range $0.5 \mu\text{s} - 0.7 \mu\text{s}$, the data is well approximated by this power law:

$$q(T_{\text{meas}}) \approx \left(\frac{\tau}{T_{\text{meas}}} \right)^5, \quad (3.70)$$

where $\tau = 0.21 \mu\text{s}$ is a time constant.

The solid black curve in Fig. 3.7 shows the parametric dependence of q and p on T_{meas} , based on the considerations and numerical factors of the previous two paragraphs, and inhomogeneous

dephasing time value of $T_2^* = 10 \mu\text{s}$ [194]. The black curve lies in the green region, where the logical error rate is lower than the physical error rate. Based on these considerations, I conclude that although it is challenging to perform a 9-qubit surface code experiment, semiconductor spin qubits have the potential to achieve break-even in the near future. In experiments, where the readout is significantly slower than in the one I cited, it could be fruitful to convert high readout fidelity to shorter readout time duration [191], since the surface code is more robust against readout errors than coherent errors. Note that the above considerations can be significantly improved with the goal of a more realistic description of quantum memory experiments, e.g., by taking into account gate errors both on data and measure qubits, etc.

Finally, I also relate my simulation results to superconducting quantum computing platforms. On the one hand, transmons are designed to be protected from dephasing [64], and hence their decoherence is often dominated by relaxation, which is excluded from my model. On the other hand, alternative superconducting qubits have been developed [195–198], in which qubit relaxation is suppressed and pure dephasing due to charge noise or flux noise is the dominant decoherence mechanism. (For an informative summary, see Ref. [199], and Table 1 therein.) For such superconducting qubits, the quasistatic phase damping model is a good starting point. Therefore, it is an interesting and relevant future task to assess the performance of quantum error correction based on such qubits, utilizing the efficient simulation methodology (FLO) applied here.

3.6 Conclusions and outlook

I introduced the error model of quasistatic phase damping, which is a simplified model that describes Larmor-frequency fluctuations due to $1/f$ noise. These Larmor-frequency fluctuations amount to unwanted coherent rotations whose axis is uniform, but the rotation angle is random across the qubit register. I showed that this quasistatic phase damping error is equivalent to independent single-qubit Pauli phase-flip errors in the case of a single cycle of error detection or error correction. However, for multiple cycles, quasistatic phase damping is distinct from a phase-flip error.

Furthermore, I numerically investigated the performance of the surface code as quantum memory in the presence of quasistatic random coherent errors on the physical qubits as well as (phenomenological) readout errors. I utilized the Fermionic Linear Optics simulation framework to perform large-scale numerical experiments and established the surface code error correction threshold. The threshold is found to be close to that with independent phase-flip errors and readout errors. However, at the threshold, the logical error rate for quasi-static phase damping combined with readout errors is lower than that for independent phase flips and readout errors. This suggests that in terms of surface code quantum memory, quasistatic phase damping is less harmful. Threshold line estimates in the plane spanned by the strengths of the coherent error and the readout error also show that quasistatic phase damping and the independent phase-flip error model have similar threshold values.

I evaluated the effects of quasistatic phase damping on the distance-3 surface code, and established the break-even boundary line for this code on the parameter plane of the physical error rate and the readout error rate. Finally, I discussed the relevance of these results to solid-state qubit platforms, including semiconductor spin qubits and superconducting qubits. The results could provide useful design guidelines for future experiments based on these quantum computing platforms.

The combination of random Pauli errors and coherent errors was considered in Refs. [200] and [201]. A possible extension of my error model is the combination of quasistatic phase damping and random Pauli errors. Including also random Pauli X and Y errors, as, e.g., in depolarizing noise, however, is unfortunately beyond the scope of this approach, due to the constraints of the

FLO simulation.

Most recently, generic single-qubit coherent errors (rotations around arbitrary axis) were considered in the surface code by mapping to statistical physical models [202], and the approximate simulation of Clifford circuits with a small number of coherent errors also became feasible [203]. These works are paving the way to a complete understanding of the effect of coherent errors on quantum error correction.

Chapter 4

Surface code error correction with crossbar spin qubit architectures

This chapter is based on publication [IV](#).

Several architectural proposals have been made for scaling up spin qubit platforms [[33](#), [187](#), [189](#), [204–208](#)]. One difficulty of controlling, e.g., a few thousand qubits on a single chip is a large number of *control lines*. The quantum dots hosting the spin qubits are defined via gate electrodes (plunger gates and barrier gates, described in [Sec. 4.1](#)) whose dc voltage supply is at room temperature, while the chip itself is usually in a dilution refrigerator at millikelvin temperature. I will refer to the wires connecting the chip with the power supply, and also the gate electrodes on the chip, as control lines. Driving the qubit (e.g. single-qubit rotations) requires ac voltage (or ac current, in case of magnetic control using an on-chip micromagnet) as well, further increasing the number of control lines needed. When the qubits are addressed individually, the number of control lines scales linearly with the qubit count. This would make it impractical to accommodate few thousand qubits on a single chip. A crossbar control architecture was proposed to overcome this issue, where the number of control lines scales as the square root of the qubit count [[209](#)], making it a good candidate for realizing large-scale quantum computers.

The crossbar architecture proposed and studied in [[188](#), [209](#)] consists of a two-dimensional array of quantum dots (see [Fig. 4.1](#)) with barrier gates (yellow lines in [Fig. 4.1](#)) separating them horizontally and vertically as well. These barrier gates control the interdot tunneling amplitudes, whereas the dot potentials (*on-site energies*) are controlled via diagonal control lines (*plunger gates*, white and gray in [Fig. 4.1](#)) which in turn enable the tuning of the charge configuration. A recent experiment has already demonstrated shared control in a 4×4 crossbar array in planar germanium [[210](#)].

To execute a quantum circuit on quantum computing hardware, the circuit has to be translated to a physical pulse sequence. In the case of this spin qubit crossbar architecture, the physical pulse sequence consists of gate-voltage pulses that govern the spatial motion of the electrons, and microwave magnetic pulses that trigger single-qubit logical gates.

I envision this translation procedure as a sequence of layers, which I depict in [Fig. 4.2](#). Here, I describe these layers briefly and leave details and examples for the bulk of the chapter. The quantum circuit serves as the input for this procedure. The first step is to express the quantum circuit in terms of the native gates of the architecture. The second step, characteristic of sparse spin qubit arrays (as well as other architectures where the qubits are mobile, e.g., trapped-ion and neutral-atom quantum computers), is to design the motion of the qubits on the lattice; this layer is termed *routing and scheduling protocol* in [Fig. 4.2](#). A subsequent task

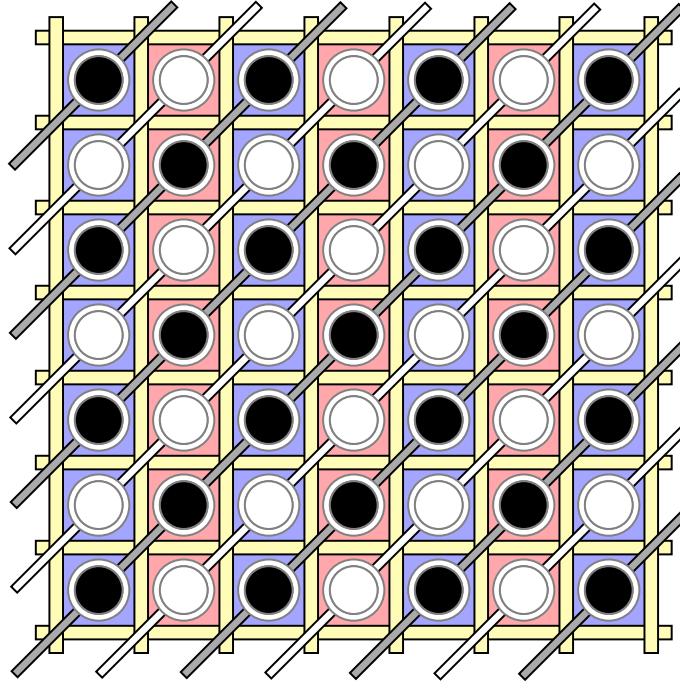


Figure 4.1: Schematics of the crossbar architecture. Circles represent quantum dots, separated by barrier gates (yellow), with on-site energies controlled by the diagonal plunger gates (gray and white lines). Black circles are the electrons (or holes, in p-type devices); the spin of each electron is a qubit. In the odd columns (light blue background) each qubit has Larmor frequency ω_o , whereas in the even columns (light red background) each qubit has Larmor frequency ω_e .

is to translate the protocol to an *abstract pulse sequence*: most importantly, this encodes the structure of subsequent gate-voltage settings that are required to move the electrons as specified by the routing and scheduling protocol. Finally, the physical pulse sequence provides a physical specification of the abstract pulse sequence, e.g., expressing the gate-voltage settings in microvolts (or microelectronvolts) and timings in microseconds, shapes of magnetic-field pulses specified in milliteslas (or microelectronvolts) and microseconds, etc.

After the proposal [209], follow-up work devised a routing and scheduling protocol for the surface code quantum memory implemented in the crossbar architecture [188], and proposed quantum circuit compilation strategies for the crossbar architecture [211, 212], down to the ‘routing and scheduling protocol’ layer of the stack (see Fig. 4.2). My results are complementary to these earlier works, as I focus on the remaining layers of the stack, the ‘abstract pulse sequence’ and ‘physical pulse sequence’ layers (denoted green in Fig. 4.2).

In this chapter, I study the opportunity of storing a surface code logical qubit on the crossbar architecture studied in [188, 209]. My contributions are enumerated as follows:

- (i) I decompose the surface code stabilizer measurement circuits in terms of single-qubit and two-qubit gates that are native to the spin-qubit architecture. This is a correction of the decomposition in Ref. [188].
- (ii) I describe a revised routing and scheduling protocol (compared to Ref. [188]) for the implementation of such a stabilizer measurement cycle.
- (iii) I make an estimate for the scaling of logical error with code distance, based on the framework established in Sec. 5.4 of Ref. [188], but applying that to my updated protocol.

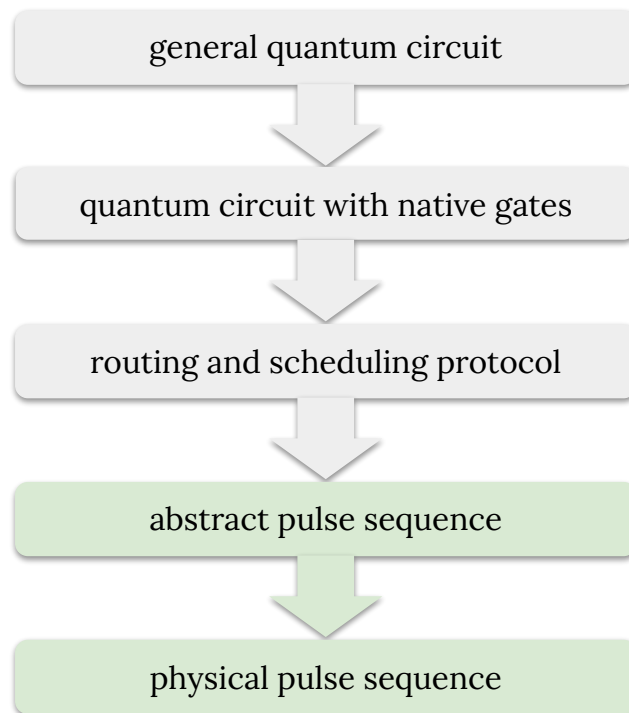


Figure 4.2: Layers for the quantum computing stack for a crossbar spin-qubit architecture. Special layers, characteristic of this architecture, are the ‘routing and scheduling protocol’, which describes the motion of the electrons in the array, and the ‘abstract pulse sequence’, which encodes the structure of subsequent gate-voltage settings required to move the electrons according to the routing and scheduling protocol. See text for a more detailed description of all layers. Layers denoted by gray color were also studied in earlier works: for the surface code in Ref. [188] and in a general compilation framework in Ref. [211]. Layers denoted by green color are addressed here.

- (iv) The surface code in this crossbar architecture can be operated in a *line-by-line* or in a *parallel* fashion [188]. The logical error rate, and its scaling with code distance d , depends strongly on this choice. For line-by-line operation, I determine the optimal code distance as a function of the physical qubit coherence time and the measurement time, and identify a parameter range where the logical error rate of the surface code quantum memory is less than the physical error rate (often referred to as the *break-even* performance of the code).
- (v) I construct an abstract pulse sequence (i.e., for gate voltage and ESR pulses) for the parallel operation of the surface code stabilizer measurement cycle.
- (vi) I devise a verification algorithm for adiabatic qubit shuttling-based routing in the shared-control crossbar architecture. As inputs, one needs to specify (i) the desired movements of the electrons (qubits) in the array, and (ii) the abstract pulse sequence specifying the gate-voltage changes. Then, the algorithm verifies if the abstract pulse sequence indeed generates the desired movements.
- (vii) I describe how to implement the abstract pulse sequence physically.
- (viii) During the physical pulse sequence, crosstalk effects (namely, coherent phase errors) can occur on idle qubits, due to the built-in constraints of the crossbar architecture. I characterize these crosstalk errors during the surface code cycle. I also identify an experimentally relevant parameter regime where the estimated crosstalk errors are below the surface code threshold. These results suggest that these crosstalk errors can be mitigated by the surface code quantum error correction procedure.

As seen in the above list, contributions (i), (ii), (iii) and (iv) are corrections or modifications or slight extensions with respect to [188]. The errors I have identified in [188], along with my proposed corrections, are summarized in Table 4.1. I note that the errors I have identified are quantitative in nature, not affecting the qualitative conclusions of [188]. My contributions (v), (vi), (vii), (viii) go beyond the scope of [188].

The rest of this chapter is organized as follows. In Sec. 4.1, I describe the key features of the crossbar spin qubit architecture. In Sec. 4.2 I summarize the quantum circuits needed for the surface code stabilizer measurement cycle, I decompose them using the native spin qubit gates and I describe the updated scheduling protocol to transpile these circuits to the crossbar architecture (i–ii). Moreover, I estimate the scaling of the logical error rate using the framework of [188] (iii–iv). In Sec. 4.3 I propose a physical pulse sequence for the stabilizer measurement cycle, and compute the crosstalk errors that occur during my protocol (v–viii).

4.1 The crossbar spin qubit architecture

In this section, I briefly introduce the crossbar spin qubit architecture [188, 209], which is shown in Fig. 4.1.

It consists of a two-dimensional array of quantum dots with barrier gates (yellow bars in Fig. 4.1) separating the dots horizontally and vertically. These barrier gates control the interdot tunneling amplitudes. The dot potentials (*on-site energies*) are controlled via diagonal control lines (a.k.a. *plunger gates*, shown as white and gray bars in Fig. 4.1) which enable the tuning of the charge configuration (up to the constraints originating from the shared-control structure).

Following [188, 209], I consider Loss–DiVincenzo qubits [41], i.e. single-electron (or single-hole) spin qubits. A static external magnetic field is applied throughout the array to set the qubit splitting. However, in the proposal of the crossbar architecture, there is a built-in inhomogeneity: the qubit Larmor frequencies are alternating column by column [209], as indicated by the blue and red shadings in Fig. 4.1. This alternating structure enables selective (semi-global) addressing of

No.	Result	Ref. [188]	My version
1	Decomposition of the CNOT gate in terms of $\sqrt{\text{SWAP}}$ gates	Fig. 4	Fig. 4.5
2	Surface code Z-stabilizer measurement circuit decomposed with two-qubit $\sqrt{\text{SWAP}}$ gates and single-qubit gates	Fig. 11	Fig. 4.6
3	Time step count per step in terms of gate types for the line-by-line implementation of the surface code stabilizer measurement cycle	Table 4	Table 4.2
4	Number of operations per qubit type (data/ancilla qubit) for the X and Z stabilizer measurement cycles	Table 5	Table 4.4
5	Estimated time of a full stabilizer measurement cycle using line-by-line operation	Eq. (18)	Eq. (4.2)
6	Average physical error probability per quantum stabilizer measurement cycle	Eq. (20)	Eq. (4.5)

Table 4.1: List of corrections (1-2) and modifications (3-6) I propose compared to Helsen *et al.* [188].

the qubits located at even or odd columns, and single-qubit gates can be performed via Electron Spin Resonance (ESR), applying an ac magnetic field that has a transverse component with respect to the static magnetic field.

Qubits can also move on the grid to unoccupied sites via coherent electron shuttling [213–224]. Moving the qubits between two sites with different Larmor frequencies, ω_e and ω_o (for brevity, I refer to angular frequencies as frequency throughout the chapter), can effectively induce a coherent rotation around the axis of the external magnetic field. Such a rotation can serve as a single-qubit gate [40], or as an identity operation if proper timing ensures that a rotation angle is an integer multiple of 2π .

A native two-qubit gate of spin qubit architectures is the $\sqrt{\text{SWAP}}$ gate that is carried out utilizing the exchange interaction between two neighboring qubits [41, 49, 225]. In the crossbar architecture, this is realized by moving the qubits to neighboring sites and lowering the potential barrier that separates them [226]. The diagonal plunger gates could also be used for radiofrequency (RF) charge sensing via gate reflectometry, enabling qubit readout via capacitance measurement at the Pauli spin blockade transition [209]. Qubit readout is also possible via charge sensors located in the vicinity of the quantum dots of the array [210].

Importantly, all these considerations rely on a high level of uniformity throughout the spin qubit processor. Throughout Sec. 4.2 and 4.3, I assume perfect uniformity of the array. Also note that due to the shared control, crosstalk effects (e.g. unwanted rotations, spurious shuttlings) might also be induced, as I describe in Sec. 4.3.4.

4.2 Surface code stabilizer measurement cycles

The surface code encodes a logical qubit in the common +1 eigenspace of the X-type and Z-type parity check operators (stabilizers), as shown in Fig. 1.8(a). In this section, I briefly summarize the quantum circuits of stabilizer measurements. The section is structured as follows. In Sec. 4.2.1, I list the quantum circuits for the surface code stabilizer measurement cycle [100]. In Sec. 4.2.2, I decompose these circuits in terms of native gates of the crossbar spin qubit architecture. Such a decomposition was included in Ref. [188], but I identify a few errors there, which I correct. These errors and the proposed corrections are collected in Table 4.1. In Sec. 4.2.3, I provide an updated version of the scheduling protocol described in Sec. 4.4 of Ref. [188], using

parallel operation. In Sec. 4.2.4, I discuss the case when parallel operation is not feasible. Finally, in Sec. 4.2.5 I estimate the scaling of the logical error probability for a crossbar system, using the phenomenological error model introduced in Ref. [188].

4.2.1 Z-cycle circuit, X-cycle circuit with CNOT gates

Experimentally, the measurement of the stabilizers, i.e., checking the joint parity of data qubits on a plaquette, is performed by measuring an ancillary qubit after entangling the latter with the four corresponding data qubits. In principle, this is possible using one ancilla per lattice face [see Fig. 4.3(a)] exploiting the standard quantum circuits depicted in Figs. 4.4(a) and (b) for the Z- and X-type stabilizers, respectively. Both circuits use four CNOT gates for entangling data qubits with the ancilla. Ancilla qubits marked red in Fig. 4.3(a) are labeled by A in Fig. 4.4(a), and they are used to measure the Z-type stabilizers. Similarly, ancilla qubits marked blue in Fig. 4.3(a) are labeled by B in Fig. 4.4(b) and they are used to measure the X-type stabilizers. For the X-type stabilizer measurement, two Hadamard gates are also needed, as shown in Fig. 4.4(a). During a complete Z-cycle (X-cycle), all of the Z (X) stabilizers are measured.

4.2.2 Z-cycle circuit, X-cycle circuit using $\sqrt{\text{SWAP}}$ gates

Here, following [188], I compile the circuits of Figs. 4.4(a) and (b) such that they utilize the $\sqrt{\text{SWAP}}$ gate (described in Sec. 4.1) instead of the CNOT as the standard two-qubit gate. The stabilizer measurement circuits can be decomposed using the identity shown in Fig. 4.5 which uses two $\sqrt{\text{SWAP}}$ gates and five single-qubit gates for the CNOT [41]. For the single-qubit gates, I use Hadamard gates, the Pauli-Z gate, the S gate (see Table 1.1), and its Hermitian conjugate, the S^\dagger gate.

Substituting this decomposition into the previous circuits of Figs. 4.4(a) and (b), after merging the subsequent Hadamard gates, I obtain the Z and X stabilizer measurement circuits with native gates of the crossbar architecture as shown in Fig. 4.6 and Fig. 4.7, respectively. Note also that I shifted the mid-circuit S and S^\dagger gates to the end of the circuits wherever it was possible.

4.2.3 Routing and scheduling protocol for parallel operation

In this section, I consider a protocol where the Z and X stabilizer measurement cycles are performed sequentially. Readout via PSB (as described in Sec. 1.2.1) requires two quantum dots, therefore the role of X and Z ancilla qubits are swapped in the subsequent cycles, using one of them always as a reference qubit for the measurement of the other. I discuss how to implement (compile) the corresponding circuits to the crossbar architecture, overcoming the hardware constraints.

Fig. 4.3(b) shows a 5×5 crossbar array hosting 13 qubits in the bulk of a surface code patch. Data qubits are black, Z-type ancilla qubits (ancilla qubits A) are red, and X-type ancilla qubits (ancilla qubits B) are blue.

For the surface code Z-cycle, using the quantum circuit of Fig. 4.6, I propose an updated version of the protocol outlined in Sec. 4.4 of Ref. [188]. It incorporates corrections 1 and 2 of Table 4.1, moreover, it also contains new steps (Steps 4 and 9). The short description of this Protocol is the following (for a visual representation see auxiliary file ZcycleMovie.pdf available at the Zenodo repository [227]):

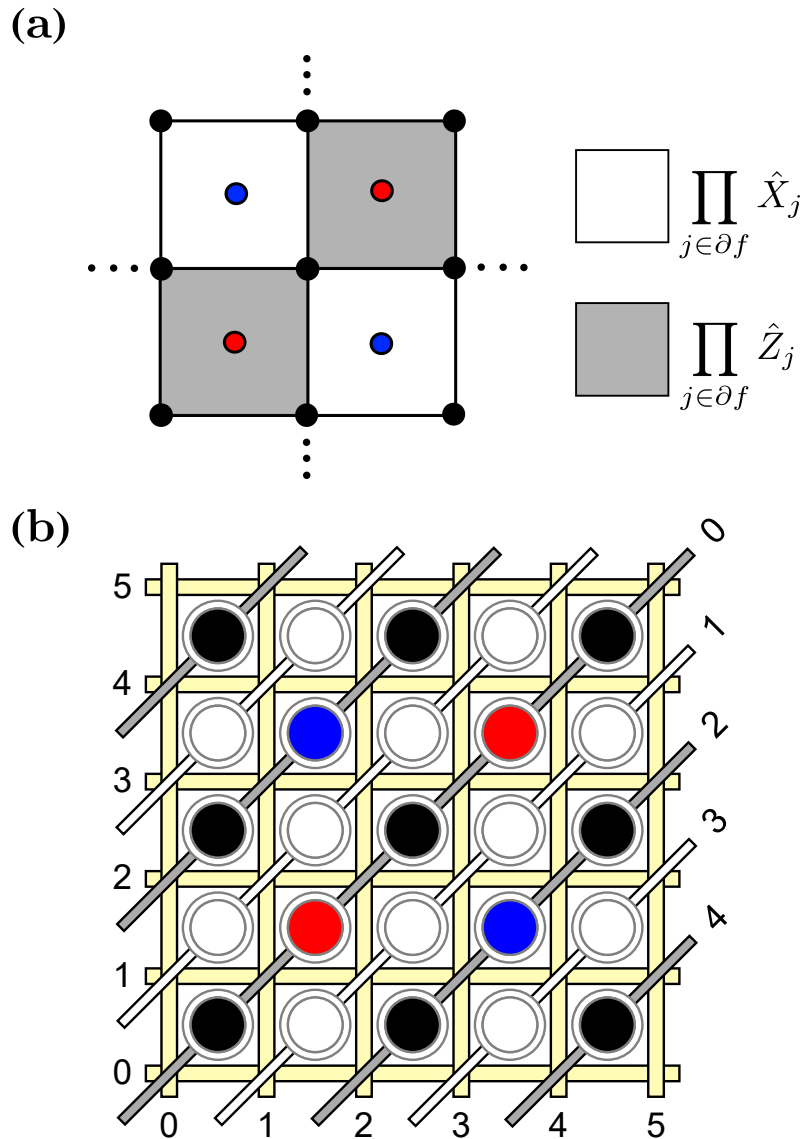


Figure 4.3: (a) Layout of the bulk of a surface code patch. The black dots are data qubits. Gray (white) plaquettes represent Z-type (X-type) stabilizer operators. Correspondingly, the red (blue) dots are the ancilla qubits for the Z (X) parity checks. I also use the notation ancilla qubit A and B for the red and blue qubits, respectively. (b) Same setup realized in a 5×5 crossbar array.

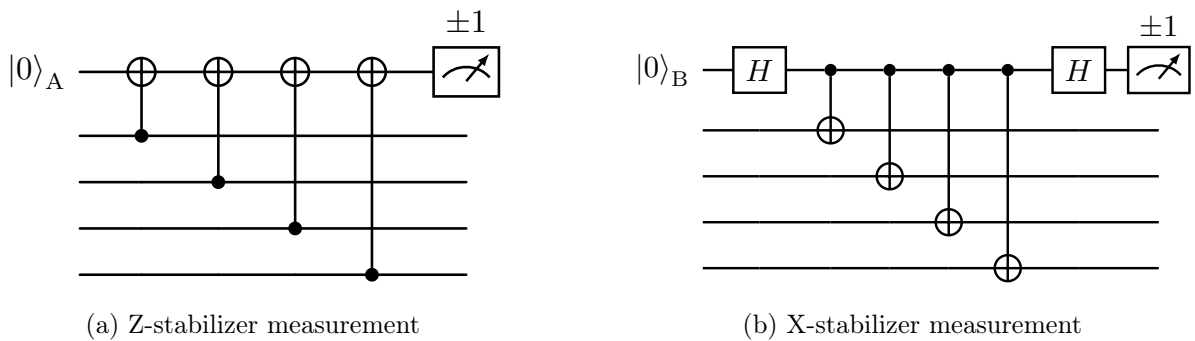


Figure 4.4: Surface code stabilizer measurement circuits [100].

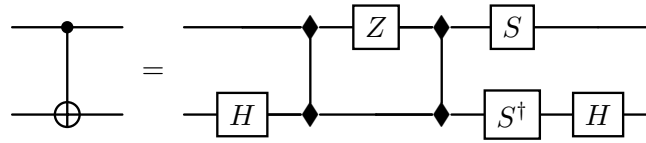


Figure 4.5: Decomposition of the CNOT gates (on the left) in terms of $\sqrt{\text{SWAP}}$ gates (connected diamonds on the right) and single-qubit gates that are native to the crossbar spin qubit architecture.

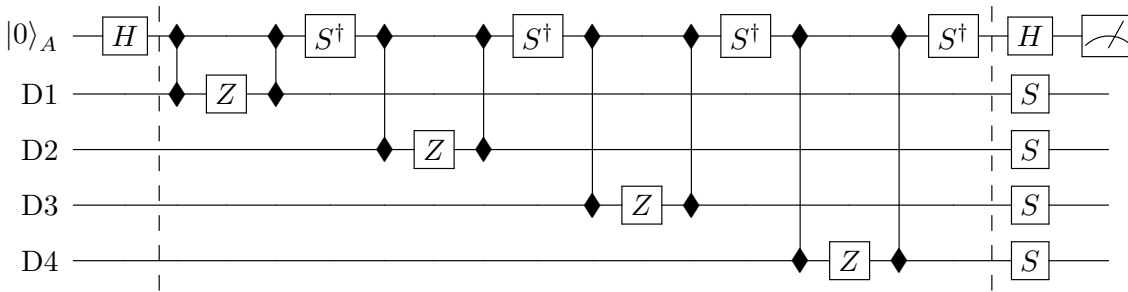


Figure 4.6: Surface code Z-stabilizer measurement circuit decomposed with two-qubit $\sqrt{\text{SWAP}}$ gates and single-qubit gates. In my Protocol, the gates before the first and after the second dashed line are realized by global ESR control. The gates between the first and second dashed lines are realized by shuttling. Labeling of the data qubits (D1, D2, D3, and D4) is consistent with Fig. 4.8.

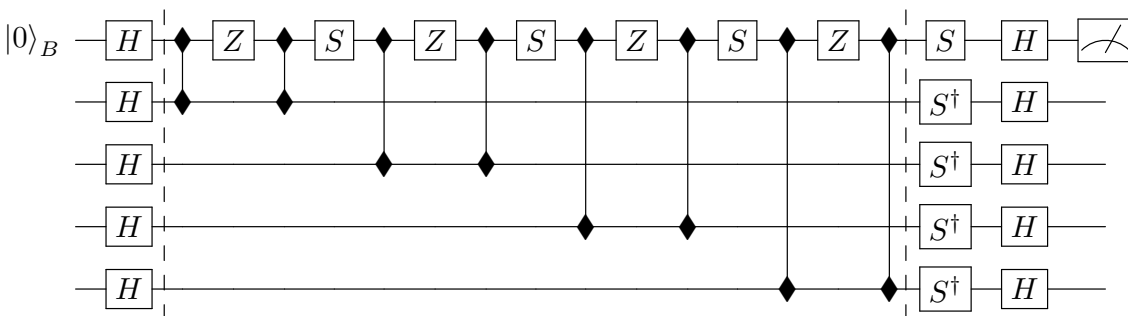


Figure 4.7: Surface code X-stabilizer measurement circuit decomposed with two-qubit $\sqrt{\text{SWAP}}$ gates and single-qubit gates. In my Protocol, the gates before the first and after the second dashed line are realized by global ESR control. The gates between the first and second dashed lines are realized by shuttling.

Routing and scheduling protocol

1. Initialize the idle configuration.
2. Apply global H gate to all ancilla qubits (located in even columns).
3. Go to the ‘rightward triangle configuration’, by moving the ancilla qubits one site to the right, see Fig. 7(b) of [188].
4. Apply global H gate to ancilla qubits B (located in even columns), to cancel the rotation they suffered in Step 2.
5. Perform the $\sqrt{\text{SWAP}}$ gates that entangle ancilla qubits A and the neighboring two data qubits (e.g. the gates that entangle ancilla qubit A and data qubits D1 and D2 in Fig. 4.6), interleaved with shuttling-based single-qubit rotations Z and S^\dagger on the data qubits and the ancilla qubit, respectively.
6. Go back to idle configuration.
7. Go to ‘leftward triangle configuration’, by moving the ancilla qubits one site to the left [188].
8. As a mirror image of Step 5, perform the two $\sqrt{\text{SWAP}}$ gates that entangle ancilla qubits A with the other two neighboring data qubits (e.g. the gates that entangle ancilla qubit A and data qubits D3 and D4 in Fig. 4.6), interleaved with shuttling-based single-qubit rotations Z and S^\dagger on the data qubits and the ancilla qubit, respectively.
9. Apply global H gate to ancilla qubits B (located in even columns).
10. Go back to idle configuration.
11. Apply global H gate to all ancilla qubits (located in even columns) and global S gate to all data qubits (located in odd columns).
12. Go to ‘rightward triangle configuration’ [188].
13. Perform PSB readout of ancilla qubits A using ancilla qubits B as reference qubits.
14. Go back to idle configuration.

I propose to perform the mid-circuit single-qubit gates (i.e., those between the vertical dashed lines in Fig. 4.6 and 4.7) via coherent qubit shuttling since all of them are rotations around the z -axis. When the external magnetic field is pointing in the z -direction, this is feasible with the proper timing. Single-qubit gates before the first and after the second vertical dashed line in Fig. 4.6 and 4.7 are conveniently performed by global rotations using ESR [188, 209], because the same gate has to be applied to all qubits located in all columns with the same color. ESR enables global rotations around any axis (e.g. with the combination of x and y axis rotations), thus S and S^\dagger gates can also be realized in this manner, as well as the Hadamard gate H . Note that compared to Fig. 4.6, the circuit corresponding to my routing and scheduling Protocol contains two extra Hadamard gates (Steps 4 and 9) on ancilla qubits B.

For the surface code X-cycle, I propose a similar protocol exchanging the role of ancilla qubits A with ancilla qubits B, based on the quantum circuit displayed in Fig. 4.7.

In principle, in an X or Z-cycle, each step described above could be executed simultaneously in each 4×4 unit cell of the crossbar array which has 4×4 spatial periodicity (see Fig. 4.8). In an

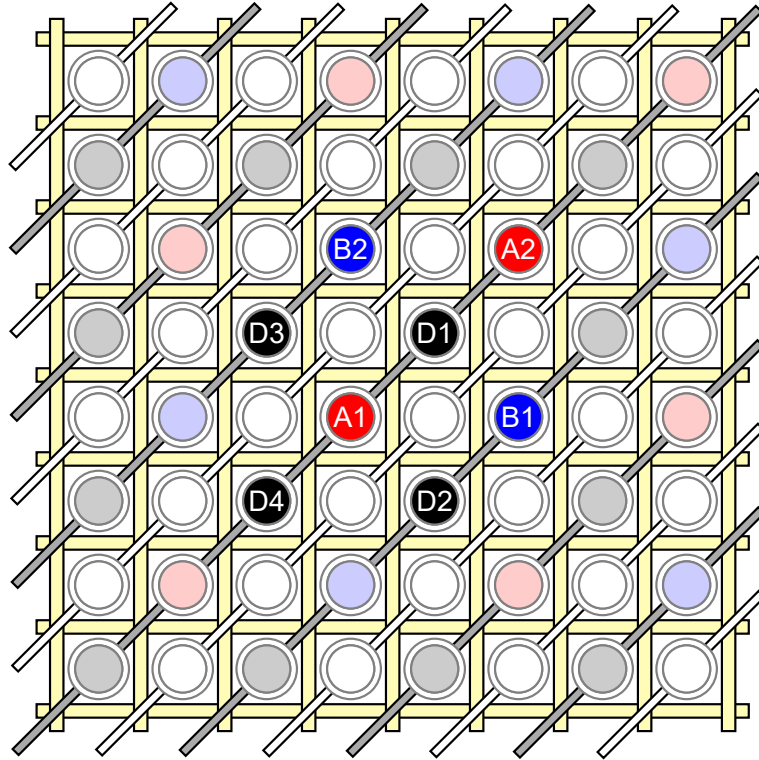


Figure 4.8: Data qubits and ancilla qubits in the idle configuration. The 4×4 unit cell of the grid is highlighted and the corresponding 8 qubits in this cell are numbered.

experimental setting, measurement of spin qubits is possible via spin-to-charge conversion and charge readout using charge sensors or gate-reflectometry [228, 229]. The latter measures the charge response (i.e. the quantum capacitance) of tunnel-coupled qubits to changing plunger gate voltage that tunes the on-site energy difference. This measurement is possible via the diagonal plunger gates. Here, I investigate the case when charge sensors are used for the readout, which has the advantage that vertical barrier activation is needed only for a short duration, reducing the amount of crosstalk errors (discussed in Sec. 4.3.4). Utilizing multiple charge sensors and PSB-based spin-to-charge conversion, qubit states across the chip could be inferred simultaneously [210]. Therefore, I assume that ancilla qubits could be measured in parallel via the parallel PSB readout scheme depicted in Fig. 4.9. Hence, I term the protocol described in this section *parallel operation*. In the next section, I discuss a scenario [188] where operations are not executed in parallel across the array.

4.2.4 Line-by-line implementation

One could also opt for line-by-line operation throughout the whole cycle to account for qubit-to-qubit variations with individual control (see Sec. 'Parallel operation' of Ref. [209], and Sec. 3 of Ref. [188]). *Line-by-line operation* means that except for global rotations, each operation (quantum gate, qubit shuttling, measurement) is done sequentially, column-by-column, or row-by-row. In particular, after performing Steps 1 and 2, Steps 3-6 (excl. Step 4 that is a global rotation) are applied only in the first two columns. At the end of this sequence, the array is returned to the idle configuration, and then the process continues with the next two columns, and so on, until reaching the end of the grid. This is followed by Steps 7-12 (excl. Step 9) performed in the same manner. Step 13 is performed row-by-row.

Following Ref. [188], I further divide each Step in my Protocol into *composite time steps* so

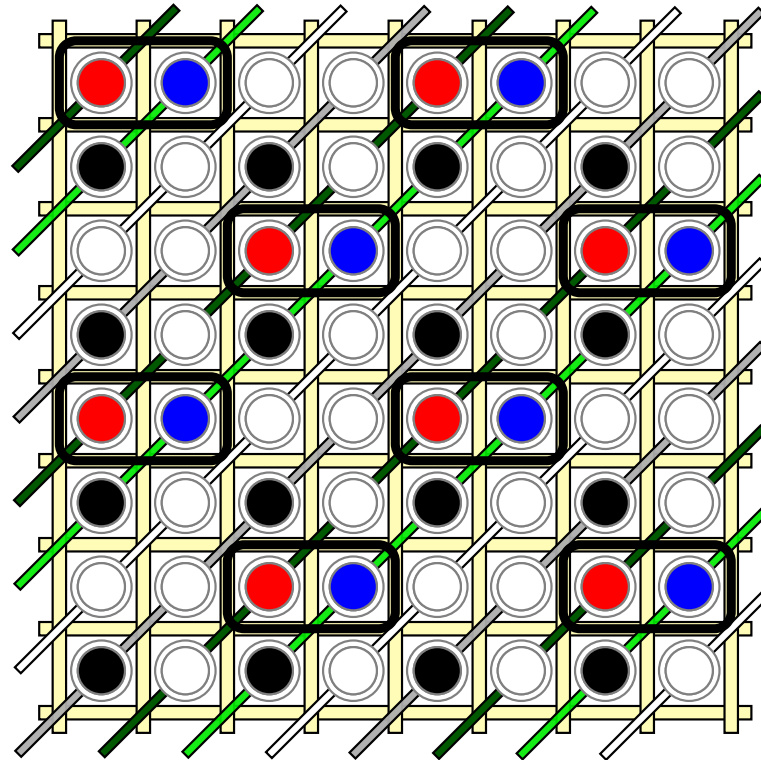


Figure 4.9: Parallel Pauli spin blockade readout of the red qubits (ancilla qubits A), using the blue qubits (ancilla qubits B) as reference qubits, in the surface-code Z-cycle. Charge sensors (not shown) are needed to perform readout in this configuration; these could be a set of sensor dots on the same chip [210], or sensors added in a 3D fashion [230–233]. The crossbar array is in the rightward triangle configuration [188]. On-site energies beneath the dark green, light green, gray, and white diagonal plunger gates have low to high values, respectively. The vertical barriers between the red and blue qubits are to be opened, and the light green diagonal plunger gates are to be far detuned to provide significantly lower on-site energy to overcome Coulomb repulsion between the red and blue qubits for the PSB readout. The same scheme can be used in the X-cycle, exchanging the role of the red and blue qubits.

Steps	1	2	3	4	5	6	7	8	9	10	11	12	13	14	Z cycle total
$\sqrt{\text{SWAP}}$ gates					$4d$			$4d$							$8d$
Z-rotations					$4d$			$4d$							$8d$
Shuttling			d			d	d			d		d		d	$5d$
Global rotations	1			1					1		1				4
Measurements													d		d

Table 4.2: Composite time step count per Step in terms of gate types for the line-by-line implementation of the surface code Z stabilizer measurement cycle (described as a 14-Step Protocol in Sec. 4.2.3). Z-rotations refers to shuttling-based single-qubit rotations around the z-axis. Table cells that are left empty signify zero entries. For the X stabilizer measurement cycle, one more global rotation and one less shuttling-based Z-rotation is needed. A similar table could be obtained for parallel operation, substituting $d = 1$ into the d -dependent entries of this Table.

Operation	Time steps per full cycle	Notation
$\sqrt{\text{SWAP}}$ gate	$16d$	τ_{sw}
Z-rotation	$15d$	τ_z
Shuttling	$10d$	τ_{sh}
Global rotation	9	τ_{gl}
Measurement	$2d$	τ_m

Table 4.3: Total number of composite time steps per operation for the full surface code stabilizer measurement cycle (subsequent X and Z stabilizer measurements) and the corresponding notations, assuming line-by-line operation. A similar table could be obtained for parallel operation, substituting $d = 1$ into the d -dependent entries of this Table.

that one Step is equivalent to at least one composite time step. At this level, one composite time step corresponds to a qubit shuttling step or a gate in the quantum circuits of Fig. 4.6 and 4.7. I use the adjective ‘composite’ here, because below I will further divide these composite time steps to *elementary time steps*.

Table 4.2 lists the composite time-step count of each Step of my Protocol in terms of the types of operations for the line-by-line implementation of the Z parity checks. As a result of the line-by-line implementation, the number of composite time steps needed for most of the operations is proportional to the code distance d . This is not true for global rotations, which are applied in parallel for qubits located in the same column [188], taking just a single composite time step. I get similar counts for the X stabilizer measurement cycle as that in Table 4.2, the only difference is I need one more global rotation, and one less shuttling-based z rotation for this protocol. Table 4.3 summarizes the total number of composite time steps for all gate types for a full surface code stabilizer measurement cycle. Additionally, I list the number of operations per qubit type (data/ancilla qubit) for both cycles in Table 4.4. Similar considerations hold for parallel operation as well, substituting $d = 1$ into the d -dependent entries of Table 4.2 and 4.3.

4.2.5 Dependence of the logical error on the code distance

In this section, I present the logical error probability estimation for a crossbar system based on Ref. [188], using the parameters from the previous section. In Ref. [100], surface code error correction was numerically simulated under realistic (circuit level) noise and the empirical formula, Eq. (11) of Ref. [100],

$$p_L \approx 0.03 \left(\frac{p_e}{8p_{\text{th}}} \right)^{\frac{d+1}{2}}, \quad (4.1)$$

	Data qubits			Z ancilla qubits			X ancilla qubits			Average
	Z-cycle	X-cycle	Total	Z-cycle	X-cycle	Total	Z-cycle	X-cycle	Total	
$\sqrt{\text{SWAP}}$ gate	2	2	4	8	0	8	0	8	8	6
Z-rotation	1	0	1	4	0	4	0	7	7	3.25
Shuttling	0	0	0	6	0	6	0	6	6	3
Global rotation	1	3	4	2	2	4	2	3	5	4.25
Measurement	0	0	0	1	0	1	0	1	1	0.5

Table 4.4: Number of operations per qubit type (data/ancilla qubit) for both cycles. Average values in the last column are obtained as the weighted average operation number for data qubits and ancilla qubits, using weight 2 for the data qubits. Qubits located at the boundary of the code might have lower gate counts.

providing reasonable agreement with the simulation data for any odd distance d (see Fig. 4 in Ref. [100]), where p_L is the logical error probability per surface code cycle, p_e is the per-cycle per-qubit physical error probability, and $p_{\text{th}} = 0.57\%$ is the per-step threshold error probability. I will make use of this formula to estimate the error scaling for my Protocol.

In my estimate, I consider two types of errors: decoherence-induced errors and operation-induced errors. Decoherence is present in any realistic quantum system that is subject to an environment [9]. Therefore, even the dynamics of idling qubits are governed by decoherence processes. These are often separated into two categories: relaxation and dephasing. Both mechanisms are characterized by a corresponding time scale, T_1 and T_2^* respectively. As argued in Chapter 3, for spin qubits, the dominant error mechanism is usually dephasing, which means that $T_2^* \ll T_1$ [23]. Thus, for my simple estimates, I neglect relaxation processes; I consider only qubit dephasing as the source of decoherence.

Assuming line-by-line operation (as discussed in Sec. 4.2.4), the total time of a full stabilizer measurement cycle using my Protocol is dependent on the code distance, and is calculated from Table 4.3 as follows:

$$\tau_{\text{total}}^{\text{line-by-line}}(d) = 16d\tau_{sw} + 15d\tau_z + 10d\tau_{sh} + 9\tau_{gl} + 2d\tau_m. \quad (4.2)$$

Here, I used the data and notation in Table 4.3, and weighted the duration of each operation with the corresponding composite time-step count. For parallel operation, the total time is independent of code distance:

$$\tau_{\text{total}}^{\text{parallel}} = 16\tau_{sw} + 15\tau_z + 10\tau_{sh} + 9\tau_{gl} + 2\tau_m. \quad (4.3)$$

Assuming an exponential decay of coherence, the decoherence-induced error probability is approximately given by the ratio of the total cycle time and the coherence time [188]:

$$P_{\text{decoh}}(d) = 1 - e^{-\tau_{\text{total}}(d)/(2T_2^*)} \approx \frac{\tau_{\text{total}}(d)}{2T_2^*}. \quad (4.4)$$

This is the standard way to introduce decoherence, however, note that Gaussian decay - relevant for e.g. $1/f$ noise - could result in significantly better estimates for the logical error probability since for time scales shorter than T_2^* it produces less decoherence. For an optimistic estimate, I use $T_2^* = 1$ s, which is the measured Hahn-echo coherence lifetime of donor spin qubits in ^{28}Si [209, 234]. I will also use a less optimistic value, $T_2^* = 10$ ms for comparison. Note that these coherence times - relying on future hardware advancements - are much longer compared to the value used in Sec. 3.5.

During quantum computation, single-qubit gates, two-qubit gates, shuttling, and measurements are also imperfect. To account for these imperfections I assign the same error probability,

Operation	Time duration	Error probability
$\sqrt{\text{SWAP}}$ gate	$\tau_{sw} = 20$ ns	$p_{sw} = 10^{-3}$
Z-rotation	$\tau_z = 100$ ns	$p_z = 10^{-3}$
Shuttling	$\tau_{sh} = 10$ ns	$p_{sh} = 10^{-3}$
Global rotation	$\tau_{gl} = 1000$ ns	$p_{gl} = 10^{-3}$
Measurement	$\tau_m = 100$ ns	$p_m = 10^{-3}$

Table 4.5: Operation times and error probabilities used for the estimation of the logical error probability p_L . All of the values are taken from Ref. [188].

10^{-3} , to each operation, as listed in Table 4.5. I also list the assumed time duration of the operations in Table 4.5.

Taking into account both decoherence-induced and operation-induced errors, I obtain the average error probability per quantum stabilizer measurement cycle (per physical qubit):

$$P_{\text{avg}}(d) = 6p_{sw} + 3.25p_z + 3p_{sh} + 4.25p_{gl} + 0.5p_m + P_{\text{decoh}}(d). \quad (4.5)$$

Here, I also weighted the operation-induced error probabilities with the per-cycle average number of the specific operations (as listed in the last column of Table 4.4). Qubits located at the code's boundary might have lower gate counts, which means that my estimate serves as an upper bound for the average error probability per cycle.

To evaluate the logical error probability, now let me use Eq. (4.1), replacing the per-cycle error probability p_e by the estimate $P_{\text{avg}}(d)$, yielding

$$p_L = 0.03 \left(\frac{P_{\text{avg}}(d)}{8p_{\text{th}}} \right)^{\frac{d+1}{2}}. \quad (4.6)$$

The thus obtained logical error probability is plotted in Fig. 4.10 as a function of code distance, both for parallel and line-by-line operation, for two different values of T_2^* , using $p_{\text{th}} = 0.57\%$ [100]. Panels (a) and (b) of Fig. 4.10 correspond to two different values of the measurement time τ_m .

In the case of parallel operation (blue solid and blue dashed lines in Fig. 4.10), the hardware constraints of the crossbar architecture do not imply any significant effect on the error suppression: the logical error probability goes below $p_L = 10^{-20}$ for code distance $d \approx 85$ for coherence times $T_2^* = 1$ s and $T_2^* = 10$ ms as well. Together with fault-tolerant logical operations, this level of precision is suitable for a fully functioning computer. Eq. (4.6) is often cast into the form

$$p_L = 0.03/\Lambda^{\frac{d+1}{2}} \quad (4.7)$$

as well, where $\Lambda = 8p_{\text{th}}/P_{\text{avg}}$ is the exponential error suppression factor which is just a constant in case of parallel operation. I extract the values $\Lambda \approx 2.7$ and 2.6 for coherence times $T_2^* = 1$ s and 10 ms, respectively. These values remain approximately the same regardless of using 100 ns or 1000 ns measurement time.

However, for line-by-line operation, due to the linear scaling of the operation time with the code distance, the logical error probability has a global minimum at a certain code distance d^* [188]. For coherence time $T_2^* = 10$ ms and measurement time $\tau_m = 100$ ns (red dashed line in Fig. 4.10(a)), the minimum achievable logical error probability is around $p_L = 10^{-12}$ at code distance $d^* = 117$. This becomes even less favorable when the measurement time τ_m is increased to 1000 ns (red dashed line in Fig. 4.10(b)), where the lowest feasible logical error probability is around $p_L = 10^{-7}$ at code distance $d^* = 63$.

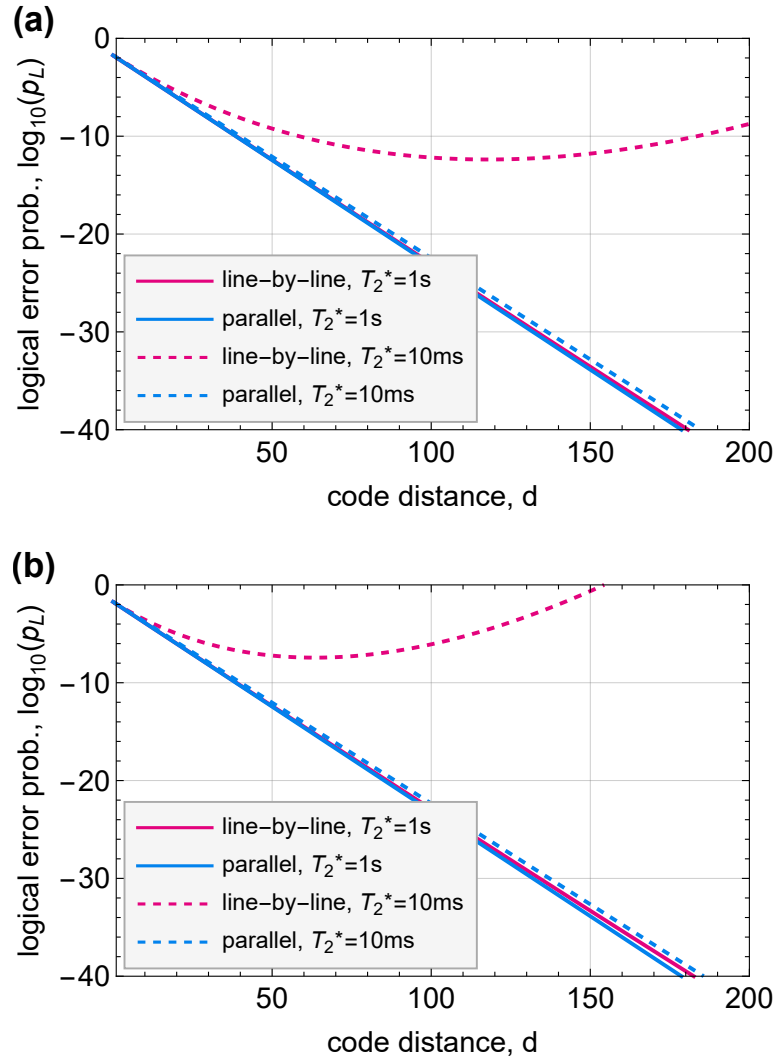


Figure 4.10: (a) Logarithm of the estimated logical error probabilities based on Eq. (4.6), as a function of code size, for measurement time $\tau_m = 100\text{ ns}$. Plotted for line-by-line and parallel operations, for coherence times $T_2^* = 1\text{ s}$ and 10 ms as well. Parallel operation implies error suppression factors $\Lambda \approx 2.7$ and 2.6 for coherence times $T_2^* = 1\text{ s}$ and 10 ms , respectively. (b) Same plot, but using $\tau_m = 1000\text{ ns}$ for the measurement time duration. The error suppression is approximately the same for the two different dephasing time values in case of parallel operation.

For the line-by-line implementation, I also compute the optimal code distance which I define as

$$d_{\text{opt}} = \arg \min_d \Gamma(d), \quad (4.8)$$

where $\Gamma(d)$ is the error rate,

$$\Gamma(d) = \begin{cases} 1/T_2^* & d = 1 \\ p_L/\tau_{\text{total}}^{\text{line-by-line}}(d) & d \geq 3. \end{cases} \quad (4.9)$$

The optimal code distance as a function of the dephasing time is illustrated in Fig. 4.11(a). Up until $T_2^* \approx 100 \mu\text{s}$ it is 1, meaning that scaling up the surface code leads to increased logical error. I consider the surface code quantum memory useful when the encoded logical qubit has less error than a single physical qubit. Therefore, in Eq. (4.8), I compare the achievable logical error probability per cycle time to the error of a single idling physical qubit. Fig. 4.11(b) also shows the optimal (minimized) error rates $\Gamma(d)$ as a function of the dephasing time. Furthermore, I also plot the optimal code distance and the optimized error rate as a function of both the dephasing time and the measurement time (from $\tau_m = 100 \text{ ns}$ to 2000 ns) in Fig. 4.11(c) and (d), respectively. Fig. 4.11(d) shows that above-millisecond coherence time is required to push the logical error rate per microsecond below 10^{-3} , which is the error of a single operation.

4.3 Pulse sequence for the stabilizer measurement cycles

In Sec. 4.2.3 I described a scheduling Protocol for the surface code stabilizer measurement cycle, although the question remains whether there is a practical pulse sequence that could realize it. In this section, I argue that the answer to this question is positive, furthermore, I construct a specific pulse sequence that is suitable for my Protocol. Following Fig. 4.2, in Sec. 4.3.1, first I describe this pulse sequence in terms of abstract gate voltage values and abstract ESR pulses. Based on this description, in Sec. 4.3.2, I also provide a verification algorithm for the qubit shuttling steps included in my Protocol. I assign physical pulses to the abstract ones in Sec. 4.3.3, establishing the final control stack layer of implementing the surface code with the crossbar architecture (Fig. 4.2). Finally, in Sec. 4.3.4, I also estimate the idle qubit errors occurring during my implementation of the surface code stabilizer measurement cycle due to the crosstalk effects.

4.3.1 Abstract pulse sequence

The Protocol described in Sec. 4.2.3 consists of global single-qubit gates, qubit shuttling steps, shuttling-based single-qubit phase gates, two-qubit $\sqrt{\text{SWAP}}$ gates, and measurements. Coherent shuttling of a single qubit is a simple procedure, however, for parallel operation, it is a non-trivial problem to perform multiple shuttlings simultaneously, due to the limited control in the crossbar architecture. This is also true for the $\sqrt{\text{SWAP}}$ gates.

Assuming that throughout the quantum-dot array, the Coulomb energy and the orbital level spacing are much larger than the on-site energy differences, I propose that it is sufficient to use 4 different plunger gate voltage values to carry out my Protocol with parallel operation. (In fact, a fifth value is needed for the spin-to-charge conversion in Step 13 of my Protocol.) Furthermore, to describe the pulse sequence it is enough to prescribe the gate voltages on 4 consecutive diagonal plunger gates, and then I have a pattern that is periodically repeating itself.

At this level, I further divide composite time steps (used in Sec. 4.2.4) into *elementary time steps* to resolve the pulsing of the plunger and barrier gates. In Table 4.6, I outline the first 18 elementary time steps of the abstract gate voltage and abstract ESR pulse sequence corresponding to the surface code Z-cycle based on my Protocol. Each column of this table corresponds to one

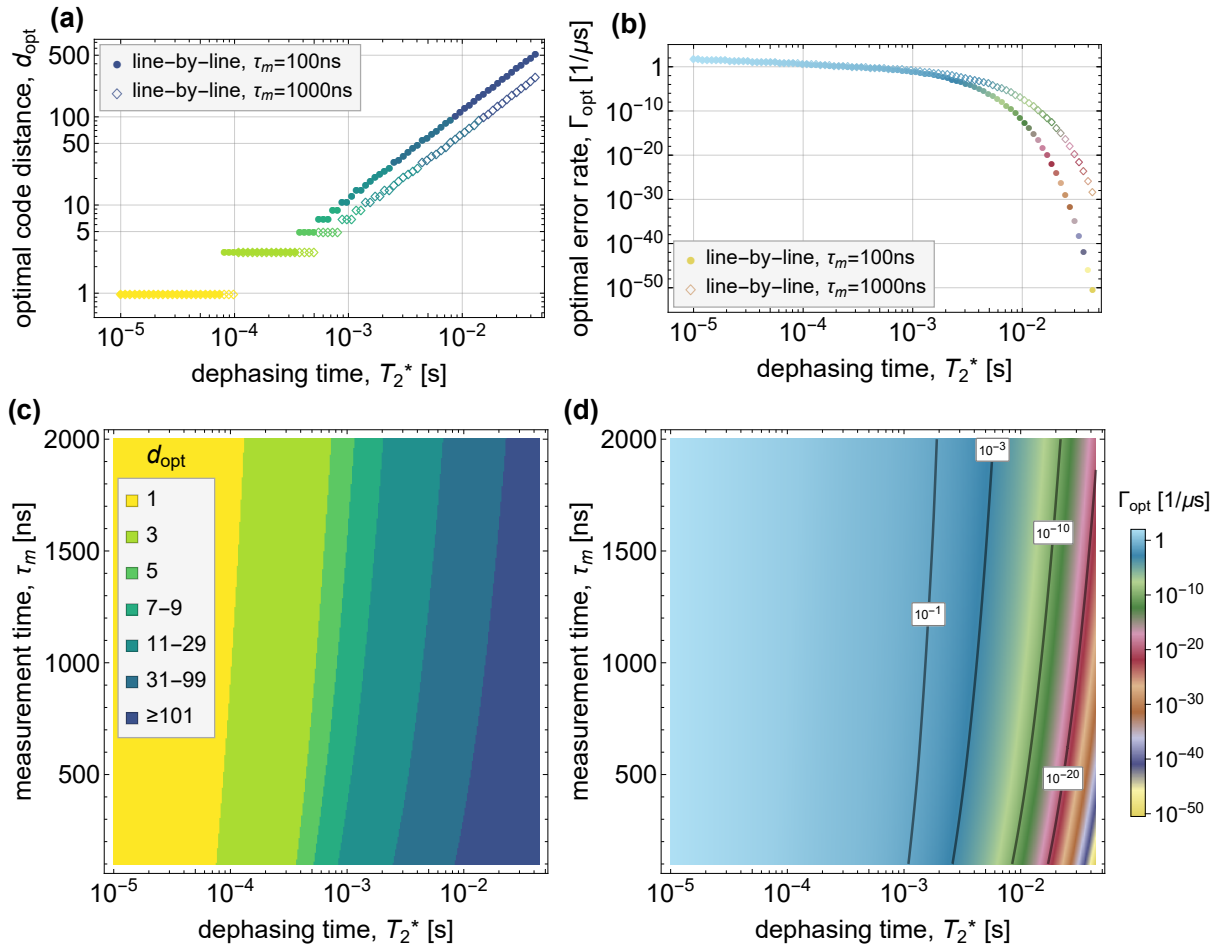


Figure 4.11: (a) Optimal code distance of Eq. (4.8), for line-by-line operation as a function of the dephasing time T_2^* , for measurement time durations $\tau_m = 100\text{ns}$ and 1000ns . (b) The corresponding optimized error rates $\Gamma_{\text{opt}} = \Gamma(d_{\text{opt}})$ in units of $(\mu\text{s})^{-1}$. (c) Optimal code distance shown as a function of both dephasing time and measurement time. (d) The optimized error rate Γ_{opt} shown as a function of both dephasing time and measurement time.

Components	Specification	1	2	3	4	5	6	7	8	9	10	11	12	13	14	15	16	17	18
plunger gates	0	1	1	1	c	3	3	3	3	3	3	3	c	4	c	3	3	3	3
	1	4	4	4	c	2	2	c	3	3	3	c	2	2	2	c	3	3	3
	2	1	1	1	1	1	1	1	1	1	1	1	1	1	1	1	1	1	1
	3	4	4	4	4	4	4	4	4	4	4	4	4	4	4	4	4	4	4
barrier gates	even, horizontal	1	1	1	1	1	1	1	c	0	c	1	1	1	1	1	c	0	c
	odd, horizontal	1	1	1	1	1	1	1	1	1	1	1	1	1	1	1	1	1	1
	even, vertical	1	1	c	0	c	1	1	1	1	1	1	c	0	c	1	1	1	1
	odd, vertical	1	1	1	1	1	1	1	1	1	1	1	1	1	1	1	1	1	1
ESR	ω_o	0	0	0	0	0	0	0	0	0	0	0	0	0	0	0	0	0	0
	ω_e	0	1	0	0	0	1	0	0	0	0	0	0	0	0	0	0	0	0

Table 4.6: First 18 elementary time steps of the (abstract) gate voltage and ESR pulse sequence realizing the surface code Z-cycle. For the numbering of the plunger gates and the barriers, I use the same convention as in Fig. 4.1 and Fig. 4.3(b). Plunger gate voltages are periodic before and after the four I listed in this table. Here, I associate integers with the plunger voltage values. A higher integer value corresponds to a higher gate voltage (on-site potential). For the barrier gates, there are On/Off declarations (where On refers to high tunnel barrier, no tunneling) corresponding to 1 or 0, respectively. The value "c" refers to that the gate voltage is changing. For the ESR pulses, 0 means no pulse and 1 means a Hadamard gate. The full sequence (111 elementary time steps) together with a visual representation is provided at the Zenodo repository [227], see ZcyclePulseSequence.xlsx and ZcycleMovie.pdf correspondingly.

elementary time step and contains a value (1, 2, 3, or 4) for the 4 consecutive diagonal plunger gates that is proportional to the value of the on-site energies, On/Off declarations for the barriers, and the ESR field as well. For the numbering of the plunger gates and the barriers, I use the same convention as in Fig. 4.3(b).

Starting from the idle configuration (elementary time step 1), elementary time step 2 is the Hadamard gate applied to the ancilla qubits, and elementary time steps 3-5 correspond to qubit shuttling to reach the rightward triangle configuration. Elementary time step 6 corresponds to Step 4 in my scheduling Protocol, elementary time step 7 is a plunger reset, elementary time steps 8-10 correspond to the first $\sqrt{\text{SWAP}}$ of Step 5, elementary time steps 11-15 realize a shuttling based Z gate, and elementary time steps 16-18 correspond to the second $\sqrt{\text{SWAP}}$ gate of Step 5. Most of the Steps in my Protocol consist of more than one elementary time step, corresponding to several columns in Table 4.6, consequently.

At the Zenodo repository [227], I provide the full abstract gate-voltage pulse sequence for both the Z and X stabilizer measurement cycles implemented with parallel operation, in the form of two Tables (see auxiliary files ZcyclePulseSequence.xlsx and XcyclePulseSequence.xlsx, respectively).

4.3.2 Verification of the shuttling protocol

In this section, I summarize how I verify the shuttling protocol. Verification means two things: ensuring that the (abstract) gate voltage pulse sequence meets the operational constraints of the crossbar architecture, and checking whether the given pulse sequence realizes the desired movements between the different spatial configurations of the electrons. Therefore, I use the following definitions and set the requirements listed below:

1. Assume that each plunger gate voltage at each step of the pulse sequence takes one of the

- four different values: 1, 2, 3, 4. This abstract value represents the on-site energy controlled by the plunger gate, with 1 (4) corresponding to the lowest (highest) on-site energy.
2. An *electron configuration* (\mathbf{E}) is the collection of electron positions in the lattice. Double occupancy of a single site is forbidden for shuttling.
 3. A *plunger configuration* (\mathbf{P}) is a vector of plunger values.
 4. A *configuration* $\mathbf{C} = (\mathbf{E}, \mathbf{P})$ is an ordered pair of an electron configuration and a plunger configuration.
 5. A plunger reset (also denoted by \mathbf{P}) describes the change of the plunger values. Formally, it is simply the plunger configuration after the change. If this is combined with barrier activation (see below), then it results in a change in the electron configuration. If it is not combined with barrier activation, then it does not change the electron configuration.
 6. A *shift* (\mathbf{S}) describes the movement of electrons in the array in response to the activation of a barrier and a plunger reset. Formally, it is an ordered pair $\mathbf{S} = (\beta, \mathbf{P})$ where β is the collection of barrier indices (of those barriers that are activated), and \mathbf{P} is a plunger reset. Activation of the barriers means that first the barriers are lowered, then the plunger reset is applied, and then the barriers are raised back.
 7. I aim to avoid unwanted, and non-adiabatic tunneling processes, hence I constrain which shifts can be performed on which configurations. This is specified in the following:
 - (a) Each shift must contain the activation of either horizontal or vertical barriers only.
 - (b) It is not allowed to activate the barriers on both sides of a dot in the same shift.
 8. A shift $\mathbf{S} = (\beta, \mathbf{P})$ is *compatible* with a configuration $\mathbf{C}_0 = (\mathbf{E}_0, \mathbf{P}_0)$, if the following conditions are satisfied for all $b \in \beta$:
 - (a) In the electron configuration \mathbf{E}_0 , all neighboring dot pairs of barrier b contains at most one electron.
 - (b) For all electrons in the neighboring dot pairs of barrier b , one side of the barrier has lower on-site energy than the other (also implying that the pre-shift plunger values specified in \mathbf{P}_0 are different), and the electron resides on the side of that barrier with the lower on-site energy.
 - (c) For all dot pairs neighboring barrier b , the post-shift plunger values specified in \mathbf{P} are also different on the two dots.
 9. A shift is an operation that can act on configurations that are compatible with it. In such a case, the result (in other words, the *action*) of the shift $\mathbf{S} = (\beta, \mathbf{P})$ on configuration $\mathbf{C}_0 = (\mathbf{E}_0, \mathbf{P}_0)$ is $\mathbf{C} = (\mathbf{E}, \mathbf{P})$, where \mathbf{E} contains the new positions of the electrons. Only the positions of those electrons can change that initially reside in one of the dot pairs neighboring the barriers listed in β . Out of those electrons, the ones whose on-site energy remains lower after the shift will not move. Those electrons whose on-site energy is higher after the shift will move to the other dot of their dot pair.
 10. A *shuttling protocol* is specified as an initial configuration, and a sequence of shifts and plunger resets (that are shifts without barrier activation), such that each shift is compatible with the configuration preceding it. Without the loss of generality, I can assume that bare plunger resets can be contracted, i.e., between two subsequent shifts there is at most one

bare plunger reset. The result of a protocol is the final configuration \mathbf{C}_N , which can be expressed as the sequence of actions on the initial configuration:

$$\mathbf{C}_N = \mathbf{S}_{(N-1) \rightarrow N} \dots \mathbf{S}_{1 \rightarrow 2} \mathbf{S}_{0 \rightarrow 1} \mathbf{C}_0, \quad (4.10)$$

where N is the number of shifts in the shuttling protocol.

Using this language, verification of a shuttling protocol is equivalent to checking whether all subsequent shifts are compatible with their prior configuration and whether their action indeed provides the desired configuration (for all of the intermediate steps as well). If all of these requirements are satisfied, then the corresponding shuttling protocol is valid.

I implemented the above requirements as a verification algorithm in Python and tested the validity of the qubit shuttling steps of my Protocol (described in Sec. 4.2.3) by checking all the requirements for the 4×4 unit cell of the grid (shown in Fig. 4.8), using periodic boundary conditions. My code is available at the Zenodo repository [235]. It takes a list of configurations $(\mathbf{C}_0, \mathbf{C}_1, \mathbf{C}_2, \dots, \mathbf{C}_N)$ and shifts $(\mathbf{S}_{0 \rightarrow 1}, \mathbf{S}_{1 \rightarrow 2}, \dots, \mathbf{S}_{(N-1) \rightarrow N})$ as input. As output, it returns boolean values depending on whether the performed shifts were compatible with the corresponding configurations and whether they resulted in the next configuration in the list. Since all shifts corresponding to shuttling steps (Step 3, 6, 7, 10, 12, and 14) in my Protocol were found to be compatible with their previous configuration and moved the grid to the subsequent configuration, I conclude that the relevant parts of the (abstract) gate voltage pulse sequence are valid. I note that one can also use my verification algorithm to find shifts connecting two arbitrary configurations of the crossbar array by brute force checking all possible cases.

4.3.3 Physical pulse sequence

In this section, I describe a physical implementation of the abstract gate voltage and ESR pulse sequence described in section 4.3.1.

As I mentioned in Sec. 4.3.1, it is sufficient to use 4 different plunger gate voltage values to carry out my Protocol. These plunger gate voltages control the quantum-dot on-site energies, to be used in the Hamiltonian introduced in Sec. 4.3.4. Let me denote the quantum dot on-site energy values by u_1, u_2, u_3 , and u_4 , in increasing order. In what follows, I will change an on-site energy from u_i to u_j in time T using the following smooth function:

$$\varepsilon(u_i, u_j, t) = u_i + (u_j - u_i) \sin^2 \left(\frac{\pi t}{2T} \right). \quad (4.11)$$

Similarly, I will tune a tunnel barrier separating neighboring quantum dots according to

$$t_0(t) = t_{0,\max} \sin^2 \left(\frac{\pi t}{T} \right), \quad (4.12)$$

between the On ($t_0(0) = t_0(T) = 0$) and Off ($t_0(T/2) = t_{0,\max}$) declarations. I use Eq. (4.11) to model the physical pulses corresponding to plunger resets, and Eq. (4.12) to model barrier activation during the shuttling protocol (see Sec. 4.3.2).

For shuttling-based z rotations (see Step 5 in the Protocol described in Sec. 4.2.3), I tune the plunger gate voltage of the target qubit (u_t) to the same level as the neighboring site (u_n) and I also tune it back; these two steps together take time T_z ; in the same time window, I also activate the barrier:

$$\varepsilon_z(u_t, u_n, t) = u_t + (u_n - u_t) \sin^2 \left(\frac{\pi t}{T_z} \right), \quad (4.13a)$$

$$t_0(t) = t_{0,\max} \sin^2 \left(\frac{\pi t}{T_z} \right). \quad (4.13b)$$

The Hadamard gate can be expressed as a $\pi/2$ rotation around the y axis, followed by a π rotation around the x axis,

$$H = X\sqrt{Y}. \quad (4.14)$$

Similarly, the S gate can be decomposed as

$$S = \sqrt{X}\sqrt{Y}\sqrt{X}^\dagger. \quad (4.15)$$

These elementary single-qubit rotations are executed by an ESR drive pulse

$$B_x(t) = B_{ac} \sin(\omega_{ac}t + \varphi), \quad (4.16)$$

where B_{ac} is the amplitude, ω_{ac} is the frequency (to be matched with ω_e or ω_o , see Fig. 4.1) and φ is the phase of the driving field. Specifically, a \sqrt{Y} gate is obtained using $\varphi = \pi$ and pulse duration $\pi/(2\Omega)$, where Ω is the qubit Rabi frequency which is proportional to the drive strength $\Omega = \gamma B_{ac}/2$, where γ is the electron gyromagnetic ratio. Similarly, a \sqrt{X} gate is obtained using $\varphi = \pi/2$ and the same pulse duration. Doubled pulse durations provide the Y and X gates, respectively. These gates are interpreted in the frame which is rotating with the qubit's Larmor frequency (ω_e or ω_o) around the z axis.

During $\sqrt{\text{SWAP}}$ gates, the two qubits involved are located at the same column, which means the Zeeman splitting is the same for both. In the crossbar architecture, these gates can be performed with a conventional exchange pulse [188, 209], i.e., by lowering the barrier separating the two electrons such that the on-site energy of the two dots is kept equal.

Finally, I use the standard two-qubit double quantum dot Hamiltonian to describe the PSB readout [236], assuming that the reference qubit is in $|\uparrow\rangle$ state occupying a quantum dot in an even column (with Larmor frequency ω_e). The qubit to be measured (e.g. the red qubits in Fig. 4.9) is located on the neighboring site, in an odd column (with Larmor frequency ω_o), and for concreteness, I assume that $\omega_o < \omega_e$. During the readout, the on-site energy of the reference qubit is lowered so that the detuning exceeds the Coulomb repulsion (I denote the corresponding value of plunger gate voltage by "R" in the abstract gate pulse sequence, see auxiliary files ZcyclePulseSequence.xlsx and XcyclePulseSequence.xlsx at the Zenodo repository [227]), and the barrier between the qubits is opened simultaneously. Consequently, the anti-parallel spin configuration is converted to a single-site singlet; in contrast, the parallel spin configuration is blockaded and the two electrons remain separated on the two sites. Finally, this charge difference is measured by a charge sensor and hence is used to infer the state state of the qubit.

4.3.4 Idle-qubit errors due to limited control

Due to the shared-control gate layout, crosstalk occurs: when an operation (e.g., shuttling, gate, readout) targets a subset of the qubits, then the remaining qubits, which are nominally idling, are also affected by the control fields, hence undergo undesired dynamics leading to errors. I refer to this effect as crosstalk. Note that my Protocol avoids opening a barrier between two idle qubits located at neighboring sites (see Sec. 4.3.2), thus two-qubit crosstalk errors are absent.

In this section, I describe the crosstalk-induced, unwanted idle qubit rotations using the adiabatic approximation and an effective model. I also provide an estimate for the rotation angles using experimentally relevant parameters.

I aim to characterize idle qubit errors during my Protocol, realized by the physical pulse sequence described in Sec. 4.3.3. Note that in my Protocol there is no such step or configuration when horizontal and vertical barriers are open simultaneously, meaning that horizontal and vertical movement of the qubits is completely separated during the stabilizer measurement cycle. Whenever a vertical barrier is open, horizontal, tunnel-coupled double quantum dots are formed from the two columns neighboring that vertical barrier.

To model this scenario (e.g. a coherent shuttling) I use a minimal model: a single electron in a double quantum dot with Hamiltonian

$$\hat{\mathcal{H}}_{\text{DQD}} = \hat{\mathcal{H}}_{\text{os}} + \hat{\mathcal{H}}_{\text{t}} + \hat{\mathcal{H}}_{\text{Z}}, \quad (4.17)$$

$$\hat{\mathcal{H}}_{\text{os}} = \frac{\epsilon(t)}{2} \hat{\tau}_z, \quad (4.18)$$

$$\hat{\mathcal{H}}_{\text{t}} = t_0(t) \hat{\tau}_x, \quad (4.19)$$

$$\hat{\mathcal{H}}_{\text{Z}} = \frac{1}{2} \hbar \gamma (B_{\text{L}} \hat{\sigma}_z^{\text{L}} + B_{\text{R}} \hat{\sigma}_z^{\text{R}}), \quad (4.20)$$

where $\hat{\mathcal{H}}_{\text{os}}$, $\hat{\mathcal{H}}_{\text{t}}$, $\hat{\mathcal{H}}_{\text{Z}}$ are on-site, tunneling, and Zeeman terms, respectively. Here $\hat{\tau}_x$ and $\hat{\tau}_z$ are Pauli matrices acting on the orbital degree of freedom in the left-right basis, e.g., $\hat{\tau}_z = |L\rangle\langle L| - |R\rangle\langle R|$, and $\hat{\sigma}_z$ is the Pauli-Z matrix acting on the electron spin. Furthermore, ϵ denotes the on-site energy detuning between the two dots, and the (spin-conserving) tunneling amplitude is denoted by t_0 . In the Zeeman term, γ is the electron gyromagnetic ratio, and $B_{\text{L,R}}$ is the external magnetic field in the left or right dot.

As discussed in Sec. 4.3.3, the Hamiltonian in Eq. (4.17), becomes time-dependent during my Protocol, through the tunneling amplitude and the on-site energy detuning. However, the tunneling term is spin-conserving, which means that there is no mixing between the spin-up and the spin-down sectors during the dynamics, thus the Hamiltonian has a block-diagonal structure: it consists of 2×2 blocks for each spin species. Therefore the exact (time-dependent) energy eigenvalues can be obtained. I also assume that the time evolution of the idle qubits is adiabatic, i.e. they remain in their instantaneous energy eigenstate.

Let me consider an idle qubit initially located in the left dot ($t_0(0) = 0$, $\epsilon(0) < 0$) which is assumed to be in an even column, with Larmor frequency $\omega_e = \gamma B_{\text{L}}$, and the right dot is in an odd column with Larmor frequency $\omega_o = \gamma B_{\text{R}}$, see Fig. 4.1. For my purposes, it is sufficient to consider the case when the detuning is large compared to the Zeeman splitting and the tunneling amplitude, $\hbar\omega_{e/o}$, $t_0 \ll |\epsilon|$, and to focus on the lowest two eigenstates in energy, that is, the bonding spin-up state and the bonding spin-down state. I expand the exact energy eigenvalues up to first order in magnetic field and second order in tunnel coupling. Thus, I obtain a 2×2 effective Hamiltonian describing the idle qubit dynamics:

$$\hat{\mathcal{H}}_{\text{eff}} \approx \frac{1}{2} \hbar \omega_e \hat{\sigma}_z \left(1 - \frac{t_0^2}{\epsilon^2} \right) + \frac{1}{2} \hbar \omega_o \hat{\sigma}_z \frac{t_0^2}{\epsilon^2}, \quad (4.21)$$

where I omitted the time dependence of t_0 and ϵ for brevity. The error mechanism described by the effective Hamiltonian Eq. (4.21) is that the idling qubit leaks into the neighboring dot upon barrier activation, which causes unwanted qubit rotation around z (i.e., a phase gate), since the Larmor frequencies of the two dots are different.

The idle qubit located in the even column is static in a rotating frame described by

$$W(t) = e^{\frac{i}{2} \omega_e \hat{\sigma}_z t}, \quad (4.22)$$

which transforms the Hamiltonian as

$$\hat{\mathcal{H}}'_{\text{eff}} = W(t) \hat{\mathcal{H}}_{\text{eff}} W^\dagger(t) - \frac{\hbar}{i} \dot{W}(t) W^\dagger(t) = -\frac{t_0^2}{\epsilon^2} \hbar \omega' \hat{\sigma}_z, \quad (4.23)$$

where $\omega' = (\omega_e - \omega_o)/2$. The time-evolution operator in the rotating frame, assuming adiabatic dynamics, can be written as

$$\hat{\mathcal{U}}'_{\text{idle}} = e^{i \Delta \phi_{\text{idle}} \hat{\sigma}_z / 2}, \quad (4.24)$$

where the idle qubit rotation angle is

$$\Delta \phi_{\text{idle}} = -2\omega' \int_0^T \frac{t_0^2(t)}{\epsilon^2(t)} dt, \quad (4.25)$$

where the on-site energy detuning between the left and the right dot is $\epsilon(t) = \varepsilon_L(t) - \varepsilon_R(t)$. When the time dependence of the on-site energies and the tunneling amplitude are described by Eqs. (4.11) and (4.12), the integral can be carried out exactly. Thus, crosstalk during shuttling results in idle qubit rotation angle

$$\Delta\phi_{\text{idle}}^{(\text{shuttle})} = \frac{12 \left(A^2 - 4A \left(\sqrt{\epsilon_0(\epsilon_0 - A)} + 2\epsilon_0 \right) + 8\epsilon_0 \left(\sqrt{\epsilon_0(\epsilon_0 - A)} + \epsilon_0 \right) \right)}{A^4} t_{0,\text{max}}^2 \omega' T, \quad (4.26)$$

where $\epsilon_0 = u_{L,i} - u_{R,i}$ is the initial detuning between the dots which is assumed to have a large negative value ($\epsilon_0 \ll 0$), and

$$A = u_{L,j} + u_{R,j} - u_{L,i} - u_{R,i} \quad (4.27)$$

is the detuning amplitude, which has a smaller magnitude, $|A| < |\epsilon_0|$, so that the overall detuning remains negative throughout the protocol.

Similarly, for shuttling-based z rotations, using the gate voltage and tunnel barrier pulses of Eq. (4.13), I obtain

$$\Delta\phi_{\text{idle}}^{(z\text{-rot.})} = \frac{\left(3A'\epsilon'_0 - 2\epsilon'_0 \left(\sqrt{\epsilon'_0(\epsilon'_0 - A')} + \epsilon'_0 \right) + 2A' \sqrt{\epsilon'_0(\epsilon'_0 - A')} \right)}{(A')^2 \sqrt{-\epsilon'_0} (A' - \epsilon'_0)^{3/2}} t_{0,\text{max}}^2 \omega' T_z, \quad (4.28)$$

where I use the notation $\epsilon'_0 = u_{L,t} - u_{R,t} < 0$ and

$$A' = u_{L,n} + u_{R,n} - u_{L,t} - u_{R,t}. \quad (4.29)$$

Note that in the special case, when the two on-site energies ε_L and ε_R are tuned such that the detuning $\epsilon(t)$ is constant in time ($A = 0$), Eq. (4.26) yields a simplified form,

$$\Delta\phi_{\text{idle}} = \frac{3t_{0,\text{max}}^2}{4\epsilon_0^2} \omega' T. \quad (4.30)$$

Eq. (4.28) also yields a similar form when $A' = 0$.

Idling data qubits during the PSB readout (depicted in Fig. 4.9, where all black qubits are idling) can also suffer such unwanted rotations. I calculate these rotation angles similarly, using the effective Hamiltonian, Eq. (4.23). During the readout, the vertical barrier between the ancilla qubits is lowered and the on-site energy of the reference qubit (blue qubits in Fig. 4.9) is lowered such that the attained detuning ϵ_{max} is large enough to overcome the on-site Coulomb repulsion. However, for the readout it is sufficient to activate the barrier only when the on-site energy detuning is approaching the value of the on-site Coulomb repulsion U , reducing the unwanted rotation angles significantly. Therefore, preceded by an abrupt plunger reset, I simulate the spin-to-charge conversion as per Eqs. (4.11) and (4.12), with reference qubit on-site energies $u_i = -2100 \mu\text{eV}$, $u_j = -2500 \mu\text{eV}$, and time duration $T = 25 \text{ ns}$. Meanwhile, the on-site energy of the measured qubit (red qubits in Fig. 4.9), is constant at $u_1 = -800 \mu\text{eV}$.

From the rotation angles, I estimate idle qubit errors as the maximal infidelity with the initial state. In the case of any shuttling-based operation (when there is barrier activation), idle qubits can suffer z rotations as crosstalk errors. Rotations around the z axis are the most harmful for states in an equal superposition of computational basis states, such as

$$|\tilde{\psi}_0\rangle = \frac{1}{\sqrt{2}} (|\tilde{0}\rangle + |\tilde{1}\rangle), \quad (4.31)$$

where the tilde is used to indicate that these states are in the rotating frame. Thus I obtain the idle error as

$$1 - \left| \langle \tilde{\psi}_0 | \hat{\mathcal{U}}_{\text{idle}} | \tilde{\psi}_0 \rangle \right|^2 = \sin^2(\Delta\phi_{\text{idle}}/2). \quad (4.32)$$

Note that using the average infidelity formula, Eq. (4.34), I get a very similar result,

$$1 - F = \frac{2}{3} \sin^2(\Delta\phi_{\text{idle}}/2), \quad (4.33)$$

that would provide a slightly more optimistic estimate.

Idle qubits also suffer errors due to off-resonant drive during the ESR pulses. Such crosstalk errors occur e.g. when qubits located at the odd columns are driven with ESR pulse outlined in Eq. (4.16), using $\omega_{\text{ac}} = \omega_o$, meanwhile, qubits located in the even columns are idling (see Steps 2, 4 and 9 in my Protocol). In this case, idle qubits are subjected to unwanted partial Rabi oscillations. I estimate the average error they suffer using the infidelity formula

$$1 - F = \frac{2}{3} - \frac{1}{6} \left| \text{Tr} \left(\hat{U}_0^\dagger \hat{U} \right) \right|^2, \quad (4.34)$$

where F denotes the average fidelity (averaged over all possible idle qubit initial state on the Bloch sphere) [237], \hat{U}_0 is the 2×2 identity matrix, and \hat{U} is the time-evolution operator in the idle qubit frame [defined in Eq. (4.22)]. Starting from the lab frame Hamiltonian

$$\hat{\mathcal{H}}_e = \frac{1}{2} \hbar \omega_e \hat{\sigma}_z + \Omega \sin(\omega_o t + \varphi) \hat{\sigma}_x, \quad (4.35)$$

I calculate the time-evolution operator employing the rotating wave approximation in the drive frame [defined by substituting ω_e with ω_o in Eq. (4.22)], and then transforming that result to the qubit frame. For large detuning $\omega' \gg \Omega$, Eq. (4.34) yields

$$1 - F \lesssim \alpha \frac{\Omega^2}{(\omega')^2}, \quad (4.36)$$

where α is a constant, e.g. for an off-resonant X gate ($\varphi = \pi/2$, and $t = \pi/\Omega$) it is $\alpha = (64 + \pi^2)/384$. For an off-resonant Hadamard gate composed of two consecutive single-qubit rotations [see Eq. (4.14)], the idle qubit error is roughly doubled, $2\alpha\Omega^2/(\omega')^2$.

Table 4.7 provides an exhaustive list of unwanted idle-qubit rotations together with the estimated errors based on the arguments discussed here, using a realistic set of parameters (Table 4.8). Since none of the estimated idle qubit errors exceeds the per-step threshold error probability of the surface code, $p_{\text{th}} = 0.57\%$ [100], I conclude that the logical qubit of a surface code implementation with these parameters will have a longer lifetime than the physical qubits used as its constituents.

I also note that due to the control constraints of the crossbar architecture, the spatial distribution of idle qubit errors has a periodic structure. This implies inhomogeneous (but spatially periodic) coherent noise on the surface code logical state which in principle could have an enhanced effect compared to random Pauli errors. However, as explained in Chapter 3, recent works showed that for the surface code, coherent single-qubit rotations do not change the error correction threshold significantly [115, 117, 238], supporting the validity of my simple error estimates.

A refined version of the estimated error scaling described in Sec. 4.2.5 can be obtained by using the simulated shuttling-based Z gate time duration, $\tau'_z \approx 10$ ns (with simulation parameters listed in Table 4.8) and including the idle qubit errors in the average error probability, Eq. (4.5). Based on Table 4.7, I estimate the average idle qubit error for the Z cycle as $p_{\text{idle}} \approx 6.4 \times 10^{-4}$ and the average number of imperfect idle qubit operations for a full cycle to be 8.5 per qubit. The latter is obtained as the sum of the number of idle qubit errors in each step, divided by the total number of qubits in the unit cell (see Fig. 4.8).

Assuming that in the X cycle, the average idle qubit error is approximately the same, this gives rise to an additional term, $17p_{\text{idle}}$ in Eq. (4.5), which is a dominant contribution to the

Operation	Corresponding steps	Idle qubits	Formula	Estimated error
shuttling	Steps 3, 6, 7, 10, 12, 14	D1, D2, D3, D4	Eq. (4.26)	1.8×10^{-4}
	Steps 3, 10	B1, B2	Eq. (4.30)	2.7×10^{-5}
shuttling-based Z gates	Steps 5, 8	D1, D2, D3, D4	Eq. (4.30)	2.3×10^{-3}
		A1, A2	Eq. (4.28)	2.5×10^{-3}
shuttling-based S^\dagger gates	Steps 5, 8	D1, D4	Eq. (4.30)	7.3×10^{-5}
		D2, D3	Eq. (4.28)	7.1×10^{-4}
PSB readout	Step 13	D1, D4	Eq. (4.30)	2.0×10^{-3}
		D2, D3	Eq. (4.26)	5.7×10^{-6}
Hadamard gate	Step 2	D1, D2, D3, D4	Eq. (4.36)	2.2×10^{-4}
	Step 4, 9	D1, D2, D3, D4 A1, A2	Eq. (4.36)	2.2×10^{-4}

Table 4.7: List of idle qubit errors during the surface code Z-cycle. Qubit notations are as per Fig. 4.8. I used the parameters listed in Table 4.8 for the error estimation. From the rotation angles expressed by the equations in column "Formula", I estimate the errors using the infidelity, Eq. (4.32). My estimates provide approximate upper bounds for the actual idle qubit errors in each step. Note that ancilla qubits B1 and B2 are not affected between Steps 4 and 9 (and after Step 11), since after two (or four) subsequent Hadamard gates they are ideally in a computational basis state. The average (weighted with the number of steps and the number of qubits) estimated idle qubit error is $p_{\text{idle}} \approx 6.4 \times 10^{-4}$ and the average number of imperfect idle qubit operations for a full cycle is 17 per qubit.

Parameter	Notation	Value
Maximal tunneling amplitude	$t_{0,\text{max}}$	25 μeV
Larmor frequency difference	$\omega' = (\omega_e - \omega_o)/2$	1 $\mu\text{eV}/\hbar$
On-site energy level 1	u_1	-800 μeV
On-site energy level 2	u_2	-533.33 μeV
On-site energy level 3	u_3	-266.66 μeV
On-site energy level 4	u_4	0 μeV
On-site repulsion	U	1500 μeV
On-site energy detuning for PSB readout	ϵ_{max}	1700 μeV
Shuttling time	τ_{sh}	9.35 ns
Time duration of shuttling-based Z gate	-	9.62 ns
Time duration of shuttling-based S^\dagger gate	-	4.82 ns
PSB spin-to-charge conversion time	-	25 ns
ESR drive amplitude	B_{ac}	0.35 mT
Qubit Rabi frequency	Ω	0.02 $\mu\text{eV}/\hbar$

Table 4.8: List of parameters used for the simulation of physical pulses based on Sec. 4.3.3 and 4.3.4. Parameters are chosen to ensure that the target qubit transfer during shuttling is adiabatic. Time durations of shuttling, the Z and the S^\dagger gates are obtained by numerical optimization of the corresponding target qubit fidelity while other parameters were fixed.

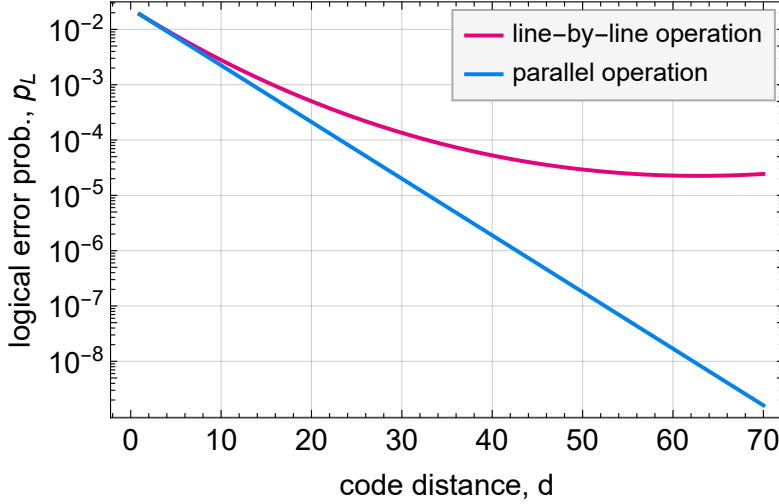


Figure 4.12: Refined estimate of the logical error probabilities versus the code distance, based on Eq. (4.6), with a shorter Z-rotation time ($\tau'_z \approx 10$ ns), and accounting for idle qubit errors as well. Plotted for line-by-line and parallel operations, using coherence time $T_2^* = 10$ ms and measurement time $\tau_m = 1000$ ns. Parallel operation provides better logical performance (with exponential error suppression factor $\Lambda \approx 1.6$), meanwhile, logical error suppression also remains feasible for line-by-line operation in this case, for moderate code sizes, up to $d_{\text{opt}} = 63$, and with the lowest attainable logical error probability being $p_L \approx 2.3 \times 10^{-5}$.

average error probability. Taking into account this additional error term and substituting τ_z with τ'_z in Eqs. (4.2)-(4.3), I obtain a refined estimate for the logical error probabilities, shown in Fig 4.12. These results show that in the presence of idle qubit errors, parallel operation has decreased exponential error suppression, $\Lambda \approx 1.6$. Since the idle qubit errors are small, logical error suppression remains feasible for the line-by-line implementation as well, up to moderate code sizes, $d_{\text{opt}} = 63$, with the lowest attainable logical error probability being $p_L \approx 2.3 \times 10^{-5}$.

4.4 Overview of auxiliary files

Finally, I give an overview of the auxiliary files available at [227]:

1. ZcyclePulseSequence.xlsx: Excel sheet containing the abstract gate voltage and ESR pulse sequence for the surface code Z-cycle, as described in Sec. 4.3.1, outlined in Table 4.6.
2. XcyclePulseSequence.xlsx: Excel sheet containing the abstract gate voltage and ESR pulse sequence for the surface code X-cycle, as described in Sec. 4.3.1.
3. configurationsZ.txt: Text file containing the configurations (electron configurations and plunger configurations, as defined in Sec. 4.3.2, see item 4) whose sequence implements the Z-cycle shuttling protocol, $(C_0, C_1, \dots, C_6) = ((E_0, P_0), (E_1, P_1), \dots, (E_6, P_6))$, as rows. Qubit coordinates are as per Fig. 4.13. This file is an input for the shuttling verification algorithm.
4. shiftsZ.txt: Text file containing the shifts (describing the movement of electrons, as defined in Sec. 4.3.2, see item 6) of the Z-cycle shuttling protocol, $(S_{0 \rightarrow 1}, S_{1 \rightarrow 2}, \dots, S_{5 \rightarrow 6}) = ((\beta_{0 \rightarrow 1}, P_{0 \rightarrow 1}), (\beta_{1 \rightarrow 2}, P_{1 \rightarrow 2}), \dots, (\beta_{5 \rightarrow 6}, P_{5 \rightarrow 6}))$, as rows. Here, I use a slightly modified notation for convenience, depicted in Fig. 4.13. This file is an input for the shuttling verification algorithm.

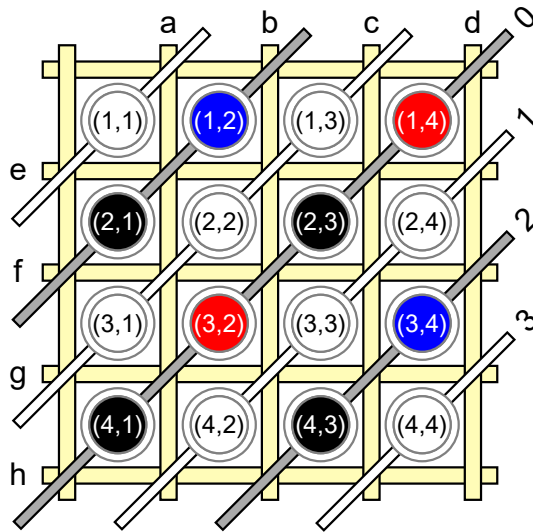


Figure 4.13: The 4×4 unit cell of the grid in the idle configuration with qubit coordinates and new notations for the barriers used in auxiliary files `shiftsZ.txt` and `shiftsX.txt`.

5. `configurationsX.txt`: Text file containing the electron configurations (defined in Sec. 4.3.2) whose sequence implements the X-cycle shuttling protocol. Qubit coordinates are as per Fig. 4.13. This file is an input for the shuttling verification algorithm.
6. `shiftsX.txt`: Text file containing the shifts (describing the movement of electrons) of the X-cycle shuttling protocol, as rows. Here, I use a slightly modified notation for convenience, depicted in Fig. 4.13. This file is an input for the shuttling verification algorithm.
7. `ZcycleMovie.pdf`: Document containing a visual representation of the abstract pulse sequence of the surface code Z-cycle (`ZcyclePulseSequence.xlsx`).
8. `XcycleMovie.pdf`: Document containing a visual representation of the abstract pulse sequence of the surface code X-cycle (`XcyclePulseSequence.xlsx`).

Additionally, my implementation of the shuttling verification algorithm (as described in Sec. 4.3.2) is available at the Zenodo repository [235].

4.5 Discussion

Hook errors: In general, to preserve the code distance of the surface code at the circuit level, the CNOT gates in the error detection circuits (Figs. 4.4(a) and (b)) must be arranged in a particular way such that a mid-circuit phase-flip (bit-flip) error occurring on the ancilla qubit A (B) propagates perpendicular to the logical X (Z) operator [183]. The effect of this type of errors and the optimal reordering of the entangling $\sqrt{\text{SWAP}}$ gates in the compiled error detection circuits (Figs. 4.6 and 4.7) remain to be explored.

Error scaling for an inhomogeneous (non-uniform) crossbar system: In this chapter, I considered a uniform (perfect) crossbar system only. However, in real experiments, quantum hardware always has some imperfections. A natural extension would be to incorporate such inhomogeneities in the logical error estimate.

Clifford-deformed surface codes: As argued in Sec. 4.2.5, spin qubits (especially in Si/SiGe heterostructures) are usually limited by dephasing. This introduces a bias in the noise: phase-flip errors are expected to be much more likely compared to bit-flip errors. In the presence of biased

noise, surface code variants with deformed stabilizers, e.g. the XZZX or the XY surface code, are shown to possess superior error correction performance [239–241]. Future work could discuss the compilation of the XZZX surface code to the crossbar architecture, using a modified error detection circuit.

4.6 Conclusions

In this chapter, I have made important steps towards the physical realization of quantum circuits in crossbar spin qubit architectures. In particular, I have identified an abstract pulse sequence, as well as a corresponding physical pulse sequence, which realizes surface-code quantum error correction in this platform. As an important ingredient, I have developed a verification algorithm that confirms that the gate-voltage changes in the abstract pulse sequence induce the desired real-space routing of the electrons in the quantum dot array. The identification of the physical pulse sequence enabled the refined estimation of the logical error probability. In fact, I showed a concrete, realistic parameter set that enables below-threshold surface code operation.

Chapter 5

Summary

In my thesis, I focused on spin qubit platforms that are promising candidates for the building blocks of future quantum computers. First, I studied the interplay of superconductivity with semiconductor nanostructures to gain insight into the key concepts and main challenges that have to be addressed when engineering topological qubits. As a step towards this implementation, I investigated a simple system, a conventional *s*-wave Josephson junction with a double quantum dot as a weak link. I described two interesting phenomena in detail, the even-odd effect, and the triplet blockade, both confirmed by experiment. The demonstrated triplet blockade mechanism could provide a coupling mechanism between spin qubits and (topological or non-topological) superconducting qubits.

In the context of simulating quantum error correction, motivated by the $1/f$ noise of condensed matter systems, I introduced a novel coherent noise model of phase damping where random angle coherent qubit rotations arise from Larmor frequency fluctuations. I argued that this model is relevant not only for semiconductor spin qubits but for any solid-state qubit platform, where the leading information loss mechanism is dephasing. I compared my model with the well-known model of independent single-qubit Pauli phase-flip errors and showed that for multiple cycles, quasistatic phase damping has a distinct effect. I also assessed the performance of the surface code in the presence of quasistatic phase damping and readout errors. The numerically established surface code error threshold is found to be close to that of independent phase-flip and readout errors. For the distance-3 surface code, I established the break-even boundary line on the parameter plane of the physical error rate and the readout error rate, providing guidelines for future experiments.

Finally, I made efforts to bring quantum error correction with spin qubits one step closer to physical realization by identifying a pulse sequence that realizes surface-code quantum error correction in a crossbar spin qubit array and showing a concrete, realistic parameter set that enables below-threshold surface code operation. The concepts and methods introduced here facilitate the realisation of quantum computing and quantum error correction with crossbar spin qubit architectures.

Thesis statements

1. I investigated a conventional *s*-wave Josephson junction with a double quantum dot as a weak link. Based on numerical simulations and analytical results in the perturbative regime I predicted an even-odd pattern in the (equilibrium) critical current. The cause of the switching between the even and odd patterns is identified as the change of the ground-state fermion parity. The sign of the supercurrent is uniquely determined by the ground state, up to leading order in perturbation theory. In the (1,1) charge sector of the serially coupled double quantum dot, the magnetically induced singlet-triplet ground-state transition has a significant effect on the supercurrent: the Josephson current carried by the triplet ground state at high magnetic field is much suppressed compared to the current carried by the singlet ground state at low magnetic field. I proved, in the framework of perturbation theory, the existence of strong triplet blockade in two different limiting cases: the large-superconducting-gap limit ($\Delta \gg U$), and the strong-Coulomb-repulsion limit ($U \gg \Delta$). Also in the perturbative framework, I have computed the number of processes contributing to the Josephson current for triplet and singlet states. This process counting indicates partial triplet blockade in the intermediate regime ($\Delta \approx U$). The even-odd effect and triplet blockade were confirmed by experiment. I took part in the interpretation of the experiment and the estimation of model parameters fitting the measurement data. I also proposed ways to utilize triplet blockade, for the readout of spin qubits and coupling to superconducting qubits.

Related publications: [I.](#) and [II.](#)

2. In the context of multi-cycle quantum error correction, I introduced the error model of quasistatic phase damping, which is a simplified model describing Larmor-frequency fluctuations due to $1/f$ noise. These Larmor-frequency fluctuations amount to unwanted coherent rotations whose axis is uniform, but the rotation angle is random across the qubit register. I proved that quasistatic phase damping error is equivalent to independent single-qubit Pauli phase-flip errors in the case of a single cycle of error detection or error correction. However, I found that for multiple cycles, quasistatic phase damping is distinct from independent phase-flip errors. I numerically investigated the performance of the surface code as quantum memory in the presence of quasistatic random coherent errors as well as (phenomenological) readout errors. I performed large-scale numerical experiments and established the surface code error correction threshold using a minimum-weight perfect matching decoder, as $p_{\text{th}} = 2.85\%$. This is close to the threshold with independent phase-flip errors and readout errors. At the threshold, the logical error rate for quasistatic phase damping combined with readout errors is around 7%, but for the combination of phase-flip and readout errors it is slightly higher, around 8.5%. I also determined the break-even boundary line for the distance-3 surface code on the parameter plane of the physical error rate and the readout error rate.

Related publication: [III](#).

3. I decomposed the surface code stabilizer measurement circuits in terms of single-qubit and two-qubit gates that are native to the crossbar spin-qubit architecture. I described a routing and scheduling protocol for the implementation of such a stabilizer measurement cycle. I identified a pulse sequence that realizes this protocol in the crossbar spin qubit array. As an important ingredient, I developed and implemented a verification algorithm that confirms that the gate-voltage changes in the abstract pulse sequence induce the desired real-space routing of the electrons in the quantum dot array. I transformed the abstract pulse sequence to a physical pulse sequence and systematically and quantitatively evaluated the logical error rates, taking into account idle qubit errors as well. I showed a concrete, realistic parameter set that enables below-threshold surface code operation.

Related publication: [IV](#).

Publications related to the thesis statements

- I. D. Pataki, and A. Pályi, Even-odd effect and triplet blockade in a double quantum dot Josephson junction. Proceedings of the PhD workshop of Physics Doctoral School at the Faculty of Natural Sciences, Budapest University of Technology and Economics (2020).
- II. D. Bouman, R. J. J. van Gulik, G. Steffensen, D. Pataki, P. Boross, P. Krogstrup, J. Nygård, J. Paaske, A. Pályi, and A. Geresdi, Triplet-blockaded Josephson supercurrent in double quantum dots. *Physical Review B* **102**(22), 220505(R) (2020).
- III. D. Pataki, Á. Márton, J. K. Asbóth, and A. Pályi, Coherent errors in stabilizer codes caused by quasistatic phase damping. *Physical Review A* **110**(1), 012417 (2024).
- IV. D. Pataki, and A. Pályi, Compiling the surface code to crossbar spin qubit architectures. *Physical Review B* **111**(11), 115307 (2025).

Acknowledgements

First and foremost, I would like to thank András Pályi, my supervisor. His guidance, patience, understanding, and insightful feedbacks have been invaluable throughout my PhD. His approach of capturing interesting physics via minimal models has always been inspiring for me. Through his mentorship, I have developed critical thinking skills and a more disciplined scientific mindset. His support has played a key role in both my personal and professional growth as a scientist.

I am grateful for the opportunity to study theoretical physics under the mentorship of outstanding professors such as Gergely Zaránd, Gábor Takács, László Orosz and Attila Viroztek. I am equally thankful for my BSc and MSc supervisors, Ádám Gali and Balázs Dóra. I am also grateful to my high school teacher, György Varga, for initially inspiring my interest in physics.

I have been fortunate to have some great colleagues and friends at the university. I would like to thank everyone including Péter Boross, Áron Márton, János Asbóth, Bendegúz Nyári, Baksa Kolok, Bálint Domokos, Zoli Guba, Aritra Sen, Domonkos Svastits, György Frank, Zoltán Okvátovity, Bálint Szentpéteri, Máté Kedves, Csaba Holló, Csilla Király, and Áron Rozgonyi for the helpful comments and insightful discussions throughout the years.

I am equally grateful to my friends beyond the academic world, such as Patrik Miller, János Duchaj, Robert Tarr, Ákos Palla, Róbert Rednic, Judit Szabó, Zsuzsanna Nagy, and Sára Jakab, whose encouragement and support were invaluable in keeping me motivated during my PhD.

Finally, this work would not have been possible without the love and constant support of my parents, brother, and sister. Thank you, I would not have made it this far without you!

This research was supported by the Ministry of Culture and Innovation and the National Research, Development and Innovation Office within the Quantum Information National Laboratory of Hungary (Grant No. 2022-2.1.1-NL-2022-00004). This research was supported by the Horizon Europe research and innovation programme of the European Union through the projects IGNITE, OpenSuperQPlus, and QLSI2, as well as by the National Research, Development and Innovation Office via the OTKA Grant No. 132146.

Bibliography

- [1] G. E. Moore, Cramming more components onto integrated circuits, *Electronics* **38**, 114 (1965).
- [2] P. W. Shor, Polynomial-time algorithms for prime factorization and discrete logarithms on a quantum computer, *SIAM Journal on Computing* **26**, 1484–1509 (1997).
- [3] B. Fauseweh, Quantum many-body simulations on digital quantum computers: State-of-the-art and future challenges, *Nature Communications* **15**, 2123 (2024).
- [4] A. M. Dalzell, S. McArdle, M. Berta, *et al.*, Quantum algorithms: A survey of applications and end-to-end complexities (2025), arXiv:2310.03011 .
- [5] A. Abbas, A. Ambainis, B. Augustino, *et al.*, Challenges and opportunities in quantum optimization, *Nature Reviews Physics* **6**, 718–735 (2024).
- [6] J. Preskill, Quantum Computing in the NISQ era and beyond, *Quantum* **2**, 79 (2018).
- [7] T. L. Scholten, C. J. Williams, D. Moody, M. Mosca, W. Hurley, W. J. Zeng, M. Troyer, and J. M. Gambetta, Assessing the benefits and risks of quantum computers (2024), arXiv:2401.16317 .
- [8] Z. C. Seskir, R. Korkmaz, and A. U. Aydinoglu, The landscape of the quantum start-up ecosystem, *EPJ Quantum Technology* **9**, 27 (2022).
- [9] M. A. Nielsen and I. L. Chuang, *Quantum Computation and Quantum Information: 10th Anniversary Edition* (Cambridge University Press, 2012).
- [10] A. Y. Kitaev, Quantum computations: algorithms and error correction, *Russian Mathematical Surveys* **52**, 1191–1249 (1997).
- [11] D. Gottesman, The Heisenberg representation of quantum computers (1998), arXiv:quant-ph/9807006 .
- [12] S. Aaronson and D. Gottesman, Improved simulation of stabilizer circuits, *Phys. Rev. A* **70**, 052328 (2004).
- [13] C. Gidney, Stim: a fast stabilizer circuit simulator, *Quantum* **5**, 497 (2021).
- [14] H. Thomas, P.-E. Emeriau, E. Kashefi, H. Ollivier, and U. Chabaud, On the role of coherence for quantum computational advantage (2024), arXiv:2410.07024 .
- [15] E. Knill, Quantum computing with realistically noisy devices, *Nature* **434**, 39–44 (2005).
- [16] S. Bravyi and A. Kitaev, Universal quantum computation with ideal Clifford gates and noisy ancillas, *Phys. Rev. A* **71**, 022316 (2005).

- [17] R. Raussendorf and H. J. Briegel, A one-way quantum computer, *Phys. Rev. Lett.* **86**, 5188–5191 (2001).
- [18] R. Raussendorf, D. E. Browne, and H. J. Briegel, Measurement-based quantum computation on cluster states, *Phys. Rev. A* **68**, 022312 (2003).
- [19] H. J. Briegel, D. E. Browne, W. Dür, R. Raussendorf, and M. Van den Nest, Measurement-based quantum computation, *Nature Physics* **5**, 19–26 (2009).
- [20] K. Alexander, A. Benyamini, D. Black, *et al.*, A manufacturable platform for photonic quantum computing, *Nature* **641**, 876–883 (2025).
- [21] C. Gidney and M. Ekerå, How to factor 2048 bit RSA integers in 8 hours using 20 million noisy qubits, *Quantum* **5**, 433 (2021).
- [22] N. W. Hendrickx, W. I. L. Lawrie, M. Russ, F. van Riggelen, S. L. de Snoo, R. N. Schouten, A. Sammak, G. Scappucci, and M. Veldhorst, A four-qubit germanium quantum processor, *Nature* **591**, 580–585 (2021).
- [23] G. Burkard, T. D. Ladd, A. Pan, J. M. Nichol, and J. R. Petta, Semiconductor spin qubits, *Rev. Mod. Phys.* **95**, 025003 (2023).
- [24] M. Kjaergaard, M. E. Schwartz, J. Braumüller, P. Krantz, J. I.-J. Wang, S. Gustavsson, and W. D. Oliver, Superconducting qubits: Current state of play, *Annual Review of Condensed Matter Physics* **11**, 369–395 (2020).
- [25] A. Noiri, K. Takeda, T. Nakajima, T. Kobayashi, A. Sammak, G. Scappucci, and S. Tarucha, Fast universal quantum gate above the fault-tolerance threshold in silicon, *Nature* **601**, 338–342 (2022).
- [26] X. Xue, M. Russ, N. Samkharadze, B. Undseth, A. Sammak, G. Scappucci, and L. M. Vandersypen, Quantum logic with spin qubits crossing the surface code threshold, *Nature* **601**, 343–347 (2022).
- [27] L. M. K. Vandersypen, H. Bluhm, J. S. Clarke, A. S. Dzurak, R. Ishihara, A. Morello, D. J. Reilly, L. R. Schreiber, and M. Veldhorst, Interfacing spin qubits in quantum dots and donors—hot, dense, and coherent, *npj Quantum Information* **3**, 34 (2017).
- [28] L. Petit, H. G. J. Eenink, M. Russ, W. I. L. Lawrie, N. W. Hendrickx, S. G. J. Philips, J. S. Clarke, L. M. K. Vandersypen, and M. Veldhorst, Universal quantum logic in hot silicon qubits, *Nature* **580**, 355–359 (2020).
- [29] C. H. Yang, R. C. C. Leon, J. C. C. Hwang, *et al.*, Operation of a silicon quantum processor unit cell above one kelvin, *Nature* **580**, 350–354 (2020).
- [30] L. C. Camenzind, S. Geyer, A. Fuhrer, R. J. Warburton, D. M. Zumbühl, and A. V. Kuhlmann, A hole spin qubit in a fin field-effect transistor above 4 kelvin, *Nature Electronics* **5**, 178–183 (2022).
- [31] J. Y. Huang, R. Y. Su, W. H. Lim, *et al.*, High-fidelity spin qubit operation and algorithmic initialization above 1 K, *Nature* **627**, 772–777 (2024).
- [32] R. Maurand, X. Jehl, D. Kotekar-Patil, *et al.*, A CMOS silicon spin qubit, *Nature Communications* **7**, 13575 (2016).
- [33] M. Veldhorst, H. G. J. Eenink, C. H. Yang, and A. S. Dzurak, Silicon CMOS architecture for a spin-based quantum computer, *Nature Communications* **8**, 1766 (2017).

- [34] S. Neyens, O. K. Zietz, T. F. Watson, *et al.*, Probing single electrons across 300-mm spin qubit wafers, *Nature* **629**, 80–85 (2024).
- [35] R. Hanson, L. P. Kouwenhoven, J. R. Petta, S. Tarucha, and L. M. K. Vandersypen, Spins in few-electron quantum dots, *Rev. Mod. Phys.* **79**, 1217–1265 (2007).
- [36] T. Tanttu, B. Hensen, K. W. Chan, *et al.*, Controlling spin-orbit interactions in silicon quantum dots using magnetic field direction, *Phys. Rev. X* **9**, 021028 (2019).
- [37] L. Han, M. Chan, D. de Jong, C. Prosko, G. Badawy, S. Gazibegovic, E. P. Bakkers, L. P. Kouwenhoven, F. K. Malinowski, and W. Pfaff, Variable and orbital-dependent spin-orbit field orientations in an InSb double quantum dot characterized via dispersive gate sensing, *Phys. Rev. Appl.* **19**, 014063 (2023).
- [38] N. W. Hendrickx, L. Massai, M. Mergenthaler, F. J. Schupp, S. Paredes, S. W. Bedell, G. Salis, and A. Fuhrer, Sweet-spot operation of a germanium hole spin qubit with highly anisotropic noise sensitivity, *Nature Materials* **23**, 920–927 (2024).
- [39] S. Nadj-Perge, S. M. Frolov, E. P. A. M. Bakkers, and L. P. Kouwenhoven, Spin-orbit qubit in a semiconductor nanowire, *Nature* **468**, 1084–1087 (2010).
- [40] C.-A. Wang, V. John, H. Tidjani, *et al.*, Operating semiconductor quantum processors with hopping spins, *Science* **385**, 447–452 (2024).
- [41] D. Loss and D. P. DiVincenzo, Quantum computation with quantum dots, *Phys. Rev. A* **57**, 120–126 (1998).
- [42] S. Geyer, B. Hetényi, S. Bosco, L. C. Camenzind, R. S. Egli, A. Fuhrer, D. Loss, R. J. Warburton, D. M. Zumbühl, and A. V. Kuhlmann, Anisotropic exchange interaction of two hole-spin qubits, *Nature Physics* **20**, 1152–1157 (2024).
- [43] M. Field, C. G. Smith, M. Pepper, D. A. Ritchie, J. E. F. Frost, G. A. C. Jones, and D. G. Hasko, Measurements of Coulomb blockade with a noninvasive voltage probe, *Phys. Rev. Lett.* **70**, 1311–1314 (1993).
- [44] T. Frey, P. J. Leek, M. Beck, A. Blais, T. Ihn, K. Ensslin, and A. Wallraff, Dipole coupling of a double quantum dot to a microwave resonator, *Phys. Rev. Lett.* **108**, 046807 (2012).
- [45] K. D. Petersson, L. W. McFaul, M. D. Schroer, M. Jung, J. M. Taylor, A. A. Houck, and J. R. Petta, Circuit quantum electrodynamics with a spin qubit, *Nature* **490**, 380–383 (2012).
- [46] S. G. J. Philips, M. T. Mađzik, S. V. Amitonov, *et al.*, Universal control of a six-qubit quantum processor in silicon, *Nature* **609**, 919–924 (2022).
- [47] V. John, C. X. Yu, B. van Straaten, *et al.*, A two-dimensional 10-qubit array in germanium with robust and localised qubit control (2024), arXiv:2412.16044 .
- [48] H. C. George, M. T. Mađzik, E. M. Henry, *et al.*, 12-spin-qubit arrays fabricated on a 300 mm semiconductor manufacturing line, *Nano Letters* **25**, 793–799 (2024).
- [49] J. R. Petta, A. C. Johnson, J. M. Taylor, E. A. Laird, A. Yacoby, M. D. Lukin, C. M. Marcus, M. P. Hanson, and A. C. Gossard, Coherent manipulation of coupled electron spins in semiconductor quantum dots, *Science* **309**, 2180–2184 (2005).
- [50] D. Jirovec, A. Hofmann, A. Ballabio, *et al.*, A singlet-triplet hole spin qubit in planar Ge, *Nature Materials* **20**, 1106–1112 (2021).

- [51] X. Zhang, E. Morozova, M. Rimbach-Russ, *et al.*, Universal control of four singlet–triplet qubits, *Nature Nanotechnology* **20**, 209–215 (2024).
- [52] D. P. DiVincenzo, D. Bacon, J. Kempe, G. Burkard, and K. B. Whaley, Universal quantum computation with the exchange interaction, *Nature* **408**, 339–342 (2000).
- [53] E. Acuna, J. D. Broz, K. Shyamsundar, *et al.*, Coherent control of a triangular exchange-only spin qubit, *Phys. Rev. Appl.* **22**, 044057 (2024).
- [54] A. J. Weinstein, M. D. Reed, A. M. Jones, *et al.*, Universal logic with encoded spin qubits in silicon, *Nature* **615**, 817–822 (2023).
- [55] I. Heinz, F. Borjans, M. Curry, R. Kotlyar, F. Luthi, M. T. Mađzik, F. A. Mohiyaddin, N. Bishop, and G. Burkard, Fast quantum gates for exchange-only qubits using simultaneous exchange pulses (2024), arXiv:2409.05843 .
- [56] A. Sala and J. Danon, Exchange-only singlet-only spin qubit, *Phys. Rev. B* **95**, 241303 (2017).
- [57] M. Russ, J. R. Petta, and G. Burkard, Quadrupolar exchange-only spin qubit, *Phys. Rev. Lett.* **121**, 177701 (2018).
- [58] B. E. Kane, A silicon-based nuclear spin quantum computer, *Nature* **393**, 133–137 (1998).
- [59] P. Neumann, J. Beck, M. Steiner, F. Rempp, H. Fedder, P. R. Hemmer, J. Wrachtrup, and F. Jelezko, Single-shot readout of a single nuclear spin, *Science* **329**, 542–544 (2010).
- [60] K. Barnes, P. Battaglino, B. J. Bloom, *et al.*, Assembly and coherent control of a register of nuclear spin qubits, *Nature Communications* **13**, 2779 (2022).
- [61] I. Thorvaldson, D. Poulos, C. M. Moehle, *et al.*, Grover’s algorithm in a four-qubit silicon processor above the fault-tolerant threshold, *Nature Nanotechnology* **20**, 472–477 (2025).
- [62] Y. Kim, A. Eddins, S. Anand, *et al.*, Evidence for the utility of quantum computing before fault tolerance, *Nature* **618**, 500–505 (2023).
- [63] Google Quantum AI and Collaborators, Quantum error correction below the surface code threshold, *Nature* **638**, 920–926 (2024).
- [64] J. Koch, T. M. Yu, J. Gambetta, A. A. Houck, D. I. Schuster, J. Majer, A. Blais, M. H. Devoret, S. M. Girvin, and R. J. Schoelkopf, Charge-insensitive qubit design derived from the Cooper pair box, *Phys. Rev. A* **76**, 042319 (2007).
- [65] M. McEwen, D. Kafri, Z. Chen, *et al.*, Removing leakage-induced correlated errors in superconducting quantum error correction, *Nature Communications* **12**, 1761 (2021).
- [66] Y. Nakamura, Y. A. Pashkin, and J. S. Tsai, Coherent control of macroscopic quantum states in a single-Cooper-pair box, *Nature* **398**, 786–788 (1999).
- [67] J. Clarke and F. K. Wilhelm, Superconducting quantum bits, *Nature* **453**, 1031–1042 (2008).
- [68] L. Abdurakhimov, J. Adam, H. Ahmad, *et al.*, Technology and performance benchmarks of IQM’s 20-qubit quantum computer (2024), arXiv:2408.12433 .
- [69] C. K. Andersen, A. Remm, S. Lazar, S. Krinner, N. Lacroix, G. J. Norris, M. Gabureac, C. Eichler, and A. Wallraff, Repeated quantum error detection in a surface code, *Nature Physics* **16**, 875–880 (2020).

- [70] T. Dirks, T. L. Hughes, S. Lal, B. Uchoa, Y.-F. Chen, C. Chialvo, P. M. Goldbart, and N. Mason, Transport through Andreev bound states in a graphene quantum dot, *Nature Physics* **7**, 386–390 (2011).
- [71] S. Park and A. L. Yeyati, Andreev spin qubits in multichannel Rashba nanowires, *Phys. Rev. B* **96**, 125416 (2017).
- [72] M. Hays, V. Fatemi, D. Bouman, *et al.*, Coherent manipulation of an Andreev spin qubit, *Science* **373**, 430–433 (2021).
- [73] M. Pita-Vidal, J. J. Wesdorp, L. J. Splitthoff, A. Bargerbos, Y. Liu, L. P. Kouwenhoven, and C. K. Andersen, Strong tunable coupling between two distant superconducting spin qubits, *Nature Physics* **20**, 1158–1163 (2024).
- [74] J. K. Asbóth, L. Oroszlány, and A. Pályi, *A Short Course on Topological Insulators* (Springer International Publishing, 2016).
- [75] A. Kitaev, Fault-tolerant quantum computation by anyons, *Annals of Physics* **303**, 2–30 (2003).
- [76] A. Kitaev, Anyons in an exactly solved model and beyond, *Annals of Physics* **321**, 2–111 (2006).
- [77] A. Y. Kitaev, Unpaired Majorana fermions in quantum wires, *Physics-Uspekhi* **44**, 131–136 (2001).
- [78] S. D. Sarma, M. Freedman, and C. Nayak, Majorana zero modes and topological quantum computation, *npj Quantum Information* **1**, 15001 (2015).
- [79] C. W. J. Beenakker, Search for non-Abelian Majorana braiding statistics in superconductors, *SciPost Phys. Lect. Notes* , 15 (2020).
- [80] Microsoft Azure Quantum, Interferometric single-shot parity measurement in InAs–Al hybrid devices, *Nature* **638**, 651–655 (2025).
- [81] P. Boross, J. K. Asbóth, G. Széchenyi, L. Oroszlány, and A. Pályi, Poor man’s topological quantum gate based on the Su-Schrieffer-Heeger model, *Phys. Rev. B* **100**, 045414 (2019).
- [82] G. Széchenyi and A. Pályi, Parity-to-charge conversion for readout of topological Majorana qubits, *Phys. Rev. B* **101**, 235441 (2020).
- [83] V. Derakhshan Maman, M. Gonzalez-Zalba, and A. Pályi, Charge noise and overdrive errors in dispersive readout of charge, spin, and Majorana qubits, *Phys. Rev. Appl.* **14**, 064024 (2020).
- [84] P. Boross and A. Pályi, Dephasing of Majorana qubits due to quasistatic disorder, *Phys. Rev. B* **105**, 035413 (2022).
- [85] P. Boross and A. Pályi, Braiding-based quantum control of a Majorana qubit built from quantum dots, *Phys. Rev. B* **109**, 125410 (2024).
- [86] M. Leijnse and K. Flensberg, Parity qubits and poor man’s Majorana bound states in double quantum dots, *Phys. Rev. B* **86** (2012).
- [87] J. D. Sau and S. Das Sarma, Realizing a robust practical Majorana chain in a quantum-dot-superconductor linear array, *Nature Communications* **3**, 964 (2012).

- [88] A. Brunetti, A. Zazunov, A. Kundu, and R. Egger, Anomalous Josephson current, incipient time-reversal symmetry breaking, and Majorana bound states in interacting multilevel dots, *Phys. Rev. B* **88**, 144515 (2013).
- [89] W. Samuelson, V. Svensson, and M. Leijnse, Minimal quantum dot based Kitaev chain with only local superconducting proximity effect, *Phys. Rev. B* **109**, 035415 (2024).
- [90] C. Gidney, How to factor 2048 bit RSA integers with less than a million noisy qubits (2025), arXiv:2505.15917 .
- [91] P. W. Shor, Scheme for reducing decoherence in quantum computer memory, *Phys. Rev. A* **52**, R2493–R2496 (1995).
- [92] E. Knill, R. Laflamme, and W. H. Zurek, Resilient quantum computation, *Science* **279**, 342–345 (1998).
- [93] P. Aliferis, D. Gottesman, and J. Preskill, Quantum accuracy threshold for concatenated distance-3 code, *Quantum Information and Computation* **6**, 97–165 (2006).
- [94] D. Aharonov and M. Ben-Or, Fault-tolerant quantum computation with constant error rate, *SIAM Journal on Computing* **38**, 1207–1282 (2008).
- [95] R. LaRose, A brief history of quantum vs classical computational advantage (2024), arXiv:2412.14703 .
- [96] M. A. Nielsen, Cluster-state quantum computation, *Reports on Mathematical Physics* **57**, 147–161 (2006).
- [97] D. Gottesman, Stabilizer codes and quantum error correction (1997), arXiv:quant-ph/9705052 .
- [98] S. B. Bravyi and A. Y. Kitaev, Quantum codes on a lattice with boundary (1998), arXiv:quant-ph/9811052 .
- [99] E. Dennis, A. Kitaev, A. Landahl, and J. Preskill, Topological quantum memory, *Journal of Mathematical Physics* **43**, 4452–4505 (2002).
- [100] A. G. Fowler, M. Mariantoni, J. M. Martinis, and A. N. Cleland, Surface codes: Towards practical large-scale quantum computation, *Phys. Rev. A* **86**, 032324 (2012).
- [101] H. Bombin and M. A. Martin-Delgado, Optimal resources for topological two-dimensional stabilizer codes: Comparative study, *Phys. Rev. A* **76**, 012305 (2007).
- [102] Quantum Code Visualizer by A. Pesah and E. Huang, <https://gui.quantumcodes.io>.
- [103] C. A. Pattison, M. E. Beverland, M. P. da Silva, and N. Delfosse, Improved quantum error correction using soft information (2021), arXiv:2107.13589 .
- [104] J. Bausch, A. W. Senior, F. J. H. Heras, *et al.*, Learning high-accuracy error decoding for quantum processors, *Nature* **635**, 834–840 (2024).
- [105] N. Shutty, M. Newman, and B. Villalonga, Efficient near-optimal decoding of the surface code through ensembling (2024), arXiv:2401.12434 .
- [106] N. Liyanage, Y. Wu, S. Tagare, and L. Zhong, FPGA-based distributed union-find decoder for surface codes, *IEEE Transactions on Quantum Engineering* **5**, 1–17 (2024).

- [107] C. Jones, Improved accuracy for decoding surface codes with matching synthesis (2024), arXiv:2408.12135 .
- [108] H. Bombín, C. Dawson, R. V. Mishmash, N. Nickerson, F. Pastawski, and S. Roberts, Logical blocks for fault-tolerant topological quantum computation, *PRX Quantum* **4**, 020303 (2023).
- [109] S. Krinner, N. Lacroix, A. Remm, *et al.*, Realizing repeated quantum error correction in a distance-three surface code, *Nature* **605**, 669–674 (2022).
- [110] Y. Zhao, Y. Ye, H.-L. Huang, *et al.*, Realization of an error-correcting surface code with superconducting qubits, *Phys. Rev. Lett.* **129**, 030501 (2022).
- [111] Google Quantum AI, Suppressing quantum errors by scaling a surface code logical qubit, *Nature* **614**, 676–681 (2023).
- [112] K. Takeda, A. Noiri, T. Nakajima, T. Kobayashi, and S. Tarucha, Quantum error correction with silicon spin qubits, *Nature* **608**, 682–686 (2022).
- [113] F. van Riggelen, W. I. L. Lawrie, M. Russ, N. W. Hendrickx, A. Sammak, M. Rispler, B. M. Terhal, G. Scappucci, and M. Veldhorst, Phase flip code with semiconductor spin qubits, *npj Quantum Information* **8**, 124 (2022).
- [114] C. Wang, J. Harrington, and J. Preskill, Confinement-Higgs transition in a disordered gauge theory and the accuracy threshold for quantum memory, *Annals of Physics* **303**, 31–58 (2003).
- [115] S. Bravyi, M. Englbrecht, R. König, and N. Peard, Correcting coherent errors with surface codes, *npj Quantum Information* **4**, 55 (2018).
- [116] F. Venn and B. Béri, Error-correction and noise-decoherence thresholds for coherent errors in planar-graph surface codes, *Phys. Rev. Res.* **2**, 043412 (2020).
- [117] Á. Márton and J. K. Asbóth, Coherent errors and readout errors in the surface code, *Quantum* **7**, 1116 (2023).
- [118] M. Tinkham, *Introduction to Superconductivity*, Dover Books on Physics Series (Dover Publications, 2004).
- [119] B. Josephson, Possible new effects in superconductive tunnelling, *Physics Letters* **1**, 251–253 (1962).
- [120] P. Krantz, M. Kjaergaard, F. Yan, T. P. Orlando, S. Gustavsson, and W. D. Oliver, A quantum engineer’s guide to superconducting qubits, *Applied Physics Reviews* **6**, 021318 (2019).
- [121] J. Q. You and F. Nori, Atomic physics and quantum optics using superconducting circuits, *Nature* **474**, 589–597 (2011).
- [122] V. V. Ryazanov, V. A. Oboznov, A. Y. Rusanov, A. V. Veretennikov, A. A. Golubov, and J. Aarts, Coupling of two superconductors through a ferromagnet: Evidence for a π junction, *Phys. Rev. Lett.* **86**, 2427–2430 (2001).
- [123] T. Kontos, M. Aprili, J. Lesueur, F. Genêt, B. Stephanidis, and R. Boursier, Josephson junction through a thin ferromagnetic layer: Negative coupling, *Phys. Rev. Lett.* **89**, 137007 (2002).

- [124] J. J. A. Baselmans, A. F. Morpurgo, B. J. van Wees, and T. M. Klapwijk, Reversing the direction of the supercurrent in a controllable Josephson junction, *Nature* **397**, 43–45 (1999).
- [125] J. A. van Dam, Y. V. Nazarov, E. P. A. M. Bakkers, S. De Franceschi, and L. P. Kouwenhoven, Supercurrent reversal in quantum dots, *Nature* **442**, 667–670 (2006).
- [126] R. Delagrangé, R. Weil, A. Kasumov, M. Ferrier, H. Bouchiat, and R. Deblock, $0-\pi$ quantum transition in a carbon nanotube Josephson junction: Universal phase dependence and orbital degeneracy, *Phys. Rev. B* **93**, 195437 (2016).
- [127] L. Hofstetter, A. Geresdi, M. Aagesen, J. Nygård, C. Schönenberger, and S. Csonka, Ferromagnetic proximity effect in a ferromagnet–quantum-dot–superconductor device, *Phys. Rev. Lett.* **104**, 246804 (2010).
- [128] L. Hofstetter, S. Csonka, A. Baumgartner, G. Fülöp, S. d’Hollosy, J. Nygård, and C. Schönenberger, Finite-bias Cooper pair splitting, *Phys. Rev. Lett.* **107**, 136801 (2011).
- [129] Z. Scherübl, A. Pályi, and S. Csonka, Probing individual split Cooper pairs using the spin qubit toolkit, *Phys. Rev. B* **89**, 205439 (2014).
- [130] Z. Scherübl, A. Pályi, and S. Csonka, Transport signatures of an Andreev molecule in a quantum dot–superconductor–quantum dot setup, *Beilstein Journal of Nanotechnology* **10**, 363–378 (2019).
- [131] Z. Scherübl, G. Fülöp, C. P. Moca, J. Gramich, A. Baumgartner, P. Makk, T. Elalaily, C. Schönenberger, J. Nygård, G. Zaránd, and S. Csonka, Large spatial extension of the zero-energy Yu–Shiba–Rusinov state in a magnetic field, *Nature Communications* **11**, 1834 (2020).
- [132] T. Elalaily, O. Kürtössy, V. Zannier, Z. Scherübl, I. E. Lukács, P. Srivastava, F. Rossi, L. Sorba, S. Csonka, and P. Makk, Probing proximity-induced superconductivity in InAs nanowires using built-in barriers, *Phys. Rev. Appl.* **14**, 044002 (2020).
- [133] O. Kürtössy, Z. Scherübl, G. Fülöp, I. E. Lukács, T. Kanne, J. Nygård, P. Makk, and S. Csonka, Andreev molecule in parallel InAs nanowires, *Nano Letters* **21**, 7929–7937 (2021).
- [134] T. Elalaily, O. Kürtössy, Z. Scherübl, M. Berke, G. Fülöp, I. E. Lukács, T. Kanne, J. Nygård, K. Watanabe, T. Taniguchi, P. Makk, and S. Csonka, Gate-controlled supercurrent in epitaxial Al/InAs nanowires, *Nano Letters* **21**, 9684–9690 (2021).
- [135] O. Kürtössy, Z. Scherübl, G. Fülöp, I. E. Lukács, T. Kanne, J. Nygård, P. Makk, and S. Csonka, Parallel InAs nanowires for Cooper pair splitters with Coulomb repulsion, *npj Quantum Materials* **7**, 88 (2022).
- [136] M. Kocsis, Z. Scherübl, G. Fülöp, P. Makk, and S. Csonka, Strong nonlocal tuning of the current-phase relation of a quantum dot based Andreev molecule, *Phys. Rev. B* **109**, 245133 (2024).
- [137] Z. Scherübl, M. Sütő, D. Kóti, *et al.*, Determination of the current-phase relation of an InAs 2DEG Josephson junction with a microwave resonator, *Phys. Rev. Res.* **7**, 023173 (2025).

- [138] O. Kürtössy, M. Bodócs, C. P. Moca, Z. Scherübl, E. Nikodem, T. Kanne, J. Nygård, G. Zaránd, P. Makk, and S. Csonka, Heteroatomic Andreev molecule in a superconducting island-double quantum dot hybrid (2024), arXiv:2407.00825 .
- [139] M.-S. Choi, C. Bruder, and D. Loss, Spin-dependent Josephson current through double quantum dots and measurement of entangled electron states, *Phys. Rev. B* **62**, 13569–13572 (2000).
- [140] Y. Zhu, Q. Sun, and T. Lin, Probing spin states of coupled quantum dots by a dc Josephson current, *Phys. Rev. B* **66**, 085306 (2002).
- [141] A. Martín-Rodero and A. L. Yeyati, Josephson and Andreev transport through quantum dots, *Advances in Physics* **60**, 899–958 (2011).
- [142] S. Droste, S. Andergassen, and J. Splettstoesser, Josephson current through interacting double quantum dots with spin-orbit coupling, *Journal of Physics: Condensed Matter* **24**, 415301 (2012).
- [143] V. Pokorný, M. Žonda, G. Loukeris, and T. Novotný, Second order perturbation theory for a superconducting double quantum dot, in *Proceedings of the International Conference on Strongly Correlated Electron Systems (SCES2019)* (Journal of the Physical Society of Japan, 2020).
- [144] D. Bouman, R. J. J. van Gulik, G. Steffensen, D. Pataki, P. Boross, P. Krogstrup, J. Nygård, J. Paaske, A. Pályi, and A. Geresdi, Triplet-blockaded Josephson supercurrent in double quantum dots, *Phys. Rev. B* **102**, 220505 (2020).
- [145] E. Vecino, A. Martín-Rodero, and A. L. Yeyati, Josephson current through a correlated quantum level: Andreev states and π junction behavior, *Phys. Rev. B* **68**, 035105 (2003).
- [146] J. C. Estrada Saldaña, A. Vekris, G. Steffensen, R. Žitko, P. Krogstrup, J. Paaske, K. Grove-Rasmussen, and J. Nygård, Supercurrent in a double quantum dot, *Phys. Rev. Lett.* **121**, 257701 (2018).
- [147] M. D. Schroer, K. D. Petersson, M. Jung, and J. R. Petta, Field tuning the g factor in InAs nanowire double quantum dots, *Phys. Rev. Lett.* **107**, 176811 (2011).
- [148] B. I. Spivak and S. A. Kivelson, Negative local superfluid densities: The difference between dirty superconductors and dirty Bose liquids, *Phys. Rev. B* **43**, 3740–3743 (1991).
- [149] W. G. van der Wiel, S. De Franceschi, J. M. Elzerman, T. Fujisawa, S. Tarucha, and L. P. Kouwenhoven, Electron transport through double quantum dots, *Rev. Mod. Phys.* **75**, 1–22 (2002).
- [150] M. L. Della Rocca, M. Chauvin, B. Huard, H. Pothier, D. Esteve, and C. Urbina, Measurement of the current-phase relation of superconducting atomic contacts, *Phys. Rev. Lett.* **99**, 127005 (2007).
- [151] J. A. van Dam, Y. V. Nazarov, E. P. A. M. Bakkers, S. De Franceschi, and L. P. Kouwenhoven, Supercurrent reversal in quantum dots, *Nature* **442**, 667–670 (2006).
- [152] Wolfram Research Inc., Mathematica, Version 13.3.
- [153] C. Karrasch, S. Andergassen, and V. Meden, Supercurrent through a multilevel quantum dot close to singlet-triplet degeneracy, *Phys. Rev. B* **84**, 134512 (2011).

- [154] A. Bargerbos, M. Pita-Vidal, R. Žitko, *et al.*, Singlet-doublet transitions of a quantum dot Josephson junction detected in a transmon circuit, *PRX Quantum* **3**, 030311 (2022).
- [155] T. Dvir, G. Wang, N. van Loo, *et al.*, Realization of a minimal Kitaev chain in coupled quantum dots, *Nature* **614**, 445–450 (2023).
- [156] F. Zatelli, D. van Driel, D. Xu, *et al.*, Robust poor man’s Majorana zero modes using Yu-Shiba-Rusinov states, *Nature Communications* **15**, 7933 (2024).
- [157] S. L. D. ten Haaf, Q. Wang, A. M. Bozkurt, *et al.*, A two-site Kitaev chain in a two-dimensional electron gas, *Nature* **630**, 329–334 (2024).
- [158] S. L. D. ten Haaf, Y. Zhang, Q. Wang, *et al.*, Observation of edge and bulk states in a three-site Kitaev chain, *Nature* **641**, 890–895 (2025).
- [159] A. Bordin, C.-X. Liu, T. Dvir, *et al.*, Enhanced Majorana stability in a three-site Kitaev chain, *Nature Nanotechnology* **20**, 726–731 (2025).
- [160] C. Ryan-Anderson, J. G. Bohnet, K. Lee, *et al.*, Realization of real-time fault-tolerant quantum error correction, *Phys. Rev. X* **11**, 041058 (2021).
- [161] L. Egan, D. M. Debroy, C. Noel, *et al.*, Fault-tolerant control of an error-corrected qubit, *Nature* **598**, 281–286 (2021).
- [162] N. M. Linke, M. Gutierrez, K. A. Landsman, C. Figgatt, S. Debnath, K. R. Brown, and C. Monroe, Fault-tolerant quantum error detection, *Science Advances* **3**, e1701074 (2017).
- [163] D. Nigg, M. Müller, E. A. Martinez, P. Schindler, M. Hennrich, T. Monz, M. A. Martin-Delgado, and R. Blatt, Quantum computations on a topologically encoded qubit, *Science* **345**, 302–305 (2014).
- [164] M. H. Abobeih, Y. Wang, J. Randall, S. J. H. Loenen, C. E. Bradley, M. Markham, D. J. Twitchen, B. M. Terhal, and T. H. Taminiau, Fault-tolerant operation of a logical qubit in a diamond quantum processor, *Nature* **606**, 884–889 (2022).
- [165] D. Bluvstein, H. Levine, G. Semeghini, *et al.*, A quantum processor based on coherent transport of entangled atom arrays, *Nature* **604**, 451–456 (2022).
- [166] D. Bluvstein, S. J. Evered, A. A. Geim, *et al.*, Logical quantum processor based on reconfigurable atom arrays, *Nature* **626**, 58–65 (2023).
- [167] S. J. Beale, J. J. Wallman, M. Gutiérrez, K. R. Brown, and R. Laflamme, Quantum error correction decoheres noise, *Phys. Rev. Lett.* **121**, 190501 (2018).
- [168] F. Venn, J. Behrends, and B. Béri, Coherent-error threshold for surface codes from Majorana delocalization, *Phys. Rev. Lett.* **131**, 060603 (2023).
- [169] M. Takita, A. W. Cross, A. D. Córcoles, J. M. Chow, and J. M. Gambetta, Experimental demonstration of fault-tolerant state preparation with superconducting qubits, *Phys. Rev. Lett.* **119**, 180501 (2017).
- [170] M. Gong, X. Yuan, S. Wang, *et al.*, Experimental exploration of five-qubit quantum error-correcting code with superconducting qubits, *National Science Review* **9**, nwab011 (2021).
- [171] J. F. Marques, B. M. Varbanov, M. S. Moreira, *et al.*, Logical-qubit operations in an error-detecting surface code, *Nature Physics* **18**, 80–86 (2021).

- [172] Y. Nakamura, Y. A. Pashkin, T. Yamamoto, and J. S. Tsai, Charge echo in a Cooper-pair box, *Phys. Rev. Lett.* **88**, 047901 (2002).
- [173] F. Yoshihara, K. Harrabi, A. O. Niskanen, Y. Nakamura, and J. S. Tsai, Decoherence of flux qubits due to $1/f$ flux noise, *Phys. Rev. Lett.* **97**, 167001 (2006).
- [174] K. Kakuyanagi, T. Meno, S. Saito, H. Nakano, K. Semba, H. Takayanagi, F. Deppe, and A. Shnirman, Dephasing of a superconducting flux qubit, *Phys. Rev. Lett.* **98**, 047004 (2007).
- [175] G. Ithier, E. Collin, P. Joyez, *et al.*, Decoherence in a superconducting quantum bit circuit, *Phys. Rev. B* **72**, 134519 (2005).
- [176] E. Paladino, Y. M. Galperin, G. Falci, and B. L. Altshuler, $1/f$ noise: Implications for solid-state quantum information, *Rev. Mod. Phys.* **86**, 361–418 (2014).
- [177] T. Struck, A. Hollmann, F. Schauer, *et al.*, Low-frequency spin qubit energy splitting noise in highly purified $^{28}\text{Si}/\text{SiGe}$, *npj Quantum Information* **6**, 40 (2020).
- [178] J. Yoneda, K. Takeda, T. Otsuka, *et al.*, A quantum-dot spin qubit with coherence limited by charge noise and fidelity higher than 99.9%, *Nature Nanotechnology* **13**, 102–106 (2017).
- [179] A. G. Fowler, Minimum weight perfect matching of fault-tolerant topological quantum error correction in average $\mathcal{O}(1)$ parallel time, *Quantum Information and Computation* **15**, 145–158 (2015).
- [180] O. Higgott and C. Gidney, Sparse Blossom: correcting a million errors per core second with minimum-weight matching, *Quantum* **9**, 1600 (2025).
- [181] A. deMarti iOlius, P. Fuentes, R. Orús, P. M. Crespo, and J. Etxezarreta Martinez, Decoding algorithms for surface codes, *Quantum* **8**, 1498 (2024).
- [182] S. Bravyi, M. Suchara, and A. Vargo, Efficient algorithms for maximum likelihood decoding in the surface code, *Phys. Rev. A* **90**, 032326 (2014).
- [183] Y. Tomita and K. M. Svore, Low-distance surface codes under realistic quantum noise, *Phys. Rev. A* **90**, 062320 (2014).
- [184] T. E. O’Brien, B. Tarasinski, and L. DiCarlo, Density-matrix simulation of small surface codes under current and projected experimental noise, *npj Quantum Information* **3**, 39 (2017).
- [185] M. Katsuda, K. Mitarai, and K. Fujii, Simulation and performance analysis of quantum error correction with a rotated surface code under a realistic noise model, *Phys. Rev. Res.* **6**, 013024 (2024).
- [186] A. S. Darmawan and D. Poulin, Tensor-network simulations of the surface code under realistic noise, *Phys. Rev. Lett.* **119**, 040502 (2017).
- [187] S. E. Nigg, A. Fuhrer, and D. Loss, Superconducting grid-bus surface code architecture for hole-spin qubits, *Phys. Rev. Lett.* **118**, 147701 (2017).
- [188] J. Helsen, M. Steudtner, M. Veldhorst, and S. Wehner, Quantum error correction in cross-bar architectures, *Quantum Science and Technology* **3**, 035005 (2018).

- [189] B. Buonacorsi, Z. Cai, E. B. Ramirez, K. S. Willick, S. M. Walker, J. Li, B. D. Shaw, X. Xu, S. C. Benjamin, and J. Baugh, Network architecture for a topological quantum computer in silicon, *Quantum Science and Technology* **4**, 025003 (2019).
- [190] Z. Cai, M. A. Fogarty, S. Schaal, S. Patomäki, S. C. Benjamin, and J. J. L. Morton, A silicon surface code architecture resilient against leakage errors, *Quantum* **3**, 212 (2019).
- [191] M. Rispler, P. Cerfontaine, V. Langrock, and B. M. Terhal, Towards a realistic GaAs-spin qubit device for a classical error-corrected quantum memory, *Phys. Rev. A* **102**, 022416 (2020).
- [192] Á. Rozgonyi and G. Széchenyi, Break-even point of the phase-flip error correcting code, *New Journal of Physics* **25**, 103004 (2023).
- [193] B. Hetényi and J. R. Wootton, Tailoring quantum error correction to spin qubits, *Phys. Rev. A* **109**, 032433 (2024).
- [194] K. Takeda, A. Noiri, T. Nakajima, L. C. Camenzind, T. Kobayashi, A. Sammak, G. Scappucci, and S. Tarucha, Rapid single-shot parity spin readout in a silicon double quantum dot with fidelity exceeding 99%, *npj Quantum Information* **10**, 22 (2024).
- [195] A. Fedorov, P. Macha, A. K. Feofanov, C. J. P. M. Harmans, and J. E. Mooij, Tuned transition from quantum to classical for macroscopic quantum states, *Phys. Rev. Lett.* **106**, 170404 (2011).
- [196] Y.-H. Lin, L. B. Nguyen, N. Grabon, J. San Miguel, N. Pankratova, and V. E. Manucharyan, Demonstration of protection of a superconducting qubit from energy decay, *Phys. Rev. Lett.* **120**, 150503 (2018).
- [197] N. Earnest, S. Chakram, Y. Lu, *et al.*, Realization of a Λ system with metastable states of a capacitively shunted fluxonium, *Phys. Rev. Lett.* **120**, 150504 (2018).
- [198] A. Gyenis, P. S. Mundada, A. Di Paolo, T. M. Hazard, X. You, D. I. Schuster, J. Koch, A. Blais, and A. A. Houck, Experimental realization of a protected superconducting circuit derived from the $0-\pi$ qubit, *PRX Quantum* **2**, 010339 (2021).
- [199] A. Gyenis, A. Di Paolo, J. Koch, A. Blais, A. A. Houck, and D. I. Schuster, Moving beyond the transmon: Noise-protected superconducting quantum circuits, *PRX Quantum* **2**, 030101 (2021).
- [200] E. Huang, A. C. Doherty, and S. Flammia, Performance of quantum error correction with coherent errors, *Phys. Rev. A* **99**, 022313 (2019).
- [201] J. Behrends and B. Béri, The surface code beyond Pauli channels: Logical noise coherence, information-theoretic measures, and errorfield-double phenomenology (2025), arXiv:2412.21055 .
- [202] J. Behrends and B. Béri, Statistical mechanical mapping and maximum-likelihood thresholds for the surface code under generic single-qubit coherent errors (2024), arXiv:2410.22436 .
- [203] A. Miller, C. Ostrove, J. Hines, R. Blume-Kohout, K. Young, and T. Proctor, Efficient simulation of Clifford circuits with small Markovian errors (2025), arXiv:2504.15128 .
- [204] D. M. Zajac, T. M. Hazard, X. Mi, E. Nielsen, and J. R. Petta, Scalable gate architecture for a one-dimensional array of semiconductor spin qubits, *Phys. Rev. Appl.* **6**, 054013 (2016).

- [205] J. M. Boter, J. P. Dehollain, J. P. G. van Dijk, T. Hensgens, R. Versluis, J. S. Clarke, M. Veldhorst, F. Sebastiano, and L. M. K. Vandersypen, A sparse spin qubit array with integrated control electronics, in *International Electron Devices Meeting (IEDM)* (IEEE, 2019).
- [206] J. M. Boter, J. P. Dehollain, J. P. van Dijk, *et al.*, Spiderweb array: A sparse spin-qubit array, *Phys. Rev. Appl.* **18**, 024053 (2022).
- [207] S. M. Patomäki, M. F. Gonzalez-Zalba, M. A. Fogarty, Z. Cai, S. C. Benjamin, and J. J. L. Morton, Pipeline quantum processor architecture for silicon spin qubits, *npj Quantum Information* **10**, 31 (2024).
- [208] M. Künne, A. Willmes, M. Oberländer, *et al.*, The SpinBus architecture for scaling spin qubits with electron shuttling, *Nature Communications* **15**, 4977 (2024).
- [209] R. Li, Ruoyu Li, L. Petit, D. P. Franke, *et al.*, A crossbar network for silicon quantum dot qubits, *Science Advances* **4**, eaar3960 (2018).
- [210] F. Borsoi, N. W. Hendrickx, V. John, M. Meyer, S. Motz, F. van Riggelen, A. Sammak, S. L. de Snoo, G. Scappucci, and M. Veldhorst, Shared control of a 16 semiconductor quantum dot crossbar array, *Nature Nanotechnology* **19**, 21–27 (2023).
- [211] N. Paraskevopoulos, F. Sebastiano, C. G. Almudever, and S. Feld, SpinQ: Compilation strategies for scalable spin-qubit architectures, *ACM Transactions on Quantum Computing* **5**, 1–36 (2023).
- [212] N. Paraskevopoulos, C. G. Almudever, and S. Feld, BeSnake: A routing algorithm for scalable spin-qubit architectures, *IEEE Transactions on Quantum Engineering* **5**, 1–22 (2024).
- [213] T. Fujita, T. A. Baart, C. Reichl, W. Wegscheider, and L. M. Vandersypen, Coherent shuttle of electron-spin states, *npj Quantum Information* **3**, 22 (2017).
- [214] A. R. Mills, D. M. Zajac, M. J. Gullans, F. J. Schupp, T. M. Hazard, and J. R. Petta, Shuttling a single charge across a one-dimensional array of silicon quantum dots, *Nature Communications* **10**, 1063 (2019).
- [215] F. Ginzl, A. R. Mills, J. R. Petta, and G. Burkard, Spin shuttling in a silicon double quantum dot, *Phys. Rev. B* **102**, 195418 (2020).
- [216] J. A. Krzywda and L. Cywiński, Adiabatic electron charge transfer between two quantum dots in presence of $1/f$ noise, *Phys. Rev. B* **101**, 035303 (2020).
- [217] J. A. Krzywda and L. Cywiński, Interplay of charge noise and coupling to phonons in adiabatic electron transfer between quantum dots, *Phys. Rev. B* **104**, 075439 (2021).
- [218] B. Jadot, P.-A. Mortemousque, E. Chanrion, V. Thiney, A. Ludwig, A. D. Wieck, M. Urdampilleta, C. Bäuerle, and T. Meunier, Distant spin entanglement via fast and coherent electron shuttling, *Nature Nanotechnology* **16**, 570–575 (2021).
- [219] J. Yoneda, W. Huang, M. Feng, *et al.*, Coherent spin qubit transport in silicon, *Nature Communications* **12**, 4114 (2021).
- [220] B. Buonacorsi, B. Shaw, and J. Baugh, Simulated coherent electron shuttling in silicon quantum dots, *Phys. Rev. B* **102**, 125406 (2020).

- [221] I. Seidler, T. Struck, R. Xue, N. Focke, S. Trellenkamp, H. Bluhm, and L. R. Schreiber, Conveyor-mode single-electron shuttling in Si/SiGe for a scalable quantum computing architecture, *npj Quantum Information* **8**, 100 (2022).
- [222] A. Zwerver, S. Amitonov, S. de Snoo, M. Mądzik, M. Rimbach-Russ, A. Sammak, G. Scappucci, and L. Vandersypen, Shuttling an electron spin through a silicon quantum dot array, *PRX Quantum* **4**, 030303 (2023).
- [223] F. van Riggelen-Doelman, C.-A. Wang, S. L. de Snoo, W. I. L. Lawrie, N. W. Hendrickx, M. Rimbach-Russ, A. Sammak, G. Scappucci, C. Déprez, and M. Veldhorst, Coherent spin qubit shuttling through germanium quantum dots, *Nature Communications* **15**, 5716 (2024).
- [224] R. Xue, M. Beer, I. Seidler, S. Humpohl, J.-S. Tu, S. Trellenkamp, T. Struck, H. Bluhm, and L. R. Schreiber, Si/SiGe QuBus for single electron information-processing devices with memory and micron-scale connectivity function, *Nature Communications* **15**, 2296 (2024).
- [225] A. J. Sigillito, M. J. Gullans, L. F. Edge, M. Borselli, and J. R. Petta, Coherent transfer of quantum information in a silicon double quantum dot using resonant SWAP gates, *npj Quantum Information* **5**, 110 (2019).
- [226] A. Noiri, K. Takeda, T. Nakajima, T. Kobayashi, A. Sammak, G. Scappucci, and S. Tarucha, A shuttling-based two-qubit logic gate for linking distant silicon quantum processors, *Nature Communications* **13**, 5740 (2022).
- [227] D. Pataki and A. Pályi, Auxiliary files for Compiling the surface code to crossbar spin qubit architectures, <https://doi.org/10.5281/zenodo.14259643> (2024).
- [228] A. Crippa, R. Ezzouch, A. Aprá, *et al.*, Gate-reflectometry dispersive readout and coherent control of a spin qubit in silicon, *Nature Communications* **10**, 2776 (2019).
- [229] E. J. Connors, J. Nelson, and J. M. Nichol, Rapid high-fidelity spin-state readout in Si/Si-Ge quantum dots via rf reflectometry, *Phys. Rev. Appl.* **13**, 024019 (2020).
- [230] A. O. Denisov, G. Fuchs, S. W. Oh, and J. R. Petta, Dispersive readout of a silicon quantum device using an atomic force microscope-based rf gate sensor, *Applied Physics Letters* **123**, 093502 (2023).
- [231] T. Futaya, R. Mizokuchi, M. Taguchi, T. Miki, M. Nagata, J. Yoneda, and T. Kodera, Cryogenic flip-chip interconnection for silicon qubit devices, *Japanese Journal of Applied Physics* **63**, 03SP64 (2024).
- [232] D. Rosenberg, D. Kim, R. Das, *et al.*, 3D integrated superconducting qubits, *npj Quantum Information* **3**, 42 (2017).
- [233] C. R. Conner, A. Bienfait, H.-S. Chang, *et al.*, Superconducting qubits in a flip-chip architecture, *Applied Physics Letters* **118**, 232602 (2021).
- [234] A. M. Tyryshkin *et al.*, Electron spin coherence exceeding seconds in high-purity silicon, *Nature Materials* **11**, 143–147 (2011).
- [235] D. Pataki and A. Pályi, Verification of shuttling protocols in crossbar spin qubit architectures, <https://doi.org/10.5281/zenodo.14047331> (2024).
- [236] A. Sen, G. Frank, B. Kolok, J. Danon, and A. Pályi, Classification and magic magnetic field directions for spin-orbit-coupled double quantum dots, *Phys. Rev. B* **108**, 245406 (2023).

-
- [237] L. H. Pedersen, N. M. Møller, and K. Mølmer, Fidelity of quantum operations, *Physics Letters A* **367**, 47–51 (2007).
- [238] D. Pataki, A. Márton, J. K. Asbóth, and A. Pályi, Coherent errors in stabilizer codes caused by quasistatic phase damping, *Phys. Rev. A* **110**, 012417 (2024).
- [239] D. K. Tuckett, S. D. Bartlett, and S. T. Flammia, Ultrahigh error threshold for surface codes with biased noise, *Phys. Rev. Lett.* **120**, 050505 (2018).
- [240] J. P. Bonilla Ataides, D. K. Tuckett, S. D. Bartlett, S. T. Flammia, and B. J. Brown, The XZZX surface code, *Nature Communications* **12**, 2172 (2021).
- [241] A. Dua, A. Kubica, L. Jiang, S. T. Flammia, and M. J. Gullans, Clifford-deformed surface codes, *PRX Quantum* **5**, 010347 (2024).